Master's Degree in Aerospace Engineering

Master's Degree Thesis

Transonic Low Reynolds number Airfoil Optimization using Discrete Adjoint Method

Supervisors:
Prof. Domenic D'Ambrosio

Ph.D. Manuel Carreno Ruiz

Candidate:
Manuel Nebbiai

2022/2023

Abstract

The increasing interest on flying on different planets from earth, whose atmospheres have mainly low density, has brought the need of analysing the low Reynolds aerodynamics characteristics of airfoils.

Moreover, atmospheres as that of Mars, where the decrease of density is not accompanied by an equal decrease on gravity acceleration, makes difficult flying in subsonic regimes for aircraft as drones.

Therefore, this paper targets the optimization of low-Reynolds based airfoil in transonic flows.

The method of optimization chosen is the adjoint multipoint optimization, first used in steady state simulations, then in time-dependent simulations.

In the end, the new airfoils are analysed at three different Reynolds and Mach conditions and their polars are compared with that of the initial airfoil.

Contents

List of Figures

List of Tables

List of Symbols

α	Angle of attack
$\bar{\tau}$	Shear stress matrix
μ	Dynamic viscosity
ρ	Density
$\mathbf{v}$	Velocity vector
a	Speed of sound
c	Chord length
C_d	Drag Coefficient
C_l/C_d	Lift to drag ratio
C_l	Lift Coefficient
E	Total energy for unit of volume
k	Thermal conductivity
$M = \frac{U}{a}$	Mach Number
p	Pressure
Re	Reynolds Number
S	Surface
T	Temperature
t	Time
U_∞	Upstream velocity
V	Volume

1 Low Reynolds Flow around an Airfoil: critical aspects

The Reynolds number is a non-dimensional factor that indicates the ratio between inertial and viscous forces. The expression is :

$$Re = \frac{\rho U_\infty c}{\mu}$$

Velocity, density and viscosity of the flow, together with the characteristic dimension of the phenomenon, i.e. airfoil chord, influence the Reynolds number. Thus, an aircraft that has to fly in low-density atmosphere, that has low velocity or that has very small chord length, will encounter low Reynolds flows.

The Martian atmosphere, mostly composed of carbon dioxide, has a density 1.388% of that of Earth, with an acceleration of gravity 40% of that of Earth [24]. For an aircraft to fly, it has to produce a lifting force at least equal to his weight. Because aerodynamics forces are directly related to the density and the velocity squared, without changing its lift coefficient, an aircraft on Mars has to fly at a velocity 5 times greater. Thus, it encounters compressibility problems.

In this paper, it has been considered flow conditions between these following ranges:

- $Re = 8000 \div 14000$;
- $Ma = 0.5 \div 0.7$.

where the lower part of the range may be encountered near the blade root of the rotor, and the higher part near the tip of the blade of a drone.

The principal effects of low Reynolds number are a degradation of performance in terms of both lift to drag ratio and unsteady oscillations of forces([4].

The first effect is mostly caused by the increase in viscous drag. In general, total drag is the sum of pressure drag and viscous drag. The former is caused by the displacement of the boundary layer and wake that modify the pressure distribution. The latter is due to the action of friction forces against the surface [1]. While at high Reynolds number the former is an order of magnitude higher than the latter, at low Reynolds number their contributions to total drag are comparable.

The second effect is due to the flow separation that occurs on the airfoil. Therefore, understanding separation effects is paramount for the design of low Reynolds airfoil.

One phenomenon related to separation is the formation of a laminar separation bubble and its transition to turbulence. These will be discussed in section 1.1.

As already discussed, along with that of low Reynolds numbers, there will be an influence of the Mach number on the airfoil characteristics.

In the lower range of Mach considered, the expansion on a typical airfoil is not strong enough to form a supersonic region, so the compressibility only influences the amplitude and frequency of the oscillations previously cited.

At Mach equal to 0.7, a supersonic region occurs on the upper body of the airfoil, and it is possible that a shock wave forms. Shock waves are sources of total pressure drops, thus they increase the total drag.

A further rise in Mach number increases the strength of the expansion on the airfoil, extending the supersonic region. A stronger shock will compare close to the trailing edge of the airfoil. In this region the boundary layer height is large, thus the foot of the shock is far from the actual airfoil, therefore the pressure distribution is not influenced.

In addition, the distance between the shock and the airfoil mitigates the possibility of a shock induced boundary layer separation [19].

The influence of Mach number on airfoil performance will be discussed in section 1.2.

1.1 Laminar Separation Bubble

The process of formation of laminar separation bubble undergoes three phases: first the laminar boundary layer, affected by the adverse pressure gradient on the suction peak of the airfoil, separates forming a separated shear layer; thereafter the shear layer is subjected to transition to turbulence; lastly the flow reattaches, forming a bubble of separated flow.

The bubble can be divided in two regions along the chord: the first is the "dead air" region in which the flow is still or moving backwards slowly and the pressure gradient is zero, in the second one a vortex is formed, with a stronger circulation velocity([22], [13]).

These two regions can also be distinguished in plots of pressure coefficient along the chord of airfoils with laminar separation bubbles.

Figure 1 shows the pressure coefficient at an angle of attack of 6 degrees over the airfoil that will be optimised later, that is an airfoil optimized using *XFOIL* [2] at a condition of Re = 10000 and M = 0.5, for a lift coefficient of 0.87, by M. Ruiz in "Numerical Simulation and Aerodynamic Design of Small-Scale Rotary-Wing for Unmanned Aerial Systems in Terrestrial and Martian Applications".

The pressure plateau, characteristic of the "dead air" region, can be noted together with the abrupt pressure rise due to the reattachment of the flow.

The length of the laminar separation bubble depends on the position of both the separation and the reattachment point. These points are influenced by the Reynolds number and the angle of attack.

As showed in [22], an increase in Reynolds number tends to move the separation point forward along the chord and the reattachment point backward, resulting in a shorter bubble.

Similar trends arise from an increase in angle of attack with exception at near stall angle of attack, where the bubble undergoes a phenomenon called "burst", that is a sudden rise of the length of the bubble that cause a decline of the lift coefficient [13].

Transition to turbulence of the separated shear layer is analysed with the linear stability theory in [7], [22] et al., in which it is stated that inviscid disturbance and secondary instabilities are the principal causes of the transition and the subsequent reattachment of the flow.

An inviscid disturbance rises in the adverse pressure gradient region and is advected by the flow. Its strength is maximum where the velocity is inflected, that is in the separated shear layer.

At the peak height of the bubble, the Kelvin-Helmholtz instability causes the shear layer to roll down towards the airfoil and causes a reattachment.

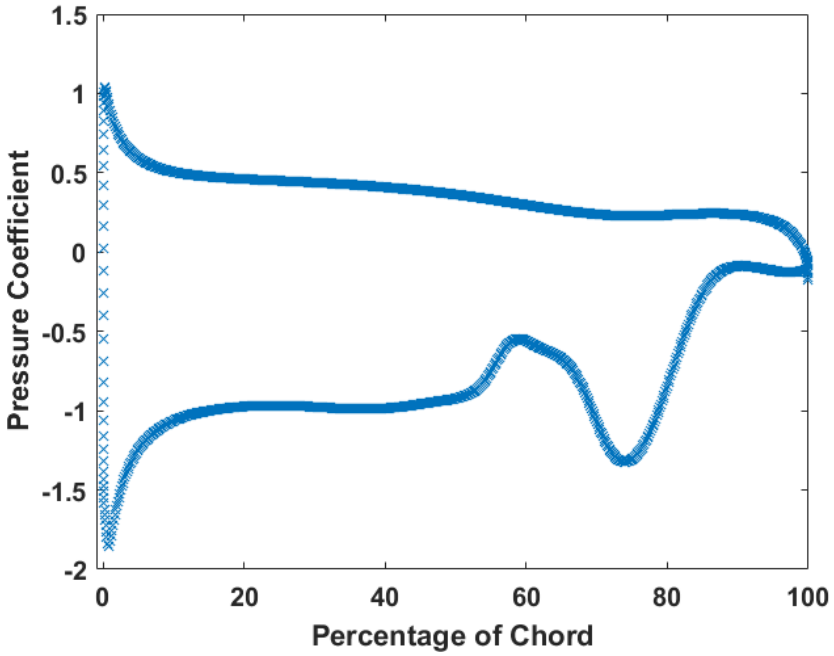

Figure 1: Pressure coefficient along the chord of the initial airfoil

The flow over the laminar separation bubble is also influenced by amplified disturbance that increase the vorticity of the flow. Therefore, the shear layer breaks down into vortices that are the principal cause of fluctuating load over the airfoil [22].

In figure 2 is shown the evolution of the laminar separation bubble over the initial airfoil at 6 degrees of angle of attack at Reynolds number 8000. The scalar field is the horizontal negative velocity, thus a white field means that the horizontal velocity is greater than zero.

In this case, flow is separated near the leading edge and reattaches after the mid-chord, forming a long separated region.

A separated bubble is also present above the trailing edge, and it can be seen that it formed from the previous region.

It can be noted the formation of a reattached flow inside the separated shear layer that tends to move the latter away from the airfoil.

When this region is high enough to link with the downstream moving flow above the shear layer, two bubbles are formed, splitting the separated region.

In figure 3 is also shown the evolution of the vorticity field.

From these images, it can be understood that the splitting of the separated region in two laminar separated bubbles is tied up with the vortex shedding of the leading edge. In fact, the vortex is shed at the same time that the separated region is split.

The roll up of vortices near the mid-chord of the airfoil is a trend that can be seen also in the vorticity fields computed by Désert in [19] at Reynolds numbers 10000.

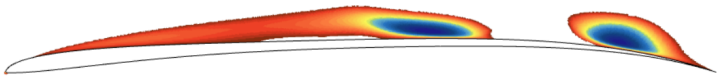

(a) Formation of a reattached flow region

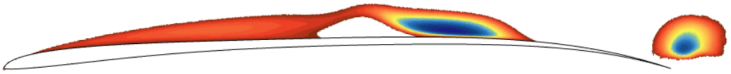

(b) Enlargement of the reattached flow region

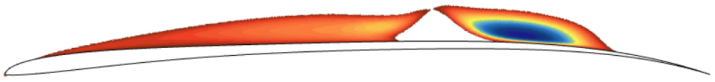

(c) Splitting of the separated flow

Figure 2: Evolution of the separated flow over the initial airfoil at 6 degrees angle of attack at Reynolds number 8000

(a) Formation of a leading edge vortex

(b) Growth of the leading edge vortex

(c) Shedding of the leading edge vortex

Figure 3: Evolution of the vorticity field over the initial airfoil at 6 degrees angle of attack at Reynolds number 8000

In figure 4 are reported lift and drag coefficient of the airfoil between three shedding of vortices.

The maximum of both C_l and C_d corresponds to the initial situation where there is a separated flow over the trailing edge that decrease the pressure in this region, resulting in a stronger bottom load. That can be seen in the drop of the pressure coefficient near the trailing edge in figure 1.

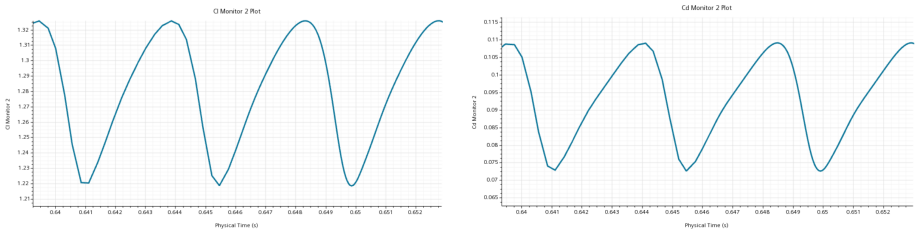

(a) Lift coefficient (b) Drag Coefficient

Figure 4: Forces coefficients of initial airfoil at 6 degrees angle of attack at Reynolds number 8000

Another aspect of the airfoil characteristics influenced by the formation of the laminar separation bubble is the slope of the $C_l - \alpha$ curve:

for inviscid potential flow, the slope of the curve has an ideal value of 2π, constant with the angle of attack. Airfoil thickness influence this value, increasing it;

for real flow, at high Reynolds number, the slope, that remains constant for most angle of attack, is influenced only at high angle of attack, where the separation of the flow cause a drop on the slope (airfoil stall);

for real flow, at low Reynolds number, the stall happens at lower angle of attack but, more important for applications related to this paper, the slope is not linear([22], [18]).

Non-linearity of lift coefficient with angle of attack causes problem in the prediction of performance and in flight control.

Figure 5 show lift coefficient in function of angle of attack for Reynolds of 8000 and 10000 of initial. At angle of attack larger than 5 degrees, the slope increases. This happens precisely when the laminar separation bubble is formed. In fact, the plateau in pressure caused by the bubble on the upper surface increments the difference in pressure with the lower surface, resulting in a boost in lift coefficient ([18], [24]).

At angle of attack over 7 degrees, the slope decreases up to becoming negative, first because of the previously described "burst" of the laminar separation bubble, then, when the reattachment point is no longer present, it is the separation over the entire length of the airfoil upper surface that deteriorates the performances [16].

For other geometry, the angle of attack at which the bubble forms could change, resulting in a completely different lift-angle of attack curve. What doesn't change, though, is the curve non-linearity.

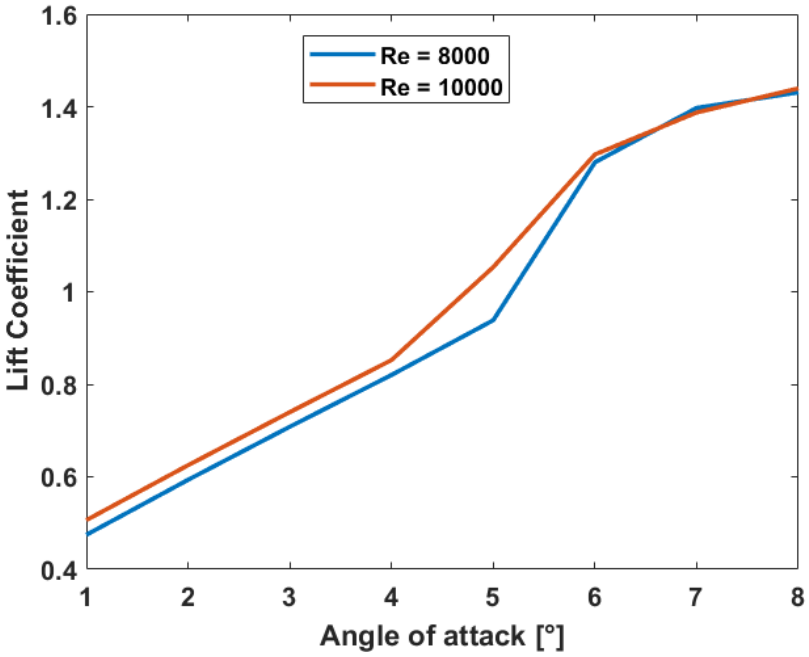

Figure 5: Lift coefficient at various angle of attack for Re = 8000 and Re = 10000

1.2 Influence of Mach Number

The second aspect that has to be discussed is the influence of Mach number on performances.

As described in [24], when Mach number is increased, the separation point moves upstream because of a more severe adverse pressure gradient near the leading edge.

Conversely, the reattachment point, moves downstream, increasing the possibility of a completely separated flow over the upper surface of the airfoil. This is a result of a stabilizing effect on the Kelvin-Helmholtz instabilities caused by the increased compressibility. The separated shear layer is less susceptible to transition due to its diminished instability, thus the transition and reattachment point moves downstream.

These two effects combined results in a longer laminar separation bubble or in a completely separated shear layer over the upper surface of the airfoil.

Another result of earlier separations is a wider vortex street that is accompanied by stronger oscillations of forces [19].

In the ranges of Mach numbers established beforehand, very weak shock waves form on the surface of the airfoil chosen. The supersonic region ends with a shock wave that generates total pressure losses of less than 1%. This could also be seen by visualizing the total pressure drop field (figure 6). Total pressure drops are only generated by vorticity in the boundary layer, and a small pressure loss occurs in correspondence to the supersonic region. The pressure loss is spread in a region wider than a normal shock wave, due to the effects of

the high viscosity. The flow then advects the loss of pressure downstream.

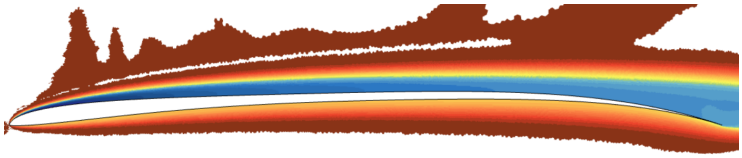

(a) Total pressure drop field

(b) Supersonic region with a maximum local Mach number of 1.172.

Figure 6: Simulation of the initial airfoil at Re = 8000 and Mach = 0.5. Warmer colour indicates greater values

A further increase in Mach number results in the formation of stronger shock waves over the upper surface of the airfoil. Yamaguchi [24] distinguishes two possible shock formation: a lambda-type shock wave and a trailing edge shock wave (He includes also a bow shock formation for supersonic flows).

Lambda-type shock waves are formed by the interaction between compression waves and separated shear layer ([5], [14]). In general, their formation happens far from the trailing edge and at lower Mach number than trailing edge shock waves. In fact, an increase in Mach number produces a downstream movement of the formation point of shock waves [3].

When shock waves are formed at the trailing edge, the boundary layer below them is at his maximum height. Shock waves feet are far away from the airfoil surface, resulting in a nearly absent influences on the pressure distribution by the shock wave/boundary layer interaction [19].

Performance of the airfoil are affected by all of these effects. In general, with an increase in Mach number, there will be a subsequent increase in both lift and drag coefficient, moving the angle of attack of maximum lift to drag ratio towards lower angles [19].

In addition, forces oscillations are of greater strength and with higher frequency. These effects are shown in figure 7 and 8: lift coefficient variations in time are plotted together with their power spectral density (data are taken from simulation of the initial airfoil at Re = 8000). The latter is obtained via Time Fourier Transform.

The magnitude of the oscillations, calculated dividing the difference between the upper and the lower value of the harmonic by the mean value, increase from 0.185% to 0.37%.

The frequency of the oscillations caused by the vortex shedding increase from a 599.8 Hz to 680 Hz.

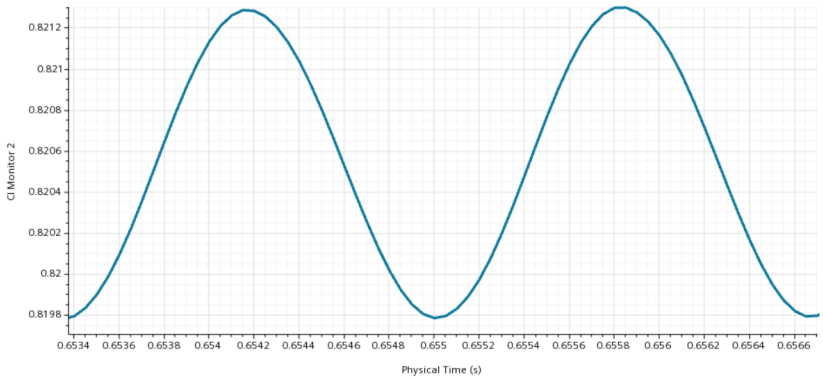

(a) Lift coefficient at Mach 0.5

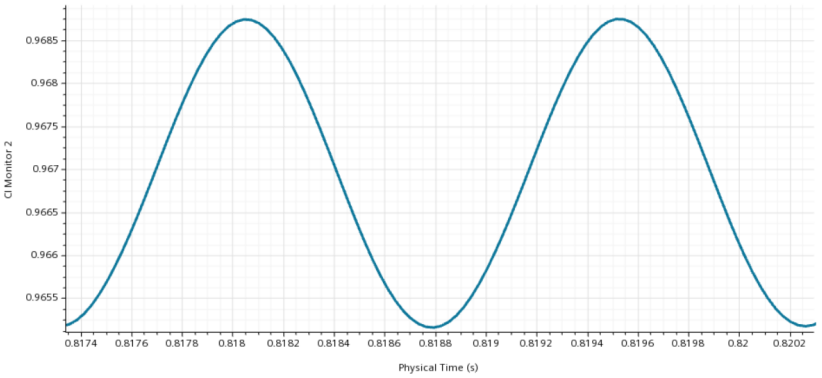

(b) Lift coefficient at Mach 0.7

Figure 7: Comparison of vortex shedding oscillation intensity of the initial airfoil at Re = 8000 at different Mach values

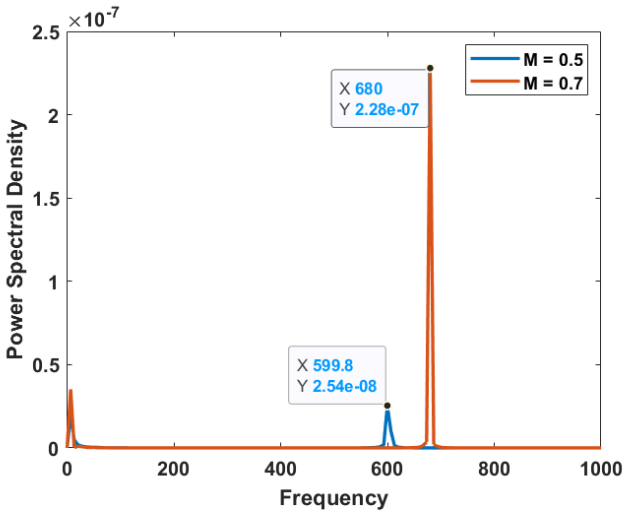

Figure 8: Power Spectral Density of lift coefficient of the initial airfoil at RE = 8000 at different Mach values

1.3 Important Aspects for Optimization

All the aspects previously described influence the performance of the airfoil. The goal of the optimization is to find a geometry that has a greater lift to drag ratio of the initial airfoil with a range of usability large enough, that is, that has almost constant performance for a range of neighbours angles of attack.

It needs to be taken into account the limited variation of viscous drag with angle of attack. In figure 9 viscous and pressure drag over the initial airfoil are plotted for Reynolds number 8000 and 10000.

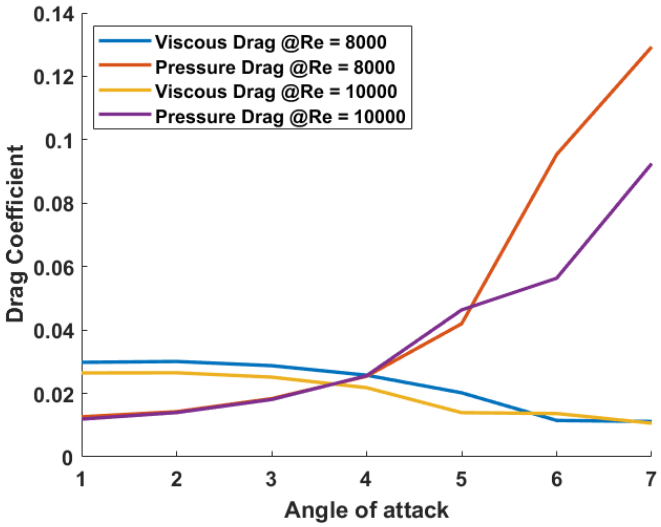

Figure 9: Comparison of viscous and pressure drag of the initial airfoil at Reynolds number 8000 and 10000

The former form of drag decrease when angle of attack is increased. This happens due to separation, that causes the wall shear stress to become negative. A negative wall shear stress result in a negative component of viscous drag, that is, a thrust component.

The pressure drag increases with angle of attack due to formation of laminar separation bubble. At around 7 degrees, the bubble "bursts" and then the flow is separated from the leading edge, causing a drastic increment of pressure drag.

Because of the high viscous drag at low angles of attack, the airfoil will not have high performances at these angles, at which lift coefficient is not high enough to produce an appreciable lift to drag ratio.

Therefore, the problems described in the previous sections are coupled with the need of increasing the angle of attack to increase the lift coefficient.

For these reasons, the optimization has the goal of finding a geometry that solves or limits these problems, obtaining a higher lift to drag ratio.

Simulations setup and optimization method will be described in the next section, while the initial airfoil performance will be shown in section 4.

2 CFD Analysis Setup

2.1 Discretization of Governing Equations

A CFD analysis solves numerically the Navier-Stokes Equations to obtain flow fields around a certain geometry.

In this paper, all the simulations use a laminar flow approximation of the bidimensional N-S equations: viscous shear stress contains only the molecular viscosity, that is equivalent to consider a RANS simulation with Reynolds stresses equal to zero everywhere on the domain.

In the following, the Navier-Stokes equations in bidimensional conservative integral form are presented. Because Reynolds stresses are not considered, these equations represent also the Reynolds averaged Navier-Stokes equations with no need for closure models.

$$\frac{\partial}{\partial t}\int_V \rho dV + \int_S \rho \mathbf{v} dS = 0$$

$$\frac{\partial}{\partial t}\int_V \rho \mathbf{v} dV + \int_S \rho \mathbf{v}(\mathbf{v}\cdot\mathbf{n})dS + \int_S p\mathbf{n}dS - \int_S (\bar{\tau}\cdot\mathbf{n})dS = 0$$

$$\frac{\partial}{\partial t}\int_V E dV + \int_S (E+p)\mathbf{v}\cdot\mathbf{n}dV + \int_S k(\nabla T\cdot\mathbf{n})dS - \int_S (\bar{\tau}\cdot\mathbf{v})\cdot\mathbf{n}dS = 0 \quad (1)$$

These equations are then discretised with finite volume method.

In the finite volume method the domain is divided in cells and in each cell the laws of conservation of equation 1 are applied.

Volumes integrals in the cell are approximated by the mean value of the cell multiplied by the cell volume. The mean value of a variable in the cell is represented, with second order accuracy, by the value of the variable at the cell centre.

Surfaces integrals, in two dimension, are represented by the sum of the integrals over the interface between the cell and its neighbours. These integrals are approximated by the mean value on the interfaces multiplied by the length of the interface.

In general, this surfaces integrals are divided in convective and diffusive fluxes, where the former ones are fluxes that derive from the advection by the flow of the variable considered, while the latter ones are fluxes that derive from the molecular diffusion and dissipation.

The discretised equations, in which $\mathbf{U}$ represents the conservative variables at the centre of the cell, $\mathbf{F}_c$ and $\mathbf{F}_d$ represent respectively convective and diffusive fluxes, are:

$$\frac{\partial \mathbf{U}}{\partial t}\Delta V + \mathbf{F}_c + \mathbf{F}_d = 0 \quad (2)$$

Once equations are discretised, there is the need of choosing methods of computing the fluxes.

While centred scheme can be adopted to compute diffusive fluxes, they cannot be used for convective fluxes because of stability problems. For this reason, fluxes are distinct in the first place.

Simulations conducted in this paper use a preconditioned Roe's flux-difference splitting scheme [8] for evaluating convective fluxes. Diffusive fluxes, that are

proportional to velocity gradients, need values of these gradients at the interfaces medium point. Cell centre gradients are used to compute these values using weighted averages and non-orthogonal direction correction terms.

Cell centre gradients are evaluated by a hybrid Green-Gauss/Least-Squared method [20].

All these methods use values at interfaces medium points. These values are evaluated by reconstructing the solution from the cell centre value.

According to the order of accuracy required, the reconstruction is of a lower order. Thus, a first order accuracy scheme uses a constant reconstruction, while a second order accuracy scheme uses a linear reconstruction.

A second order accuracy scheme is used, thus a linear reconstruction. Cell centre gradients are used to linear interpolate values in the cells. With this method of interpolation, values in the medium point of an interface could fall outside ranges of minimum and maximum values of neighbours cells [20].

For this reason, gradients are limited by gradient limiters. Venkatakrishnan gradient limiter is adopted [6].

Then an integration method has to be chosen. A second-order implicit scheme using backward differentiation is employed: the solution at the next time-step is calculated using the solution itself and those of the previous two time-step (the first calculation is only of first order because the solver has only the initial condition) [20].

Finally, the set of partial derivatives equations is discretised, every time-step, in a set of algebraic equations of dimension proportional to the number of cells in which the domain is divided.

Such non-linear systems are solved using iterative algorithms. The algebraic multi-grid method (AMG) is used to solve the system. This method exploits the faster convergence of a high frequency residual than that of a low frequency one ([15], [9]).

When a set is solved iteratively, the solution ϕ that solves

$$A\phi = b$$

is not immediately reached, but at a certain iteration k, a solution ϕ_k that doesn't solve the equation above is computed, thus

$$A\phi_k - b = R_k \neq 0$$

where R_k is the residual at iteration k. There are cells where residuals are lower than in other cells, creating an oscillating field of residuals with low and high frequencies. In the first step of an iterative method, high frequency oscillations are dumped, leaving a spatial distribution of residuals with only low frequency oscillations. These are the oscillations that take the most time to be reduced.

AMG methods transfer the residual field computed in the firsts' iteration of the iterative solver, from the initial fine mesh into a coarser mesh constructed by agglomerating cells of the initial mesh. When this happens, low frequencies are transformed in high frequencies. Then the iterative solver is applied to the coarser mesh and a newly residual field is computed and subsequently interpolated on the initial mesh.

There could be multiple level of coarsening and different method of iteration. In the simulations of this paper, a V-Cycle AMG algorithm is utilised [20].

To summarize, the setup chosen is:

- time-dependent Simulations;
- compressible, laminar flow;
- second order finite volume discretization;
- FDS Roe's method for convective fluxes;
- hybrid Green-Gauss/Least-Squared method for diffusive fluxes
- second order implicit scheme;
- algebraic multi-grid method.

Now it will be discussed the parameters chosen for the simulations and the mesh refinement adopted

2.2 Parameters and Mesh Settings

Once the setup is chosen, values of the time-step, the total time of simulation and a suitable mesh need to be chosen.

The time-step is influenced by the highest frequency of the phenomenon, that, for low Reynolds number airfoil, is the vortex shedding. A suitable time-step is at least half of the period of oscillation (Nyquist criterion). The value chosen is a tenth of the period of oscillation.

The total simulation time must be set so that the transient of the simulation has passed, and the simulation is in the asymptotic regions, i.e. the oscillations have established themselves and their maximum and minimum values remain constant. If the oscillations include higher order harmonics, a sufficient number of periods of the lowest frequency oscillation must pass.

The mesh generation is divided in two separated steps: first, a base mesh, that doesn't employ refinements, is generated; then a loop of refinement and simulation run is implemented.

Specifically, the loop involves a mesh refinement function based on some field functions that must be computed first. A number of implicit steps are therefore required to obtain the refinement function. It is then used to modify the base mesh and refine it in the desired areas. Finally, further implicit steps are performed, and the scheme is repeated for a certain number of iterations.

Mesh refinement function is based on velocity and pressure gradients. It involves 5 level of refinement: an initial value of cell size is chosen, and cell sizes of next levels are computed by doubling the value of precedent levels.

Levels are defined by the intensity of gradients (defined by the logarithm of the gradient magnitude): maximum levels intensities are chosen, and areas where gradients are more intense than this value are refined with the cell size of those levels. Thus, the first level has the greatest intensity value and will refine areas in which gradients are greater than this value, next levels will refine areas in which gradients are lower than the intensity of the previous level and greater than the intensity of its level.

Because the simulation is time-dependent, pressure and velocity gradients fields change with time. Therefore, the refinement function uses mean velocity and mean pressure gradients computed in a time window that contains numerous periods of oscillations.

All the parameters described assume that the frequency of the oscillations is known, but this is not known before starting the simulation. Therefore, a first simulation was done to better understand how the transient will evolve, what is the maximum time step that can be chosen, how the number of cells changes with the base size, and what is the best intensity value to choose.

Through this initial simulation, the parameters are setted in this way:

- base size: 0.6 meter;
- initial value: 0.3% of base size;
- time-step: 3e-5 seconds;
- total time: 0.8 seconds.

Gradients intensity will vary between simulations: simulations at lower angle of attack have weaker velocity and pressure gradients, while simulations at higher angle of attack have stronger gradients.

For this reason, the first value is set equal to the maximum value on the entire domain, at the angle of attack of the simulation, minus 5, that is the value chosen is 5 order of magnitude lower than the maximum.

Because at high angles of attack the number of cells become too large, the simulations at angles of attack greater than 4 use a value 4 order of magnitude lower than the maximum.

The number of iterations of the loop of refinements is 4, and the number of time-steps of implicit integration between two refinement is 750, so that the final mesh has a refinement based on field functions computed at 0.1 seconds.

Now, it will be discussed the automation process for simulating an airfoil polar.

2.3 Java Macro for Airfoil Polar

The automation process is done by using Java written macros. These are code that are generated by recording all the action done in Star CCM+ workspace. Then they can be modified.

Once the code is prepared, it can be called and all actions recorded will be done.

In the present simulations, PoliTo Cluster has been used for speeding the simulations up. Thus, Java Macros were launched in batch mode on a node of the Cluster.

Macro used for polar is composed of 10 steps, as in figure 10.

The first step is importing the airfoil coordinates and creating the surrounding domain. The latter has the form of a projectile and, to avoid disturbance from reflecting boundary conditions, domain boundaries are 300 chord-lengths far from the airfoil.

Once the three-dimensional domain is created and transformed in parts, the base mesh is generated. Because it is treated as bidimensional, the domain is given a badge for 2D meshing.

The base mesh is shown in figure 11 and 12.

Then the physics models are set as discussed above, and boundary and initial conditions are chosen to represent the Reynolds and Mach number wanted.

The angle of attack is changed by a rotation of coordinates of the flow, so that the airfoil remains with its chord horizontal, while the boundary conditions and initial conditions are rotated.

Stopping criteria are setted: one for the inner loop, representing the maximum number of iteration of AMG solver at every time-step; another one for the outer loop, representing the number of time-step or the maximum simulation time.

The first criterion is activated if, prior to 10 iteration, a drag coefficient convergence is reached. That is, if the relative difference from drag coefficient between two adjacent steps is less than 0.001 %, inner iterations are stopped, otherwise the inner loop is stopped after ten iteration.

The initial angle of attack is setted rotating the coordinate system.

Then the refinement loop is started: 750 steps of implicit scheme are done, refinement function is updates and used for re-meshing the base mesh, then other 750 steps are done and refinement continue until 0.1 seconds of simulation are reached.

Finally, with the refined mesh (figure 13 and 14 show a refined mesh for the initial airfoil) the simulation runs until the outer stopping criteria is reached, that is at 0.8 seconds.

The simulation is saved, and the loop is closed, setting a new angle of attack.

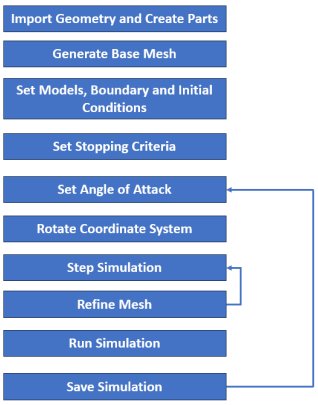

Figure 10: Algorithm scheme for Polar Java Macro

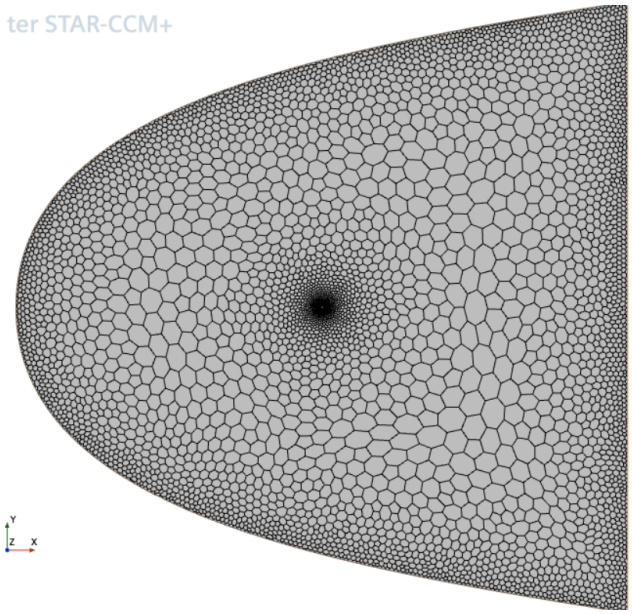

Figure 11: Base Mesh

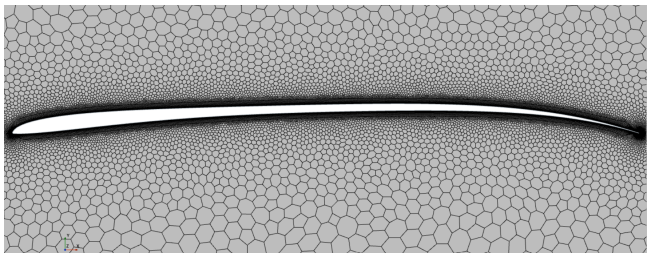

Figure 12: Detail of base mesh

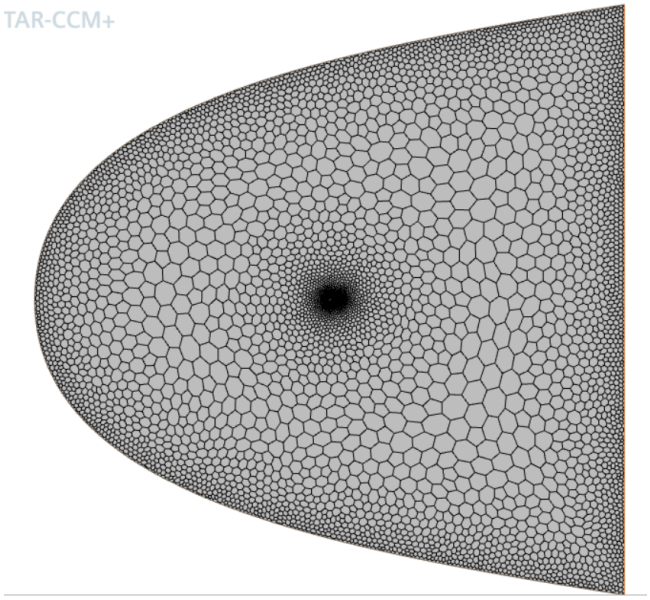

Figure 13: Final refined mesh for the initial airfoil at Re = 8000, M = 0.5, $\alpha = 4^{\circ}$

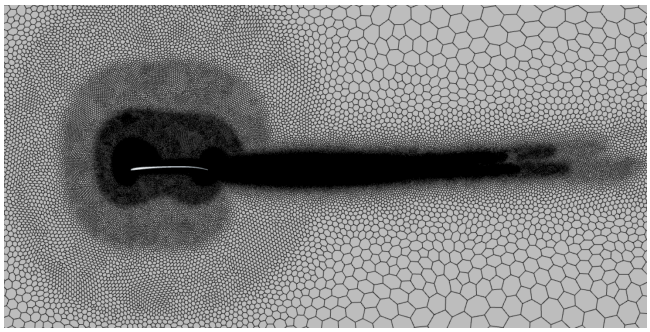

(a) Detail of levels of refinement

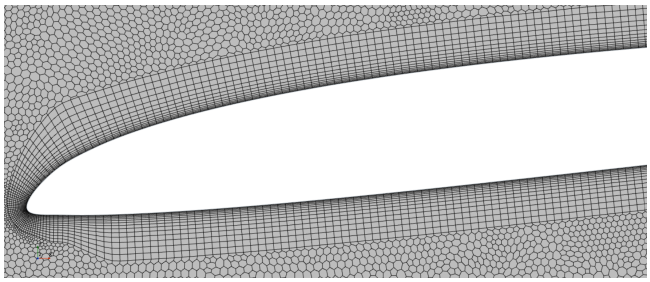

(b) Detail of prism layer-core transition near the leading edge

Figure 14: Details of the final refined mesh

3 Discrete Adjoint Method

As previously stated, the method of optimization chosen is the discrete adjoint method. It is based on gradient methods, but, while the latter ones have a direct dependence on the number of design variables, the adjoint method is weakly dependent on the number of design variables [10]. Thus, the computational cost is reduced for design problems with large number of design point, as aerodynamics shape optimization.

This method, being based on gradient method, evaluates the gradient of some function and uses it for the steepest descent iterative algorithm [12].

3.1 Equations Derivation

Like gradient based methods, the adjoint method aims to calculate the derivatives of cost functions with respect to a number of design variables, that, in the case of a shape optimization, represents a set of points on the airfoil or near the airfoil.

Cost functions are the quantities related to the optimization, i.e. lift or drag coefficients, lift to drag ratio among others.

Derivatives of these functions are used to search the minimum or the maximum w.r.t. airfoil shape. Thus, if the vector of cost function is denoted as $\mathbf{I}$, flow variables are $\mathbf{Q}$, mesh points are $\mathbf{X}$ and design variables $\mathbf{D}$, the optimization process is based on the calculation of

$$\frac{d\mathbf{I}}{d\mathbf{D}} = \frac{d}{d\mathbf{D}}\{\mathbf{I}[\mathbf{Q}(\mathbf{X}), \mathbf{X}]\}$$

Chain rule of derivations is then used to derive a usable equation

$$\frac{d\mathbf{I}}{d\mathbf{D}} = \left(\frac{\partial \mathbf{I}}{\partial \mathbf{X}} + \frac{\partial \mathbf{I}}{\partial \mathbf{Q}}\frac{\partial \mathbf{Q}}{\partial \mathbf{X}}\right)\frac{\partial \mathbf{X}}{\partial \mathbf{D}} \tag{3}$$

Now, if the dimension of the variables are:

- n: number of mesh points;
- m: number of design points;
- l: number of cost functions;

then:

$\frac{\partial \mathbf{X}}{\partial \mathbf{D}}$ has dimension $n \times m$, and represents the sensitivity of the mesh w.r.t the design variables

$\frac{\partial \mathbf{I}}{\partial \mathbf{X}} + \frac{\partial \mathbf{I}}{\partial \mathbf{Q}}\frac{\partial \mathbf{Q}}{\partial \mathbf{X}}$ has dimension $l \times n$, and represents the sensitivity of cost functions w.r.t the mesh;

$\frac{d\mathbf{I}}{d\mathbf{D}}$ has dimension $l \times m$ and is the sensitivity of cost functions w.r.t the design variables.

For large dimension, this matrix multiplication becomes expensive in terms of memory. To better understand equations 3, an example of calculation is presented: n, m, l are setted equal to 3, then the equation is written in matrix form:

$$\begin{bmatrix} \frac{dI_1}{dD_1} & \frac{dI_1}{dD_2} & \frac{dI_1}{dD_3} \\ \frac{dI_2}{dD_1} & \frac{dI_2}{dD_2} & \frac{dI_2}{dD_3} \\ \frac{dI_3}{dD_1} & \frac{dI_3}{dD_2} & \frac{dI_3}{dD_3} \end{bmatrix} = \begin{bmatrix} \frac{dI_1}{dX_1} & \frac{dI_1}{dX_2} & \frac{dI_1}{dX_3} \\ \frac{dI_2}{dX_1} & \frac{dI_2}{dX_2} & \frac{dI_2}{dX_3} \\ \frac{dI_3}{dX_1} & \frac{dI_3}{dX_2} & \frac{dI_3}{dX_3} \end{bmatrix} \begin{bmatrix} \frac{dX_1}{dD_1} & \frac{dX_1}{dD_2} & \frac{dX_1}{dD_3} \\ \frac{dX_2}{dD_1} & \frac{dX_2}{dD_2} & \frac{dX_2}{dD_3} \\ \frac{dX_3}{dD_1} & \frac{dX_3}{dD_2} & \frac{dX_3}{dD_3} \end{bmatrix}$$

then, using indexing notation and splitting each rows of the first matrix:

$$\frac{d\mathbf{I}}{dD_j} = \left(\frac{\partial \mathbf{I}}{\partial \mathbf{X}} + \frac{\partial \mathbf{I}}{\partial \mathbf{Q}} \frac{\partial \mathbf{Q}}{\partial \mathbf{X}} \right) \frac{\partial \mathbf{X}}{\partial D_j}$$

A cheaper calculation is obtained in terms of memory, but now the system is dependent on the number of design variables [20]. To overcome this problem, the transpose derivative is used, obtaining the system

$$\frac{dI_i}{d\mathbf{D}}^T = \frac{\partial \mathbf{X}}{\partial \mathbf{D}}^T \left(\frac{\partial I_i}{\partial \mathbf{X}}^T + \frac{\partial \mathbf{Q}}{\partial \mathbf{X}}^T \frac{\partial I_i}{\partial \mathbf{Q}}^T \right) \tag{4}$$

that can be solved to obtain the sensitivities of each cost functions w.r.t all design variables and is weakly dependent on their number.

Now the actual steps to obtain each term of equation 4 will be described.

3.2 Primal and Adjoint Calculations

All the derivatives present in 4 can be computed once the solution of the discretised Navier Stokes equations is obtained, except the sensitivity of flow variables w.r.t mesh points that is computed with the adjoint solver itself.

The flow solution is obtained using discretised equations as in section 2. The nature of the residual will change if the simulation is setted as steady-state or time-dependent.

In a steady-state simulation, the residual of the converged solution indicates that real time variations are zero in the discretised domain. Thus, the residual $\mathbf{R}$ can be derived w.r.t the design variables:

$$\frac{d\mathbf{R}}{d\mathbf{D}} = \frac{d}{d\mathbf{D}} \{ \mathbf{R}[\mathbf{Q}(\mathbf{X}), \mathbf{X}] = 0$$

Using the chain rule:

$$\frac{\partial \mathbf{R}}{\partial \mathbf{Q}} \frac{\partial \mathbf{Q}}{\partial \mathbf{X}} + \frac{\partial \mathbf{R}}{\partial \mathbf{X}} = 0$$

$$\frac{\partial \mathbf{Q}}{\partial \mathbf{X}}^T = -\frac{\partial \mathbf{R}}{\partial \mathbf{X}}^T \frac{\partial \mathbf{R}}{\partial \mathbf{Q}}^{-T} \tag{5}$$

In a time-dependent simulation, the residual is a function of time and is the sum of the time derivative of flow quantities and the steady-state residual arising from the implicit solver [17]:

$$\mathbf{R}_n = \frac{\partial \mathbf{Q}_n}{\partial t} + \mathbf{R}_{st,n} \tag{6}$$

where the subscript n indicates the time-step.

In unsteady flows, cost functions can be a time average of the instantaneous value within a certain period of time. For these cases, an exhaustive derivation of equation 5 is present in [17].

In this paper, cost functions are chosen instantaneous. This choice is made because both lift and drag coefficient, in the simulation's asymptotic range, at angle of attack near the maximum lift to drag ratio, have little oscillations (see section 4), therefore an instantaneous value at a certain time-step is near the time averaged value.

Because the embedded adjoint solver of Star CCM+ used a steady residual to compute the sensitivities, problems could arise for unsteady residuals very different from their steady counterparts.

For this reason, once the simulation is in the asymptotic range, two additional steps of the implicit scheme are done, with a time-step of 5 order of magnitude lower than that chosen for the simulation.

Two steps are made because the time discretization is of second order accuracy, and with such a small time-step, the discretized time derivative in equation 6 is very close to the exact value and the simulation doesn't change much in time, remaining in the spot chosen.

Moreover, because the simulation is in the asymptotic range, the only causes of changes in time are the oscillations of the flow. Thus, for relatively small oscillating flows, the unsteady residual could be used in place of the steady one in the adjoint solver.

This statement needs to be verified after the optimization process.

Because inverting the matrix of sensitivity of the residual field w.r.t. the design variables is computational expensive, equation 5 is multiplied by the sensitivity of the cost function w.r.t. flow variables

$$\frac{\partial \mathbf{Q}}{\partial \mathbf{X}}^T \frac{\partial I_i}{\partial \mathbf{Q}}^T = -\frac{\partial \mathbf{R}}{\partial \mathbf{X}}^T \frac{\partial \mathbf{R}}{\partial \mathbf{Q}}^{-T} \frac{\partial I_i}{\partial \mathbf{Q}}^T = -\frac{\partial \mathbf{R}}{\partial \mathbf{X}}^T \frac{\partial I_i}{\partial \mathbf{R}}^T$$

The left-hand term represents the sensitivity of the cost function w.r.t. the mesh $\frac{\partial I_i}{\partial \mathbf{X}}$. The first term of the right-hand product is known once the primal solution and its residual fields are obtained. The second term of the product is a vector of the so-called adjoint variables.

The adjoint solver is used to solve the equation of the adjoint variable for each cost function. Then the adjoint variables of each cost function are applied to assembly the sensitivity of the cost function w.r.t. the design variables (equation 3).

Once the adjoint solver has computed the adjoint variables, all the derivatives except the sensitivity of the mesh points w.r.t. the design variables are known. The latter derivative is calculated solving a system resulting from using the radial basis functions morpher algorithm [20].

Radial basis functions are constructed starting from the set of design variables chosen. These functions are used to interpolate all the other points in the mesh.

A radial basis function is a function that only depends on the magnitude of his independent variable [11]. In this paper, multi-quadratic functions are chosen, which have the form:

$$\phi = \sqrt{r^2 + c^2}, \qquad r = ||\mathbf{x} - \mathbf{x}_i||$$

The resulting interpolation is:

$$s(\mathbf{x}) = \alpha 1 + \sum_{i=1}^{m} \lambda_i \phi(||\mathbf{x} - \mathbf{x}_i||)$$

Coefficients λ_i and $\alpha 1$ are computed using the m design points and the additional constraint [11]:

$$\sum_{i=1}^{m} \lambda_i = 0$$

Once the link between the mesh points and the design points is found, the evaluation of the last derivative can be done.

With all the derivative, the design points can be deformed in the direction of the derivative $\frac{dI_i}{d\mathbf{D}}$ (in a bidimensional domain it is a gradient). The entity of the deformation is a parameter that has to be set. The general equation that governs the displacement of the design points is ([23]):

$$\mathbf{d}_i = \mathbf{d}_{i-1} + hf(\nabla \mathbf{I}) \tag{7}$$

in which d_i and d_{i-1} are displacement vectors at the current and the previous iteration of the optimization process (in the first iteration $d_{i-1} = 0$), h is the magnitude of the displacement that has to be set and f is a function of all gradients of the cost functions, usually represents a weighted average. The displacement need to be small in order to approximate as linear every step of the steepest descent mechanism on which the adjoint is based. Mesh points are then recomputed using the radial basis functions.

With the new mesh, the process is restarted, and a loop is formed, in which the simulation is carried out on the new mesh, sensitivities are computed on the new solution and the mesh is deformed based on new sensitivities.

Now that all the tools used have been described, the aerodynamic characteristics of the initial airfoil are presented, so that the starting point for the optimization process is known.

4 Aerodynamic Characteristics of the Starting Airfoil

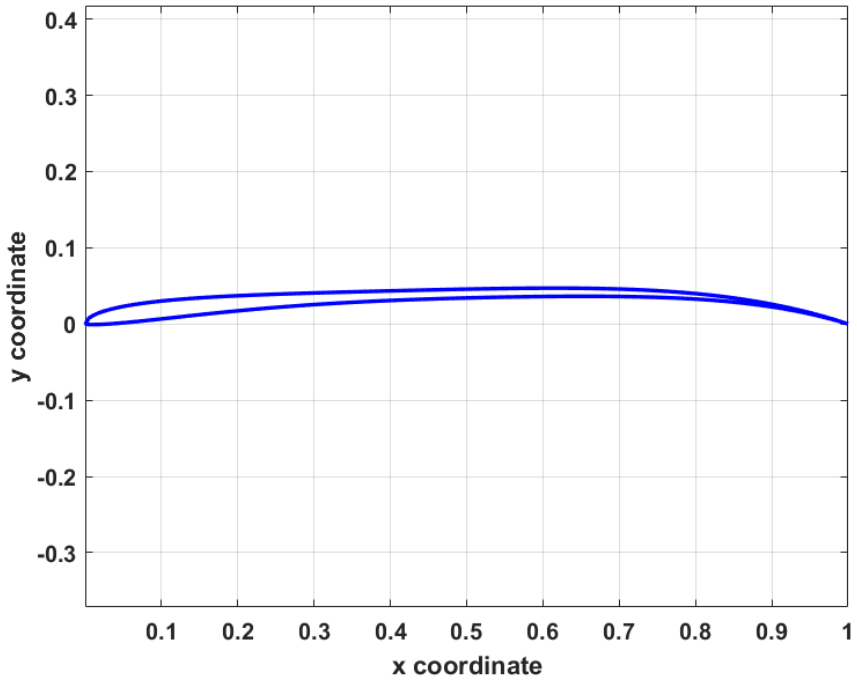

Figure 15: Geometry of the initial airfoil

The starting airfoil of all the optimization processes, as stated before, is an airfoil optimized at a condition of Re = 10000 and M = 0.5, for an optimum at a lift coefficient of 0.87. Figure 15 shows its geometry.

Principal features of the geometry are:

- maximum camber positioned around 60% of the chord;
- maximum thickness (about 6% of the chord) near the leading edge;
- flatness area in the centre part of the airfoil
- average thickness of 1.3% of the chord.

The airfoil is analysed with the procedure described in section 2. Conditions of the flow chosen for polars construction are:

1. $Re = 8000$, $M = 0.5$;
2. $Re = 10000$, $M = 0.5$;
3. $Re = 14000$, $M = 0.7$;

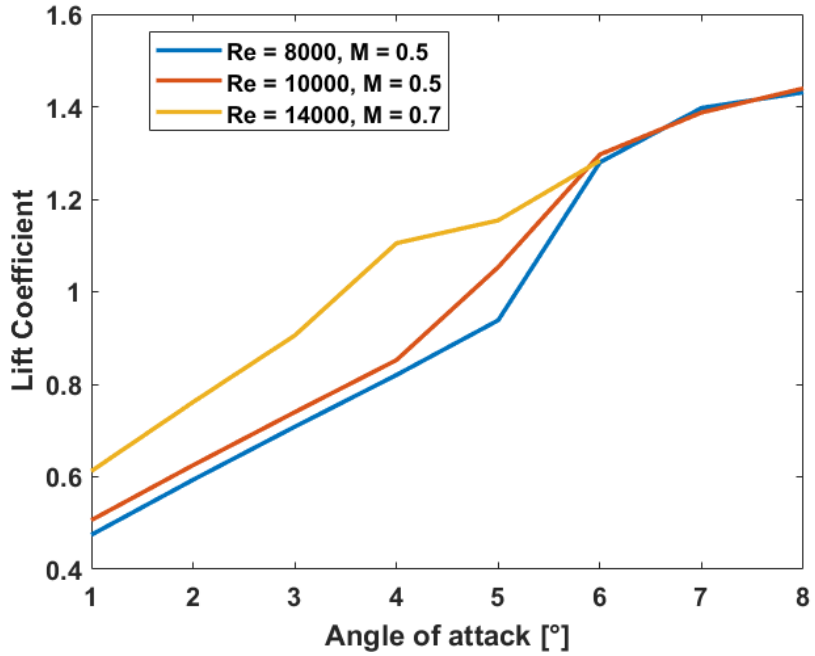

Figure 16: Averaged lift coefficient variation with angle of attack at three different flow conditions

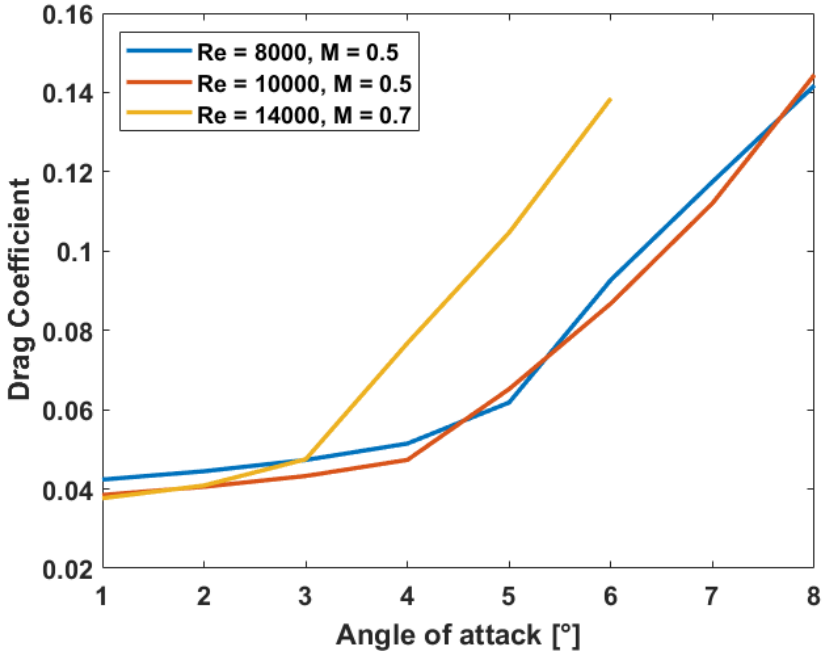

Figure 17: Averaged drag coefficient variation with angle of attack at three different flow conditions

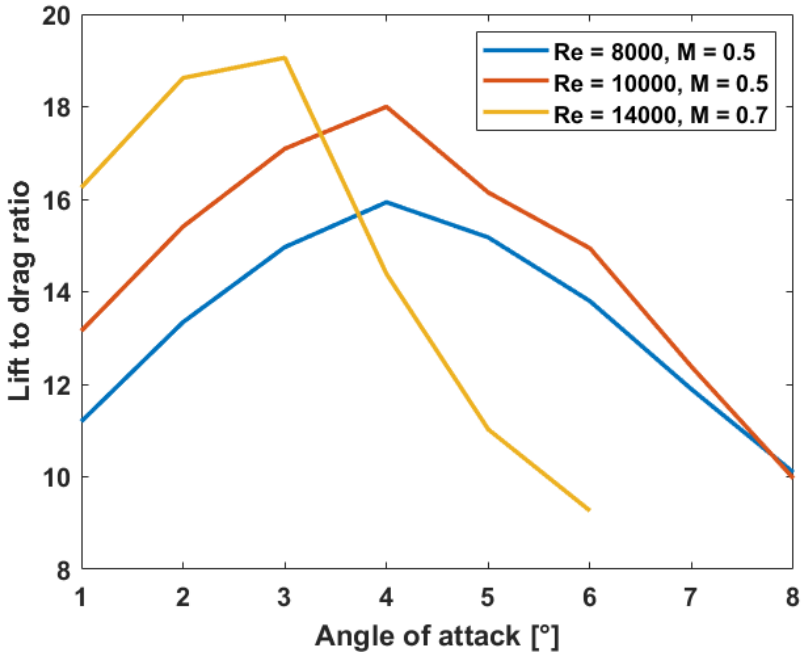

Figure 18: Averaged lift to drag ratio variation with angle of attack at three different flow conditions

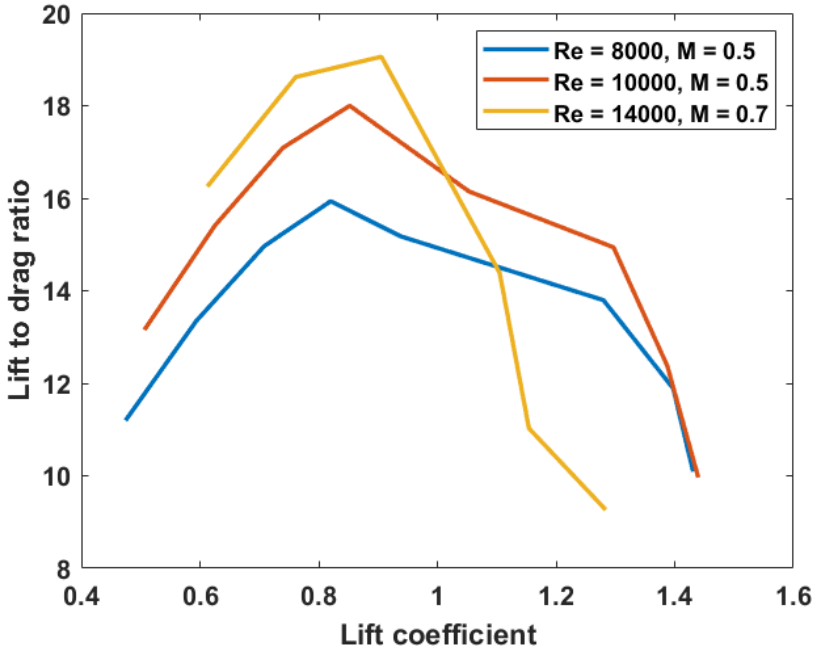

Figure 19: Averaged lift to drag ratio variation with lift coefficient at three different flow conditions

The second condition is the condition at which the initial airfoil is optimised, the first one is a condition that may be encountered near the blade root of a rotor. The last condition is the one at which the paper aims to, and can also be encountered at the blade tip. Therefore, the goal is to obtain an airfoil that, with the same atmosphere conditions, can fly more efficiently at greater speeds.

4.1 Airfoil Averaged Performance

Since the flow is unsteady, performance are time-averaged over the period of oscillations. If no clear period of oscillations is found, the average is done over a time window of 0.1 seconds. As it will be shown later, this period of time is large enough to contain, in the worst case, at least 20 period of oscillation.

Figures from 16 to 19 show the aerodynamics characteristic at the three conditions at different angles of attack. The maximum angle of attack is 7°because the optimization process will focus on the range in which the lift to drag ratio is near the maximum. Thus, flow conditions with angles above 7°and below 1°are not analysed.

The lift coefficient has the typical non-linear trend with two slopes: one at low angles of attack, the other one at angles of attack above the one at which the laminar separation bubble is formed (5°at Re = 8000). At angles above 6°, a leading edge separation occurs after the bubble *burst* and leads to airfoil stall, where the lift coefficient does not immediately decrease, but continue to increase at a weaker rate due to the presence of higher suction peak at increasing angles of attack.

The increase in Reynolds number from 8000 to 10000 leads to the formation of the laminar separation bubble at a lower angle of attack, due to the increased instability of the boundary layer. It is also present a slight increase in the lift coefficient at low angles, but the two trends has the same slopes.

The increase in speed, that cause the Mach and Reynolds number to become respectively 0.7 and 14000, induces a higher value of the lift coefficient at low angles of attack, thus the curve is slightly higher.

Laminar separation bubble formation starts between 3 and 4 degrees, at 5 degrees the flow is separated from the leading edge and oscillations contains high order harmonics, as can be seen in figure 24.

Interestingly, the increase in Mach and Reynolds numbers after leading edge separation ceases to produce higher lift coefficients, which at high angles of attack are approximately the same for all three conditions.

From the drag coefficient plot, it is clear that once a laminar separation bubble is formed, pressure drag increases and overall the drag coefficient is strongly incremented.

At low angles of attack, an increase in Reynolds number produces a decrease in viscous drag that causes the curves at high Reynolds number to be under that at Re = 8000.

Since at Re = 14000, and M = 0.7 the laminar separation bubble forms at lower angles of attack, and the lift coefficients have approximately the same slopes, the range in which the efficiency is high is much more restricted than that at the other conditions, as can be seen in the lift to drag ratio plots.

Prior to the formation of the bubble, lift to drag ratio curve of the third case is significantly higher than the other ones due to the increase in Reynolds number.

In general, it can be seen that the range of lift coefficients at which the present airfoil is performant is between 0.6 and 1.

4.2 Oscillations Behaviour

Variations of oscillations amplitude and frequency are shown in figure 21, 21 and 23.

Increasing angle of attack leads to greater oscillations amplitude and smaller frequency. It can be seen an abrupt variation, both in the amplitude and in the frequency, around the angles of attack at which the laminar separation bubble is formed. At these angles, the flow contains high order harmonics, as can be seen from figure 24,which represents the one-sided frequency spectrum of the time history of lift coefficients (which is also equal to that of the drag coefficients) at various angles of attack. At the first angle of attack, at which the laminar separation bubble is not yet formed, oscillations has a clear frequency and a single harmonic. When the bubble is formed or, afterward, when the flow is separated from the leading edge, high order harmonics appear and the frequency spectrum widens.

Figure 20 shows the difference in instantaneous vorticity field between the flow prior and after the abrupt variation described above. It can be seen the flow separated near the leading edge in the case with high amplitude of oscillations, and high order harmonics are caused by the interaction between the vortex shedding and the laminar separation bubble over the upper surface of the airfoil, as was already described in section 1.1.

Reynolds and Mach number effects are the shrinkage of the range of usability of the airfoil: amplitude of oscillations begin to increase at smaller angles of attack, making the airfoil impossible to control above these angles, due to large variations of forces in little time.

It is interesting to note that above 4°, the airfoil has the same frequency of oscillations at both Re = 10000 and Re = 14000, indicating that the flow structures when the leading edge is separated are not influenced by Mach and Reynolds numbers.

Finally, it can be noted that oscillations of drag are stronger than lift oscillations at the same angle of attack.

(a) Instantaneous vorticity field of the initial airfoil at Re = 8000, M = 0.5 and $\alpha = 5^{\circ}$

(b) Instantaneous vorticity field of the initial airfoil at Re = 8000, M = 0.5 and $\alpha = 6^{\circ}$

Figure 20: Comparison of vortex shedding between same flow conditions but different angles of attack

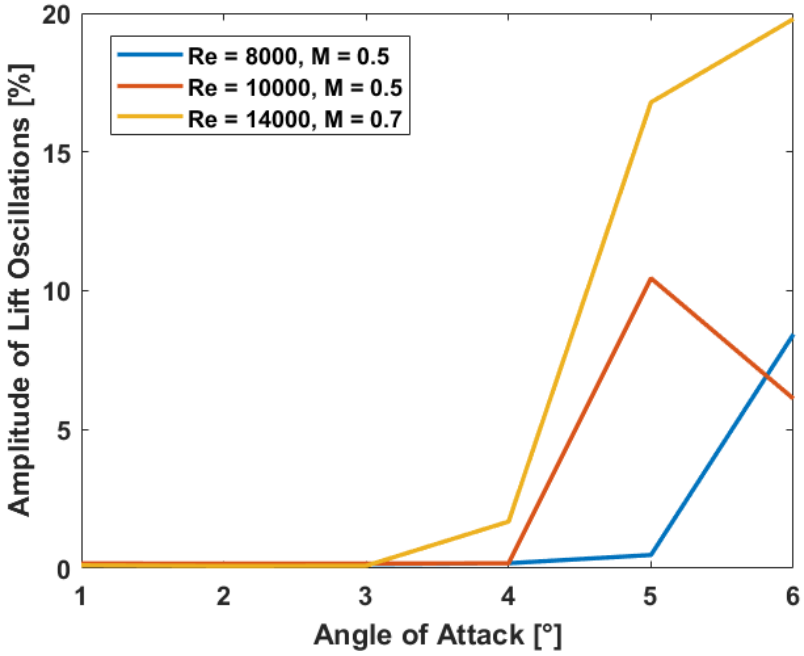

Figure 21: Lift coefficient oscillations from the mean value in percentage of mean value in function of the angle of attack at different flow conditions

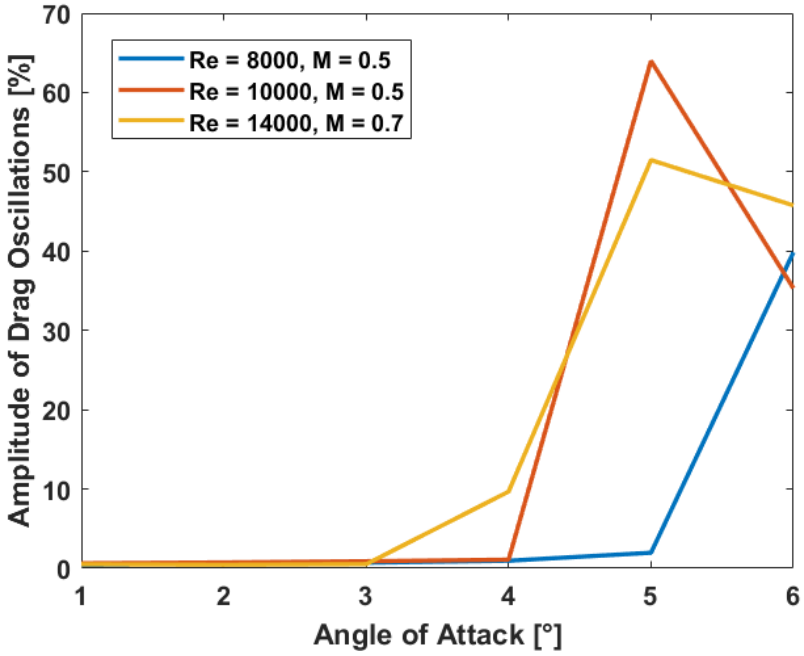

Figure 22: Drag coefficient oscillations from the mean value in percentage of mean value in function of the angle of attack at different flow conditions

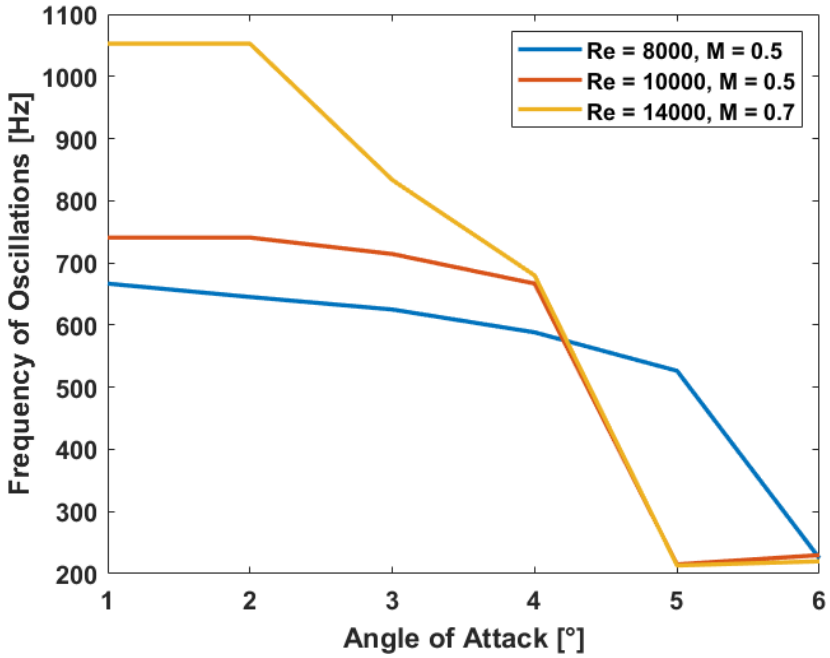

Figure 23: Frequency of oscillations in function of the angle of attack at different flow conditions

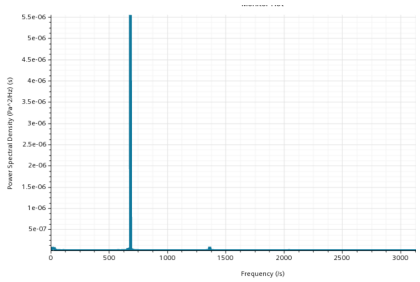

(a) One-sided frequency spectrum, α =4°

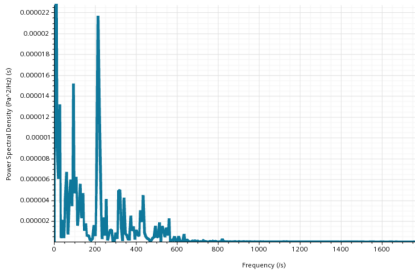

(b) One-sided frequency spectrum, α =5°

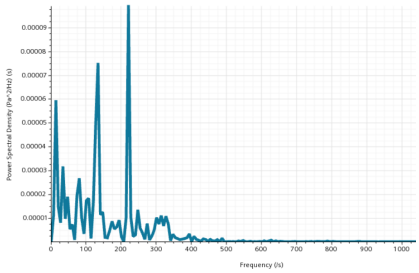

(c) One-sided frequency spectrum, α =6°

Figure 24: Comparison of frequency spectrum at different angles of attack of the initial airfoil at Re=14000, M = 0.7

5 Steady Adjoint Optimization: setups and problems

The airfoil aerodynamics characteristics highlight the unsteadiness of the flow at these Reynolds numbers. Oscillations due to vortex shedding influence the lift and drag coefficients. However, a case has to be made for using the embedded steady adjoint solver in Star CCM+.

The steady approximation greatly cuts down the computation time and the memory expense with respects to unsteady adjoint optimization. That is due to the updating of the solution after the deformation process. In the steady adjoint, once the mesh is deformed, a steady simulation is carried out with initial condition set with the precedent flow field. This field, for small deformation, will be almost equal to that computed in the process, thus, the solution converges in little time. In the unsteady adjoint, as will be described in section 6, after the mesh deformation, the unsteady simulation is continued until the transient due to the changing mesh is past. The transient may last $0.1 \div 0.2$ seconds, resulting in numerous iteration of the implicit scheme between two deformation of the mesh.

In addition, because the interest is not on the actual value of aerodynamics coefficients, instead it is in the general trend of sensitivity of the cost functions w.r.t the design points chosen, a larger error on the actual value of the coefficients can be accepted.

Moreover, as described in section 4, the intensity of vortex shedding is not

strong enough to influence heavily the performance at low angles of attack. In fact, at these angles, the vortex shedding is caused by trailing edge separation, and the flow over the airfoil is fully laminar. Therefore, approximating as steady the unsteady flow around the airfoil at low angle of attack leads to a small increase in the error committed predicting the pressure distribution over the airfoil.

The steady approximation and its consequence on the flow field and on these errors are described in the following part, and a steady adjoint optimization procedure is presented, together with two optimization.

5.1 Steady Approximation

When a simulation is steady-state, the time derivatives are neglected and the discretised compressible Navier-Stokes equations are solved using a pesudo-time marching procedure, in which a pseudo time-step is applied to the equations, updating field variables until residuals are small enough, that is, until the time derivative is near zero. In this case the residuals represent how much the solution is changed from the previous pseudo time-step, therefore if a steady state is reached, the residuals are small and the simulation is converged.

Simulations converge only in the case in which sources of unsteadiness in the flow are not strong enough to alter the solution. These source of unsteadiness can be separation of flow on the airfoil, vortex shedding, turbulence fluctuations, shock wave movement.

If these source modify a large part of the field, then the steady approximation is not usable, for it does not provide a converged solution.

For this reason, the approximation range of usability is restricted to flow at low angles of attack and low Mach number, in which, as shown in table 1, the error on the prediction of the pressure distribution is high anyway, but a converged solution, with which an adjoint optimization can be done, is obtained.

In table 1 value of lift and drag coefficients at low angles of attack for unsteady and steady simulations are compared. Coefficients of the unsteady simulations represents the mean value over the period of oscillation. The error is calculated as a percentage error relative to the unsteady value.

Errors increase with angles of attack, for the increasing unsteadiness of the flow due to stronger vortex shedding. Moreover, in conditions of higher Mach, they are significantly larger.

	Unsteady		Steady		Errors	
$\alpha\&M$	C_l	C_d	C_l	C_d	C_l	C_d
1°&0.5	0.4745	0.0424	0.4007	0.0404	15.556%	4.717%
2°&0.5	0.5935	0.0445	0.4963	0.0418	16.377%	6.067%
3°&0.5	0.7082	0.0473	0.5740	0.0437	18.949%	7.611%
4°&0.5	0.8201	0.5147	0.6330	0.0464	22.816%	9.877%
2°&0.7	0.6799	0.0495	0.5341	0.0449	21.444%	9.292%
3°&0.7	0.8231	0.0553	0.6149	0.0479	25.294%	13.382%

Table 1: Comparison of lift and drag coefficients for time-dependent and steady-state simulations

In addition, when the vortex shedding in the wake is evaluated with a steady procedure, a recirculation bubble, past the airfoil, is formed (figure 25).

Figure 25: Negative velocity zone past the initial airfoil at Re=8000, M = 0.5, with a steady-state simulation

This negative recirculating flow influence the flow past the entire airfoil, modifying its pressure distribution. On the upper surface, the expansion is weaker than that of the unsteady case, resulting in a smaller suction peak that justify the downward error in both lift and drag coefficients.

In figure 26b and 26a are compared the pressure distribution of the initial airfoil for a steady simulation at angle of attack of 2 degrees, with that at angle of attack of 1 and 2 degrees computed with a time-dependent simulation.

Figure 26a shows that the suction peak in the steady simulation is weaker, resulting in a pressure distribution over the upper surface entirely under that at the same angle of attack and with an unsteady simulation. The lower pressure distribution is comparable and doesn't change much decreasing the angle of attack, due to the flatness of the airfoil lower surface.

Figure 26b shows that the pressure distribution on the upper surface of the steady simulation, albeit with some differences, can be comparable with that of the unsteady simulation but at a lower angle of attack. In facts, as can be seen in table 1, the lift and drag coefficients of the steady simulations are always closer to that of the unsteady simulations at one degree lower of angle of attack.

This can be justified by the presence of the recirculation bubble, that influence the flow over the airfoil, deflecting it downward, resulting in an effective angle of attack over the airfoil of one degree lower.

Because the adjoint optimization needs a starting simulation, an analysis of its angle of attack has to consider the effects of the recirculation bubble.

The analysis for the starting simulation is done by considering some aspects of the optimization process.

Initial angle of attack has to permit the solution convergence. Moreover, for a performance enhancement, the range of angles of attack considered has to be near the angle of attack of maximum lift to drag ratio. This is done because the optimization that is done is a pure performance improvement, thus the aim is to increase the maximum lift to drag ratio.

An airfoil with high performance in a very restricted range of angles of attack is not ideal. Therefore, a multipoint approach is adopted.

This approach uses two or more starting simulations, the steady adjoint solver is used on all the simulations, obtaining two or more vectors, along which the mesh is deformed. These vectors are then combined to form a displacement vector that deform the airfoil and can potentially optimize the performance at all the angles of attack chosen. In this way, although the efficiency of the process is reduced, the performance of the airfoil is less punctual.

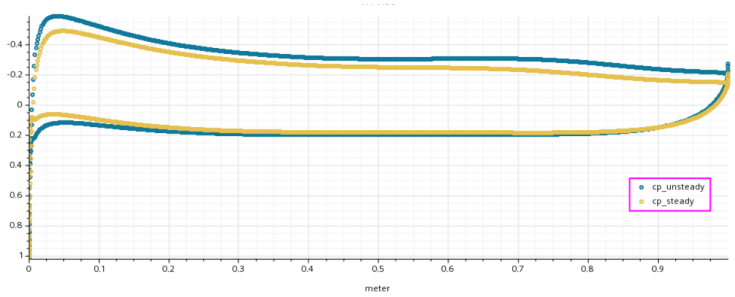

(a) Steady simulation pressure distribution at 2°, unsteady simulation pressure distribution at 2°

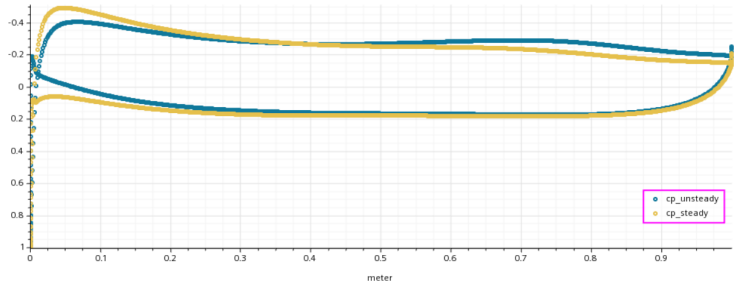

(b) Steady simulation pressure distribution at 2°, unsteady simulation pressure distribution at 1°

Figure 26: Comparison of pressure distribution over the initial airfoil at Re = 8000, M = 0.5, at different angle of attack and simulations setups

5.2 Multipoint Optimization Approach

As previously described, the multipoint optimization approach is paramount to obtain performance that are not punctual, that is, that are valid for a range of usability wide enough. This approach can also be used to widen the range of Reynolds or Mach number, by using simulations at different flow condition. However, Mach number, for the steady simulation to converge, cannot be in the higher part of the range selected.

Three simulation are chosen for the optimization. Angles of attack and flow conditions of the simulations need to be selected. Constraints for the selection are:

- higher angle of attack possible is 4 degrees;
- all angles will result in simulations with flow conditions similar to that of lower angles;
- Mach and Reynolds number has to be in the lower range, due to convergence problem

These constraints result in the following conditions for the simulations:

1. range of angles of attack: $1 \leq \alpha \leq 4$;
2. Reynolds number: Re = 8000;
3. Mach Number: M = 0.5.

Another choice to be made is the combination of displacement vectors resulting from the adjoint processes. A weighted averaged will be used for this purpose, in which the highest weight is assigned to the angle of attack closest to the maximum lift to drag ratio.

The final choice is which cost functions to use.

Since the embedded adjoint solver has the only option of maximizing the cost function, for a minimization process, this needs to be the negative of the function willing to minimize.

Two options are selected: the first optimization process will be carried out with lift to drag ratio as cost function, the second one will use a penalised drag cost function.

The penalised drag cost function is composed of two terms: the first is the negative of the drag coefficient, so that will be minimised. Because the minimization of the drag coefficients is probably accompanied by a decrease in lift coefficient, the latter is constraint to remain constant. Therefore, a penalisation function is summed to the drag coefficient.

The penalisation function chosen is a polynomial function. Since the process will maximize the cost function, the polynomial need a negative second derivative with a maximum near the point at which the lift coefficient has to remain constant.

Because a constant lift coefficient is too restricted for the optimization, the polynomial chosen has a maximum in a flat zone, thus the lift coefficient can vary in a small range.

The polynomial is:

$$y = -[C_l - (a-1)]^4 + (C_l - a)^3 - [C_l - (a+1)]^4 \tag{8}$$

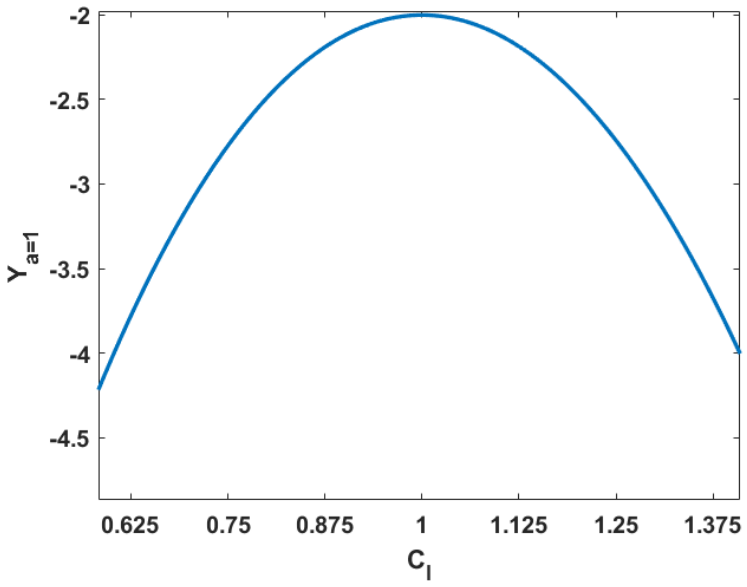

Figure 27: Polynomial of equations 8 with $a = 1$

in which "a" is a parameter that represents the value of the lift coefficient at which the optimization will ideally result. This value is chosen to be the lift coefficient at the angle of attack of the simulation in which the cost function is used. Figure 27 shows the form of the polynomial with $a = 1$ in the zone of the plateau.

The definitive cost function, dependent on the parameter "a", will be:

$$CF(a) = -C_d - [C_l - (a-1)]^4 + (C_l - a)^3 - [C_l - (a+1)]^4 \tag{9}$$

Finally, two optimization processes are obtained. Their parameters are highlights in table 2. The range of angles of attack for the drag minimization process is higher than that for the lift to drag ratio. This is because the drag coefficients at low angles increase weakly. The flatness of its curve in function of angle of attack, caused by the low pressure drag and almost constant friction drag, could lead the optimization process to simply reduce the chord length to reduce the drag. On the other hand, at medium angle of attack, where pressure drag start to be more noticeable, the curve slope rises and the optimization may act to reduce this rise.

Once the optimization process is selected, the design points need to be picked in number and position, together with the magnitude of the displacement of design points (h in equation 7).

To avoid the formation of dimples on the optimised airfoil, the design points are placed outside the boundary layer. This choice was made after various attempts with different offset from the surface of the design points. It has been seen that in cases where design points were inside the boundary layer, the resulting airfoil had dimples and little concavity on its surface (figure 28). Thus, for all the cases, offset is set equal to 0.06 meter.

		Optimization 1	Optimization 2
Simulation 1	Cost Function Angle of attack	C_l/C_d 1°	CF(0.4) 2.5°
Simulation 2	Cost Function Angle of attack	C_l/C_d 2°	CF(0.5) 3.5°
Simulation 3	Cost Function Angle of attack	C_l/C_d 3°	CF(0.6) 4.5°

Table 2: Optimizations parameters selected for the steady adjoint optimizations

The total number of point is 100, distributed around the airfoil, with the offset chosen. Figure 29 shows the design point for the Optimization 1 (see table 2).

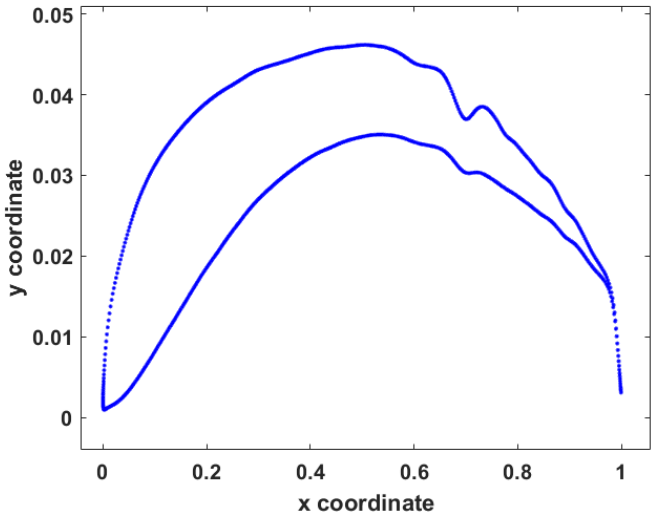

Figure 28: Shape of an airfoil optimised using design points with an offset of 0.02 meter at Re = 8000

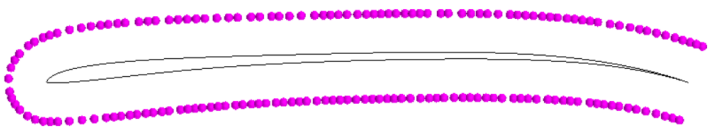

Figure 29: Distribution of design points around the airfoil

The magnitude of the displacement is not constant, but is set to change at every iteration. This is done because a constant maximum displacement in the field is wanted.

Since the derivatives evaluated in the adjoint solver are not normalised, the

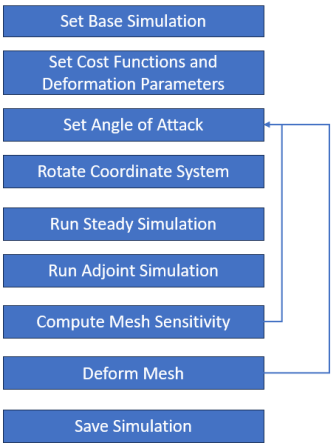

Figure 30: Steady Adjoint optimization process scheme

parameter h will contain the maximum of the gradients of the cost functions w.r.t the design points. In this way, the maximum displacement is always constant. The value of this displacement is then set to be equal to 0.5 millimetres, having to be small to maintain the linear approximation used in the gradient based optimization method.

Now that all parameters have been chosen, the steps of the optimization implemented in Star CCM+ are described.

5.3 Optimization Process Scheme

Thanks to the cheap computational cost of a steady-state simulation, it is not necessary to retain all the information of the previous iteration, as it will be in the unsteady adjoint procedure. Thus, the solution of the previous step is cancelled once the displacement of the iteration is computed.

For this reason, the memory usage is limited.

The simulation operations manager embedded in Star CCM+ is used for thee iterative algorithm.

The scheme of the procedure is described in figure 30.

First, a base simulation is setted. The domain is created and all the parameters and functions are created. Because in the adjoint optimization the importance is given to the trend of the derivative and not its actual value, the mesh can be weakly refined. The initial mesh is refined using a gradient based refinement function. This function is evaluated with a first steady-state simulation at the angle of attack in the middle of the range (for Optimization 1 : 2°, for Optimization 2: 3°).

Later, cost functions and displacement parameters are created.

The next step is the real iterative procedure. It is composed of two loops: an inner and an outer loop.

In the inner loop, a steady-state simulation is carried out using the first angle of attack to rotate the coordinate system of the flow, then the adjoint solver computed the adjoint variable and the mesh sensitivity is obtained. Mesh

sensitivity is then used to calculate the displacement vector, which is saved and stored.

The process is then repeated, closing the inner loop. For three angle of attack, there will be three displacement vectors stored.

Once the inner loop is finished, the three vectors are combined to form the total displacement vector with which the mesh is deformed. The outer loop is then closed, restarting the inner loop with the new mesh. The outer loop is stopped when a convergence on the cost function with adjoint iteration is reached.

Now, Optimization 1 and 2 will be described in details.

5.4 Optimization 1

The first optimization procedure uses the lift to drag ratio as cost functions. The range of angles of attack chosen are from 1 to 3 degrees. Because of the already described effect of the recirculation bubble past the leading edge, the effective angles of attack are from 0 to 2 degrees.

Starting value of lift to drag ratio are:

- at 1°$\rightarrow C_l/C_d = 11.62$;
- at 2°$\rightarrow C_l/C_d = 13.67$;
- at 3°$\rightarrow C_l/C_d = 15.17$;

Figure 31 shows the mesh used for the simulations, with 4 levels of refinement and an initial value of 0.25% of the base mesh, which is set to 0.9 meters. The total number of cells is around 31 thousands.

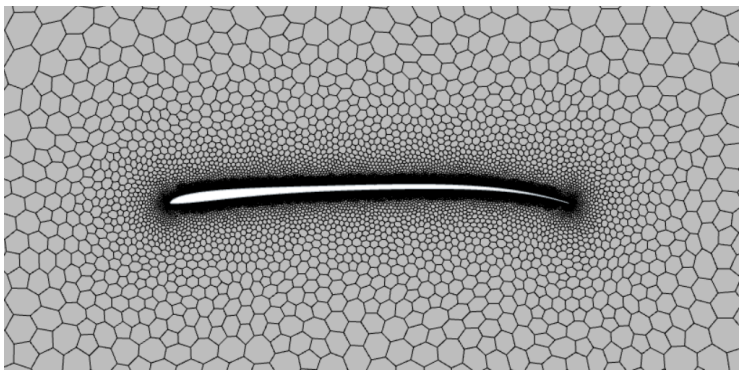

Figure 31: Detail of the mesh used for the Optimization 1

The design points are setted outside the boundary layer, and their displacement could produce a rotation of the airfoil. This can be blocked by setting to zero displacements of the point at the leading edge and trailing edge. However, because the range of angles of attack is not close to the maximum lift to drag ratio, this constraint is not applied, so that the airfoil can adjust its incidence while deforming.

At the end of the process, that has comprised 96 iteration of the outside loop described above, the airfoil is indeed rotated. The entity of the rotation is equal to -1.1°, resulting in an increase of angle of attack of that entity.

Final values of lift to drag ratio and their increase in percentage are:

- at 1°→ $C_l/C_d = 15.93$, corresponding to an increase of 37.09%;
- at 2°→ $C_l/C_d = 17.01$, corresponding to an increase of 24.43%;
- at 3°→ $C_l/C_d = 17.38$, corresponding to an increase of 14.57%;

These values are evaluated with the steady-state simulations, thus they are affected by large errors. It is noticeable that the rotation of the airfoil leads it to be in the range of angles of attack closer to the maximum lift to drag ratio.

Because of this tendency of the steady adjoint optimization, the gradients originating from lower angles of attack are stronger than that originating from angles closer to the maximum lift to drag ratio.

Figure 32 shows the convergence of the cost functions during the iteration. The stronger "thrust" given by the optimization to the simulations at lower angles of attack helps the airfoil to widen his range of usability.

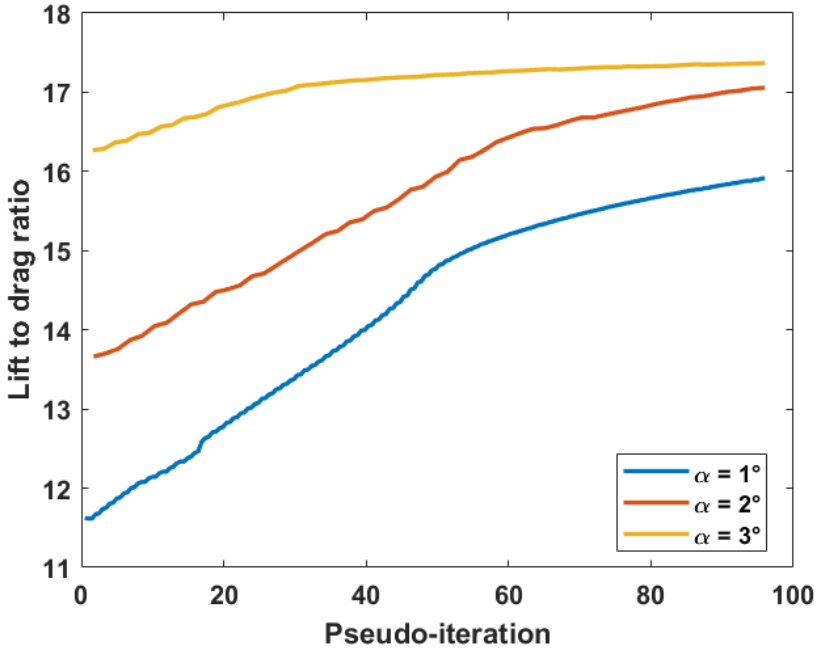

Figure 32: Lift to drag ratio in function of adjoint iterations for Optimization 1

Figure 33 shows the optimised airfoil compared with the initial airfoil. A trailing edge curvature is present, that increase the bottom loading. Overall, the curvature of the profile is increased, with a slight decrease in thickness in the aft part of the airfoil.

5.5 Optimization 2

In the second optimization, cost functions used are that of equations 9. The choice of the parameters is done after the first steady-state simulation. Lift coef-

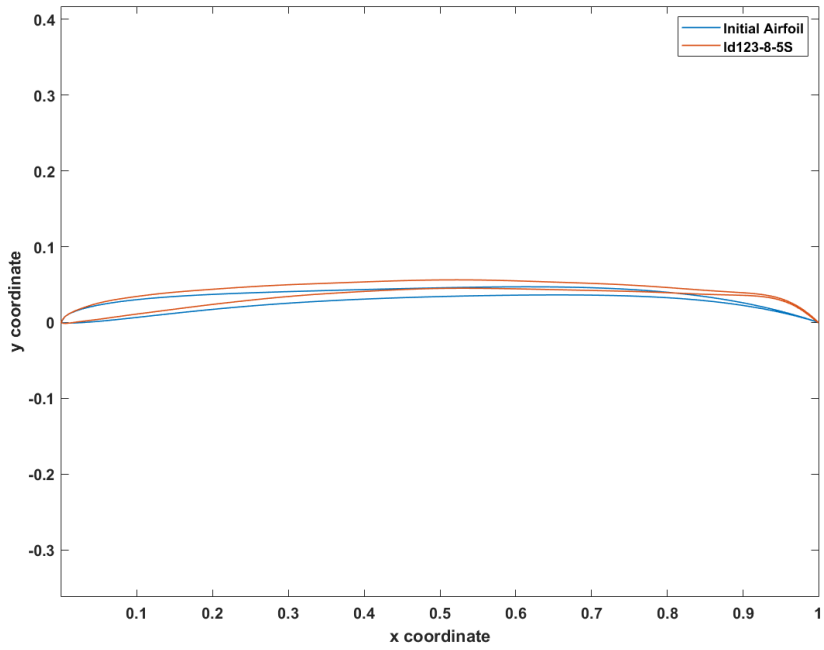

Figure 33: Comparison of the initial airfoil and ld123-8-5S (see appendix A)

ficients are evaluated and the a in the equations is substituted by the respective lift coefficient, obtaining three different cost functions.

It has been shown that the lift coefficients can vary between a range of $0.2 \div 0.3$, while the drag coefficients are minimised.

In this optimization, as in the previous, the rotation of the airfoil is not blocked, although the fact that the lift coefficient can vary only slightly, blocks the rotation itself, because a rotation will produce a variation in angle of attack and a subsequent variation in lift coefficient.

Starting value of lift to drag ratio are:

- at $2.5°\rightarrow C_l/C_d = 14.50$;
- at $3.5°\rightarrow C_l/C_d = 15.74$;
- at $4.5°\rightarrow C_l/C_d = 16.27$;

To monitor the variation of the drag coefficients, they are hereby presented:

- at $2.5°\rightarrow C_d = 0.0441$;
- at $3.5°\rightarrow C_d = 0.0469$;
- at $4.5°\rightarrow C_d = 0.0511$

Figure 34 shows the mesh used for the simulations, with 4 levels of refinement and an initial value of 0.2% of the base mesh, which is set to 0.8 meters. The total number of cells is around 40 thousands.

At the end of the process, that lasted 78 iteration of the outer loop, the values of lift to drag ratio and drag coefficient are:

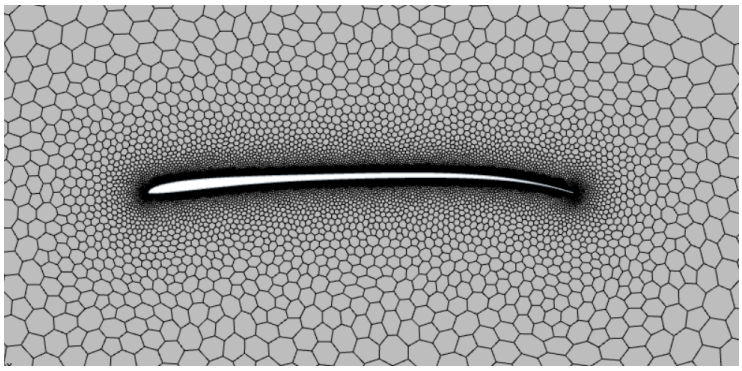

Figure 34: Detail of the mesh used for the Optimization 2

- at 2°→ $C_d = 0.0417$, $C_l/C_d = 15.18$ corresponding to a decrease of 5.44% in drag and to an increase of 4.69% in lift to drag ratio;
- at 3°→ $C_d = 0.0444$, $C_l/C_d = 16.64$ corresponding to a decrease of 5.33% in drag and to an increase of 5.71% in lift to drag ratio;
- at 4°→ $C_d = 0.0505$, $C_l/C_d = 17.00$ corresponding to a decrease of 1.17% in drag and to an increase of 4.49% in lift to drag ratio.

Figure 35 and 36 show the convergence of the lift to drag ratio throughout the iterations and the comparison of the initial airfoil with the optimised one.

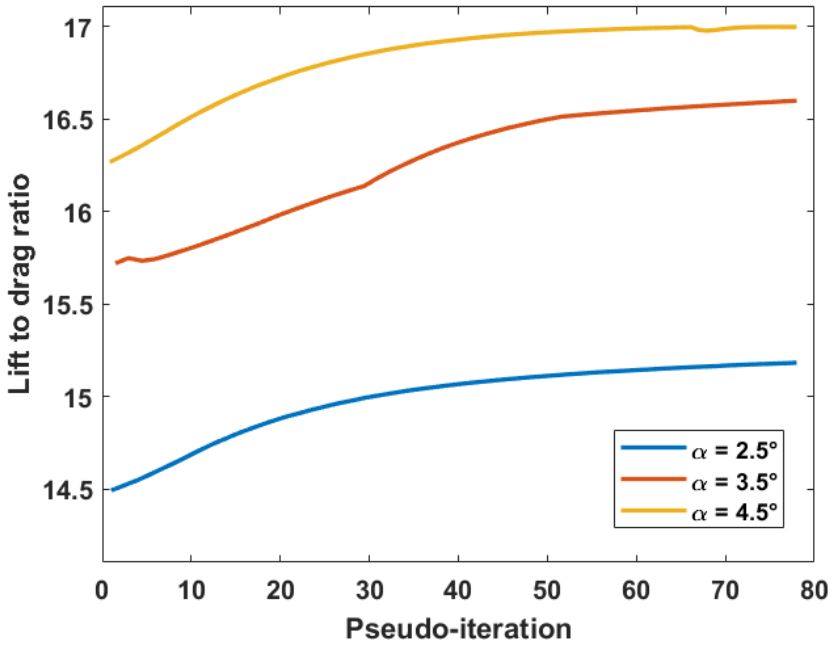

Figure 35: Lift to drag ratio in function of adjoint iterations for Optimization 2

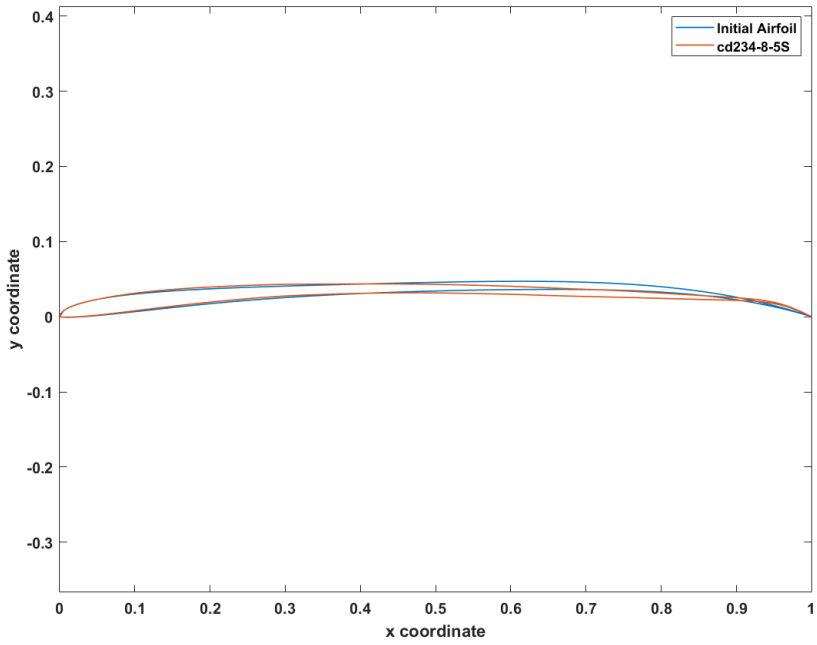

Figure 36: Comparison of the initial airfoil and cd234-8-5S (see appendix A)

It can be seen a reduction in curvature of the airfoil. The lower curvature helps the airfoil to produce less pressure drag, thus reducing the total drag at the same angle of attack. The negative effect is a reduction in lift coefficient, that, thanks to the penalisation function, is weaker than the decrease in drag coefficients, thus producing an increase in lift to drag ratio.

6 Unsteady Adjoint Optimization: Setups and Problems

After the two optimization processes described above, focus will move to the unsteady adjoint optimization.

As already stated, the need for an unsteady adjoint process is born to solve optimization problems where the flow is highly unsteady, and a steady-state simulation either will not converge or will converge to a solution containing non-negligible errors.

In this paper, the starting point of the optimization process is a simulation at Mach equals to 0.7.

After the steady adjoint at M=0.5, which has given notable results, obtaining airfoils that are better than the initial one also in transonic flows, now the unsteady adjoint procedure used will be described.

6.1 Optimization Procedure

The unsteady adjoint, unlike the steady adjoint, has high computational cost and memory usage. The computational cost is increased, with respect to the steady adjoint, by the simulations runs, while the memory usage is increased by the need to save the previous simulations to save some computation time.

Simulations are carried out in a time-dependent analysis, and after the deformation of the mesh, re-starting the simulations can be very expensive, because the simulations need to reach an asymptotic range and that could take some computational time.

To make the process cheaper, the field of pressure, velocity and temperature of the previous iteration are saved prior to the deformation of the mesh. Then they are used as initial conditions for the simulations after the deformation.

Since the deformation of the mesh is little for choice, the initial conditions are close to the actual asymptotic range of the new simulation, thus, the transient lasts less.

This trick saves some time, but usage of memory increases, especially with high cells count meshes.

For these reasons, the multipoint approach used in the steady adjoint processes is used with only two points. Thus, there will be two starting simulations.

These simulations, to save time, are taken from the simulations used for the reconstruction of the polar of the initial airfoil.

6.1.1 Treatment of the Mesh

In the steady adjoint, the mesh was refined for the central case of the multipoint approach. Here, an average mesh between the two case of the multipoint has been taken instead.

Since the starting simulations are already obtained, refinements of the meshes are known. The refinement is defined in a way that it will be a function of the base mesh size: the initial value of each level is a fraction of the base mesh size, thus, changing the mesh size will change the initial value and the refinement.

Because in the adjoint process a high cell counts is not needed, the base mesh size is increased, diminishing the number of cells.

Then, the base mesh is refined using the two new refinement function combined, obtaining an average mesh.

Figure 37 show the refinement levels of one of the mesh used for the adjoint unsteady optimization.

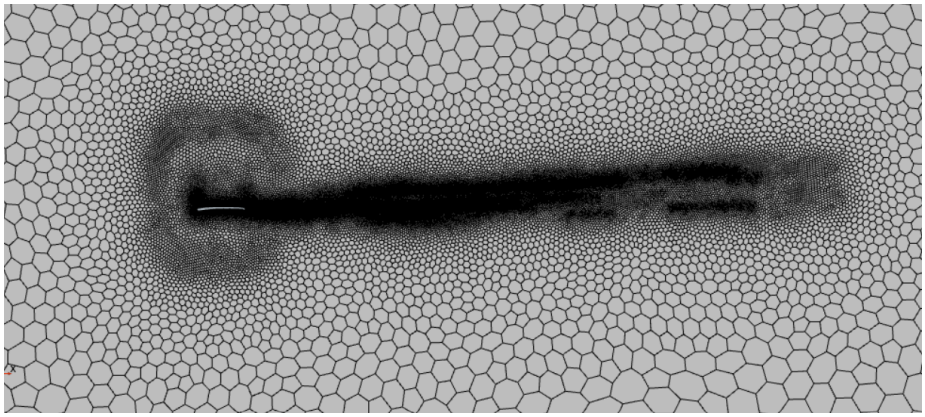

Figure 37: Details of the refinement of the average mesh used in Optimization 4

On the average mesh, the design points are constructed, with an offset of 6 centimetres from the airfoil, as in the previous cases.

6.1.2 Algorithm Scheme

Figure 38 shows the algorithm scheme for the adjoint unsteady optimization.

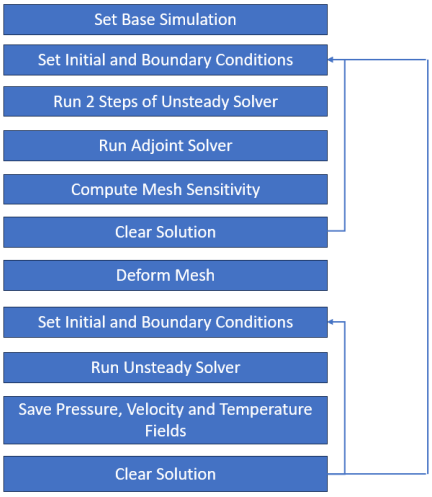

Figure 38: Algorithm scheme of the Unsteady Adjoint Optimization

The procedure is made of two inner loops and an outer loop.

First a base simulation is loaded: this simulation contains the average mesh, the cost functions and all the parameters for the deformation. Furthermore,

the base simulation has to contain the pressure, temperature, and velocity field of the simulations at the angles of attack chosen. Then the outer loop starts. The outer loop is made of two inner loops, one for the calculation of the mesh sensitivity at each angle of attack chosen, one for the runs of the simulations after the deformation of the mesh.

In detail, the first loop uses the saved flow fields of one angle of attack as initial conditions, then compute the unsteady residual after two iteration of the implicit scheme. With this residual, the adjoint solver is used to calculate the mesh sensitivity. Then the simulation is cleared, and the loop is iterated for all the angle of attack (in this case there are only two angles of attack). Therefore, saved flow fields at the other angle of attack are used as new initial conditions and the other mesh sensitivity is found.

The two vector of displacement are computed and combined to form the total displacement with which the mesh is deformed. As in the steady case, the total displacement is the average of the two initial displacement.

Once the mesh is deformed, the second inner loop starts: the flow fields are newly used as initial conditions for one angle of attack and now a number of steps of the implicit are made to get past the transient of the simulations that is caused by the mesh deformation. As the transient is passed, the flow fields are updated and the solution is cleared. Then the second inner loop is iterated for all the angle of attack.

At the end of the second inner loop, new flow fields with the new mesh for all the angles of attack are obtained, and the outer loop can be iterated.

The clearing of the solutions is necessary to give the simulations a new initial conditions. Thus, because the simulations are cleared at every iteration of every loop, to see the convergence of the scheme, simulations are saved at the end of the second loop every ten iteration of the outer loop.

6.1.3 Choice of Flow Conditions and Cost Functions

Once the procedure is setted, flow conditions of the starting simulations need to be selected.

With the unsteady adjoint optimization, this choice is not restricted to case at low angle of attack and low Mach number. In fact, this restriction has been made to avoid convergence problems on steady-state simulations. Since in the unsteady case, the simulations are time-dependent, it can be chosen a flow condition with high unsteadiness.

Two flow conditions are selected:

- Re = 8000, M = 0.7;
- Re = 14000, M = 0.7;

The first condition is chosen to compare results with the unsteady adjoint and the steady adjoint. Although the case in the unsteady optimization is at a higher Mach number, the predominance of the Reynolds number allows a comparison.

The second condition is chosen to optimize the flow conditions at which the airfoils in this paper are aimed to fly.

The second selection to make is what type of cost function to use. Because the penalisation function used in the steady adjoint optimisation need to be

setted properly to give good results, and since the airfoil optimized with the lift to drag ratio cost function has given better peak results, the lift to drag ratio has been chosen for the cost functions.

As stated above, the cost function is instantaneous in the treatment of the adjoint solver. To allow for an averaged optimization, it has been tried a different approach in one of the optimization: flow fields are averaged in time and in the first inner loop are used to initialize the two steps run. Because of the small time-step, the average solution doesn't change too much, thus the adjoint uses flow variables that are averaged. Then in the second loop, instantaneous flow field are used to pass the transient.

This approach has been used for one optimization at flow conditions of Re = 8000 and M = 0.7. Other two optimizations are done with instantaneous cost functions: one at the same flow conditions as the previous one (for a comparison of results), one at Re = 14000 and M = 0.7 (choice made after it has been seen that the results were better for instantaneous value).

All three optimizations use simulations with angles of attack of 3 and 4 degrees. These angles are selected because the maximum lift to drag ratio lies close to these values.

Table 3 summarize the parameters of the three procedure.

	Re	M	Cost Function	α
Optimization 3	8000	0.7	C_l/C_d averaged	3°
	8000	0.7	C_l/C_d averaged	4°
Optimization 4	8000	0.7	C_l/C_d	3°
	8000	0.7	C_l/C_d	4°
Optimization 5	14000	0.7	C_l/C_d	3°
	14000	0.7	C_l/C_d	4°

Table 3: Optimizations parameters selected for the unsteady adjoint optimizations

6.2 Optimization 3

In this optimization process, averaged flow fields are used for computing the derivatives used to calculate the mesh sensitivity.

This method, besides saving the instantaneous flow field at the end of the implicit iterations once an asymptotic range is reached, saves also the averaged field. Thus, the memory usage is higher than the method used in optimization 4 and 5.

Flow conditions are at Reynolds and Mach number of 8000 and 0.7.

The starting values of lift to drag ratio, at 3 and 4-degree angle of attack, are:

- $\alpha = 3° \rightarrow C_l/C_d = 14.89$;
- $\alpha = 4° \rightarrow C_l/C_d = 13.80$.

As already described, at the same Reynolds number, an increase in Mach number makes the maximum lift to drag ratio to move at lower angles of attack.

The mesh used is the one in figure 37 and contains around 64 thousands cells.

Figure 39 shows the convergence of the averaged lift to drag ratio with the outer loop iterations. One point every 10 iterations is saved. Total number of iterations is 130.

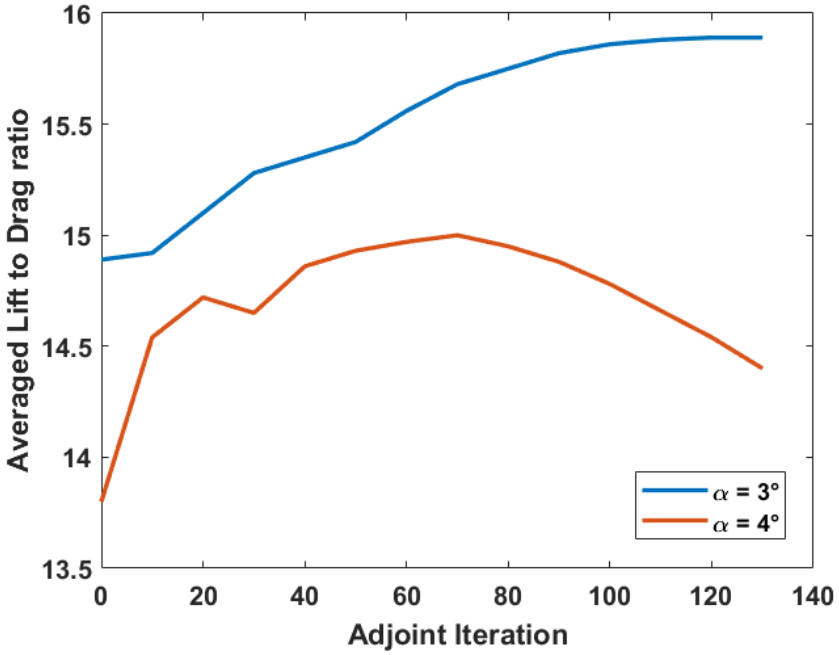

Figure 39: Convergence of lift to drag ratio value, at the two angles of attack chosen, for Optimization 3

While at 3°the lift to drag ratio converges to a value of 15.89, at 4°the cost functions doesn't converge, but has a peak value and then starts to decrease. One fact that has to be taken in considerations is that at 4°, in these flow conditions, airfoil is past its angle of attack of maximum performance, therefore this angle is not so relevant for the purposes of optimization of maximum performances.

Since the target is also to widen the range of usability, it has been chosen to take the geometry of the airfoil at the 100th iteration, thus the value at 3°is almost converged, while the value at 4°, although past the maximum, is not decreased too much.

Final values of lift to drag ratio and their relative increments are:

- at 3°: $C_l/C_d = 15.86$, corresponding to an increase of 6.51%;
- at 4°: $C_l/C_d = 14.78$, corresponding to an increase of 7.10%;

The geometry obtained is that in figure 40, compared to that of the initial airfoil.

It can be seen that, although to a less extent than in Optimization 1, the curvature of the airfoil has been increased, and the maximum camber is shifted

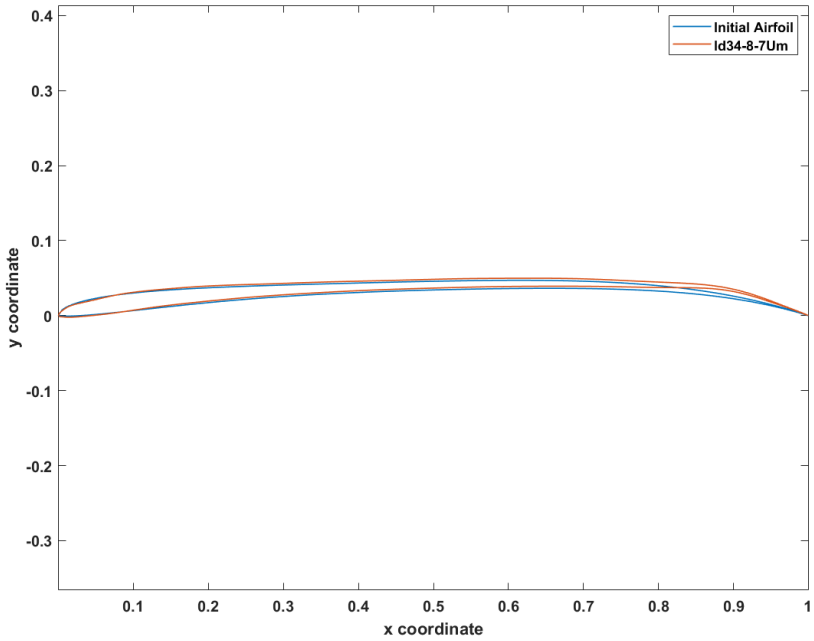

Figure 40: Comparison of the geometry obtained with Optimization 3 and that of the initial airfoil

rearwards, with a pronounced deviation near the trailing edge, that resembles a trailing edge flap.

6.3 Optimization 4

Optimization 4 is done to compare the resultant geometry of an optimization with instantaneous cost functions and averaged ones. Thus, flow conditions and starting value of the lift to drag ratio are the same as Optimization 3.

The total number of iterations of the outer loop done is the same (130), to better compare the results of the procedure.

In this case, both the value at 3°and 4°increase and converge (figure 41), thus the final geometry taken is the one at the last iteration.

Final values of lift to drag ratio and their relative increments are:

- at 3°: $C_l/C_d = 16.57$, corresponding to an increase of 11.28%;
- at 4°: $C_l/C_d = 16.34$, corresponding to an increase of 18.41%;

The geometry of the optimized airfoil is shown in figure 42, compared with that of the initial airfoil.

Even in this case, the optimised airfoil has a greater curvature and its maximum camber is closer to the trailing edge than the initial airfoil.

This airfoil shows a feature similar to that of the airfoil provides by the Optimization 5, that is a leading edge flap. In this case, the flap is less visible than in the next airfoil.

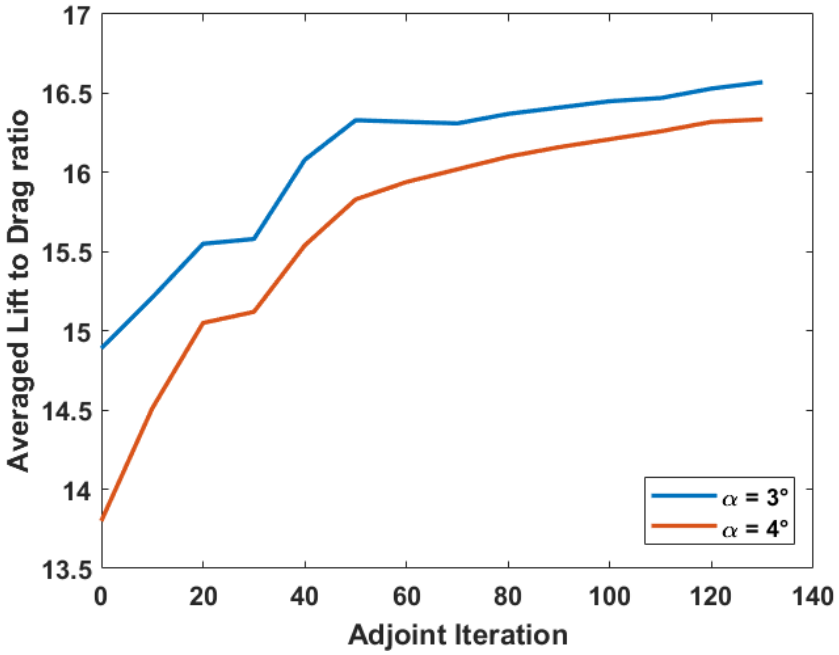

Figure 41: Evolution of values of lift to drag ratio with iterations of the outer loop for Optimization 4

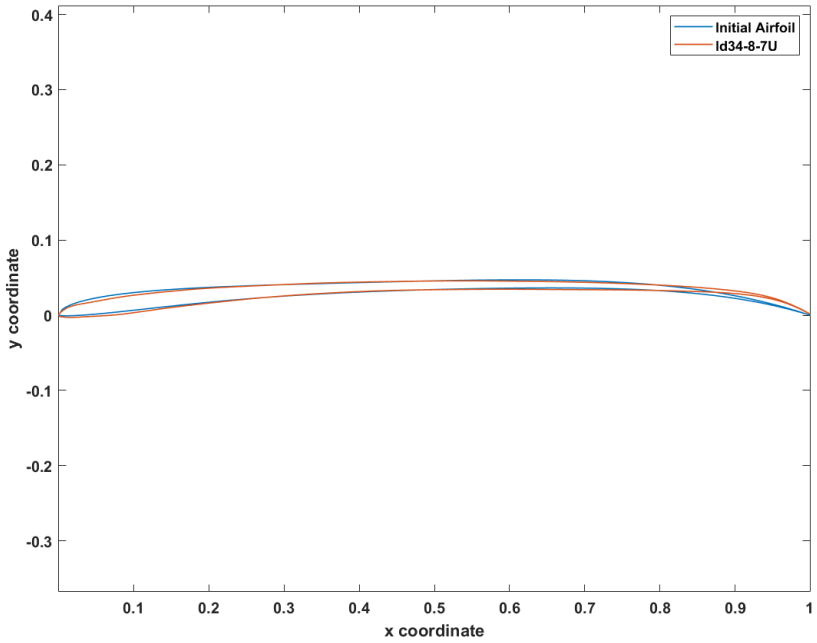

Figure 42: Comparison of the geometry of the initial airfoil with that provided by the Optimization 4

6.4 Optimization 5

Optimization 5 is the last optimization and uses the information extracted from the previous optimizations. The cost function used is the lift to drag ratio, since in the steady adjoint the optimization with the lift to drag ratio has shown the better improvement in pure performance. The cost function is chosen to be instantaneous instead of averaged, because in the last two optimizations, the one with the instantaneous value has shown greater improvements.

Flow conditions are the ones at which the initial goal of the optimization was aiming, i.e. Re = 14000 and M = 0.7.

Initial values of lift to drag ratio are:

- $\alpha = 3° \rightarrow C_l/C_d = 19.05$;
- $\alpha = 4° \rightarrow C_l/C_d = 14.39$.

The flow at 4°, in these conditions, is highly oscillatory, with amplitude of lift and drag coefficients oscillations respectively of 1.7% and 9.7%. This angle of attack is chosen to verify if the unsteady residual can be used in the steady adjoint solver, although the intensity of time changes is high (the usability of the unsteady residual with low intensity time changes is verified by the good results of optimization 3 and 4, where oscillations was of low intensity at all angles of attack).

The rotation of the airfoil is not blocked, therefore displacements from the adjoint are expected to reduce the effective angle of attack, bringing it closer to that of the maximum lift to drag ratio.

Figure 43 shows the convergence of lift to drag ratio at both the angles of attack. Because the airfoil is rotating by means of the deformation, it is possible that at some iteration the value of the cost functions is decreased, but the average value at the two angles of attack is increasing. For this reason, the evolution of the average value of the lift to drag ratio between the two angles of attack is also presented.

The total number of iterations is 70, because the deformation of the geometry was so high that the resulting mesh was poor at the end of the iterations, and continuing further the optimization procedure is resulted in a mesh with negative volume.

The resulting airfoil, compared with the initial airfoil, is shown in figure 44.

The geometry is changed a lot more than the other airfoils. It appears the usual trailing edge flap, but there is also a leading edge flap. Geometry is similar to that analysed in [21], that has given good results.

The leading edge flap helps the formation of a laminar separation bubble and its reattachment near the leading edge. In this way, the bubble is short, and its height is not great enough to produce significant increase in pressure drag. Therefore, the beneficial effect of the separation bubble, i.e. a decrease in viscous drag because of negative wall shear stress, is exploited without the typical consequences of a long laminar separation bubble.

At the optimum angle of attack, a short laminar separation bubble forms also in the aft part of the airfoil, further reducing the viscous drag.

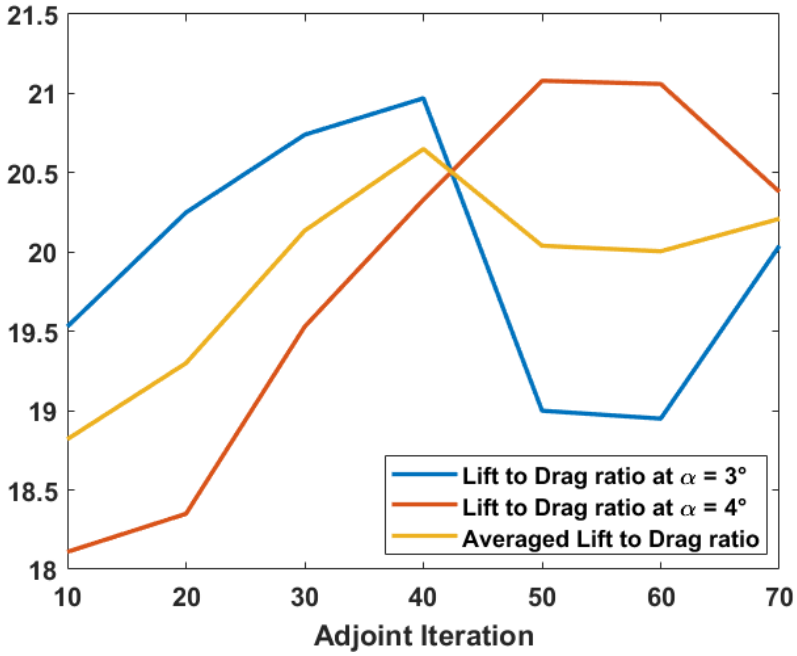

Figure 43: Evolution of lift to drag ratio, at the two angles of attack chosen and their mean value, for Optimization 5

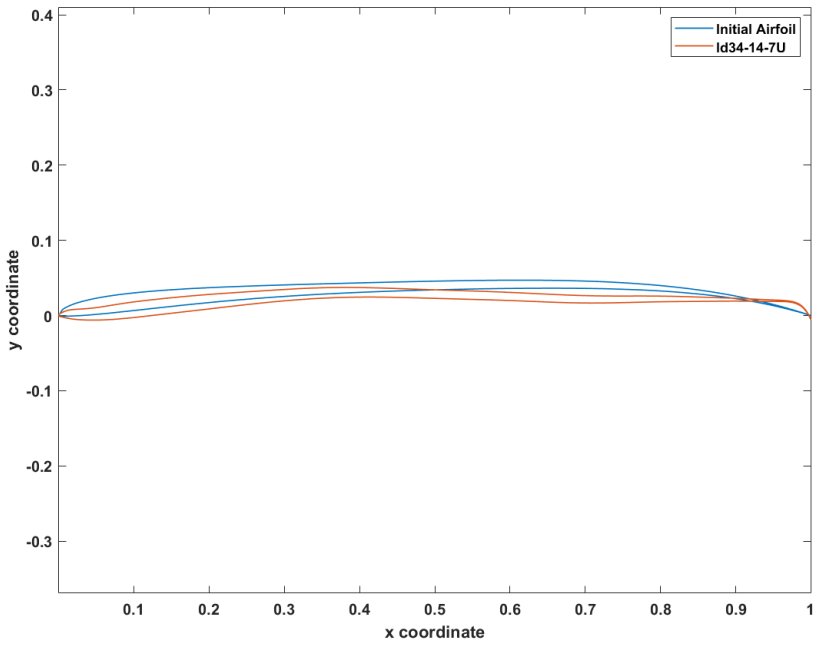

Figure 44: Comparison of the geometry of the initial airfoil and ld34-14-7U (see appendix A)

7 Results

All the performance of the airfoils optimised are presented in this section, both in terms of averaged value and in terms of oscillations. In the end, tables 4, 5 and 6 are present, summarizing all results at maximum lift to drag ratio conditions.

7.1 Airfoil 1

7.1.1 Averaged Performances

The first airfoil, obtained with the steady adjoint procedure, has a maximum camber closer to the trailing edge than the initial airfoil. Moreover, the overall curvature is increased. The first geometry change induces a greater bottom loading, which, combined with the second change, causes a shift in the $C_l - \alpha$ curve. Thus, the airfoil produces a greater lift than the initial airfoil at the same angle of attack.

Since the boundary layer is thick at the trailing edge, an increase in curvature localised in this zone produces little change in drag coefficient. The overall increase in the drag coefficient seen in figure 46 is caused by the total curvature increment of the airfoil, which causes a rise in pressure drag, but of lower strength than the increase in lift coefficient.

The lift to drag ratio is increased at low angles of attack, but because the lift curve is shifted upwards, the lift coefficient corresponding to maximum lift to drag ratio is increased from a value near 0.8 to a value of 1 at all flow conditions analysed.

Because of the increase in lift coefficients, there could be problems in the use of this airfoil: if the middle flow condition is taken as reference, using this airfoil rather than the initial airfoil requires flying at a velocity 10% lower, at the same aircraft weight. Thus, the flying Reynolds number is decreased to a value closer to the first flow conditions, resulting in a reduced lift to drag ratio.

7.1.2 Oscillations' Behaviour

The oscillations' behaviour of the airfoil, compared to the behaviour of the initial airfoil, is shown in figure from 49 to 51.

General trends of the initial airfoil are followed, with an increased in oscillation strength once the flow is separated from the leading edge. This effect is due to the higher lift coefficient at which the flow separate.

7.2 Airfoil 2

7.2.1 Averaged Performances

Figures from 52 to 55 show the averaged performances of the *cd234-8-5S*. Since the conditions of the flow in the simulations used in the optimization process are the first conditions, at this Reynolds number the penalisation function helps the lift coefficient to remain constant. Once the Reynolds is increased, the lift coefficient tends to reduced with respect to the lift coefficient of the initial airfoil. Therefore, the increase in lift to drag ratio caused by the reduction in drag is mitigated, and values of the lift to drag ratio are close to that of the initial airfoil.

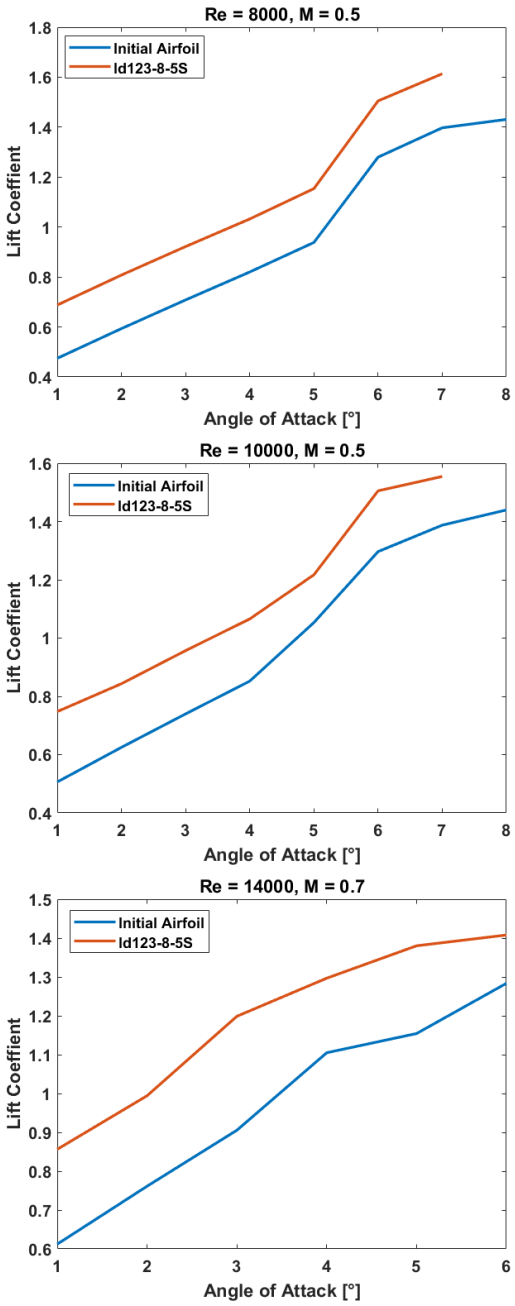

Figure 45: Averaged lift coefficient variations with angle of attack at different Reynolds and Mach numbers of ld123-8-5S compared to the initial airfoil

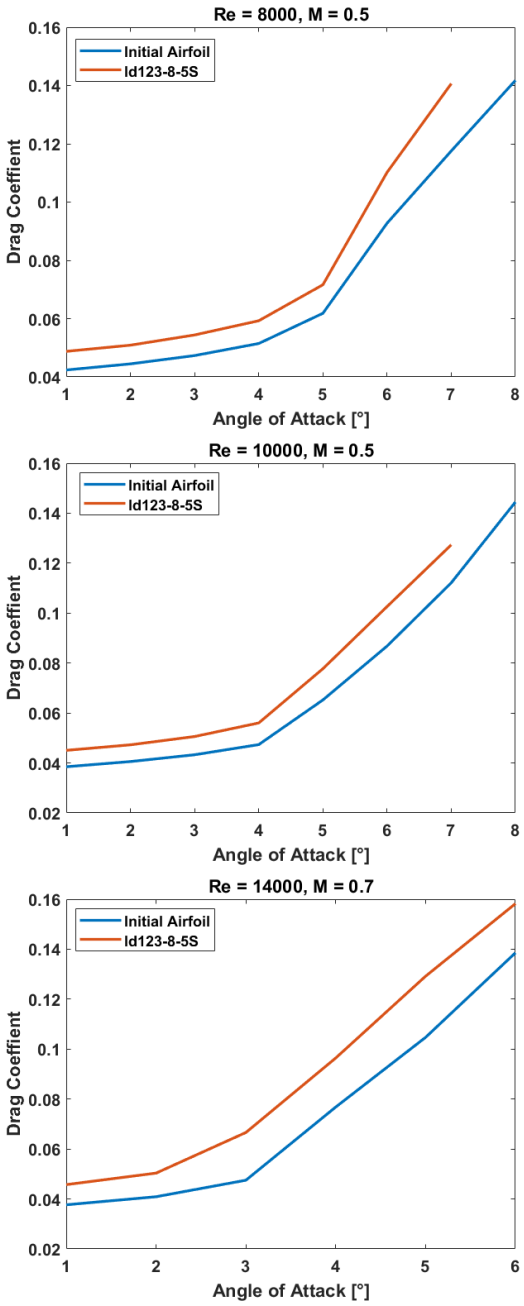

Figure 46: Averaged drag coefficient variations with angle of attack at different Reynolds and Mach numbers of ld123-8-5S compared to the initial airfoil

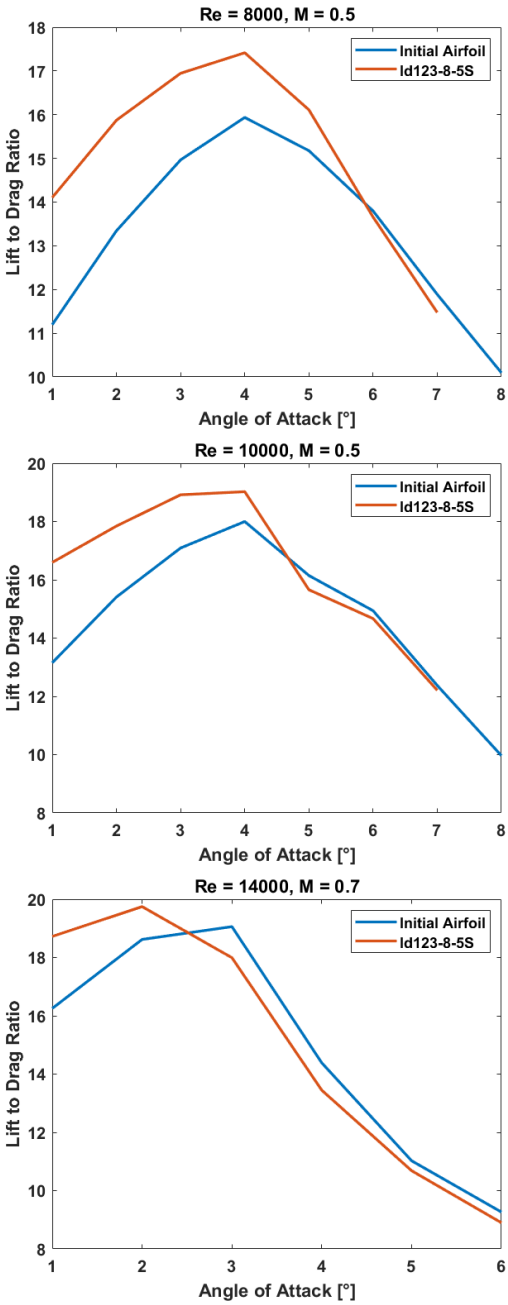

Figure 47: Averaged lift to drag ratio variations with angle of attack at different Reynolds and Mach numbers of ld123-8-5S compared to the initial airfoil

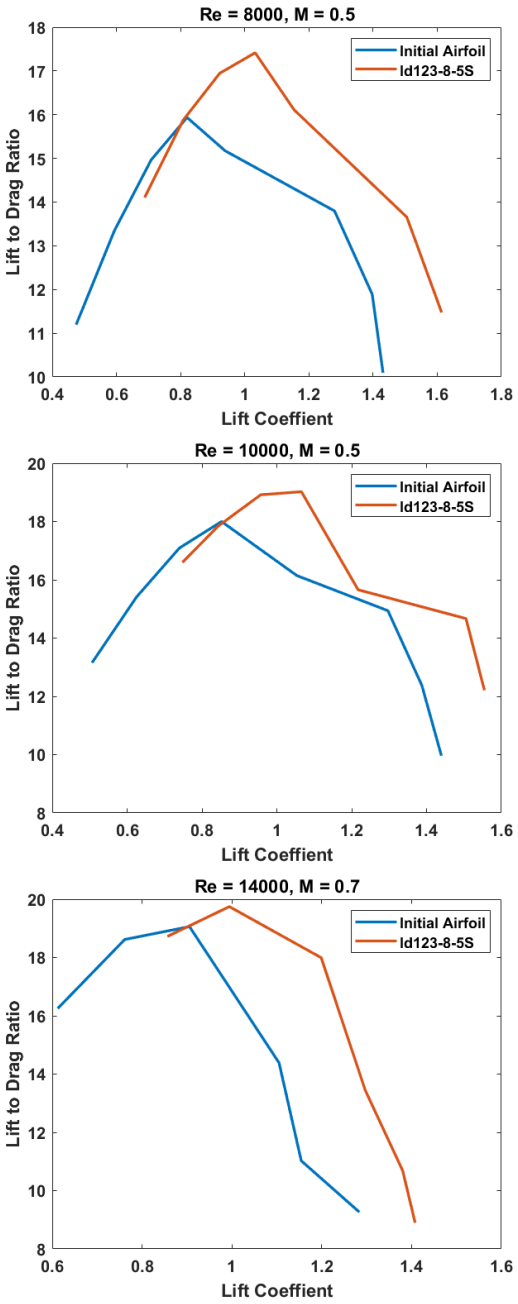

Figure 48: Averaged lift to drag ratio variations with lift coefficient at different Reynolds and Mach numbers of ld123-8-5S compared to the initial airfoil

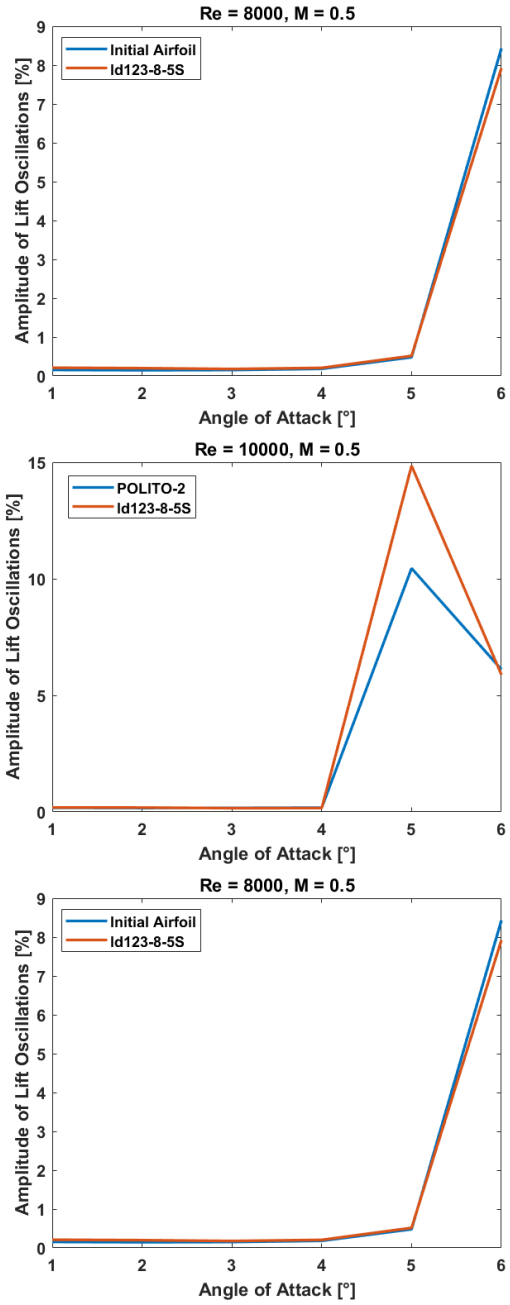

Figure 49: Lift coefficient oscillations from the mean value in percentage of the mean value at different Reynolds and Mach numbers of ld123-8-5S compared to the initial airfoil

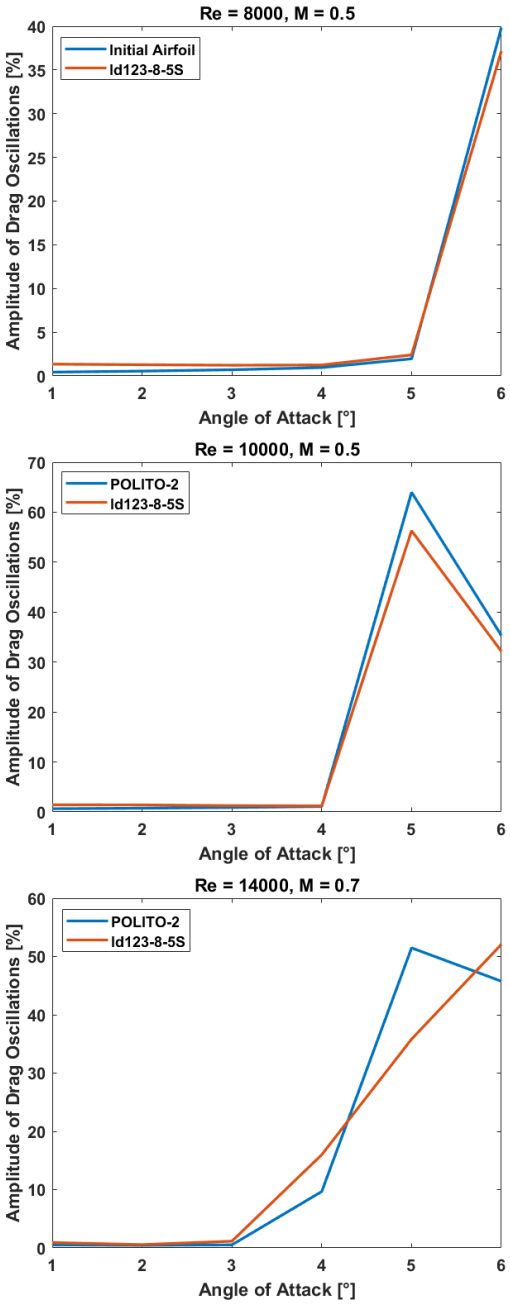

Figure 50: Drag coefficient oscillations from the mean value in percentage of the mean value at different Reynolds and Mach numbers of ld123-8-5S compared to the initial airfoil

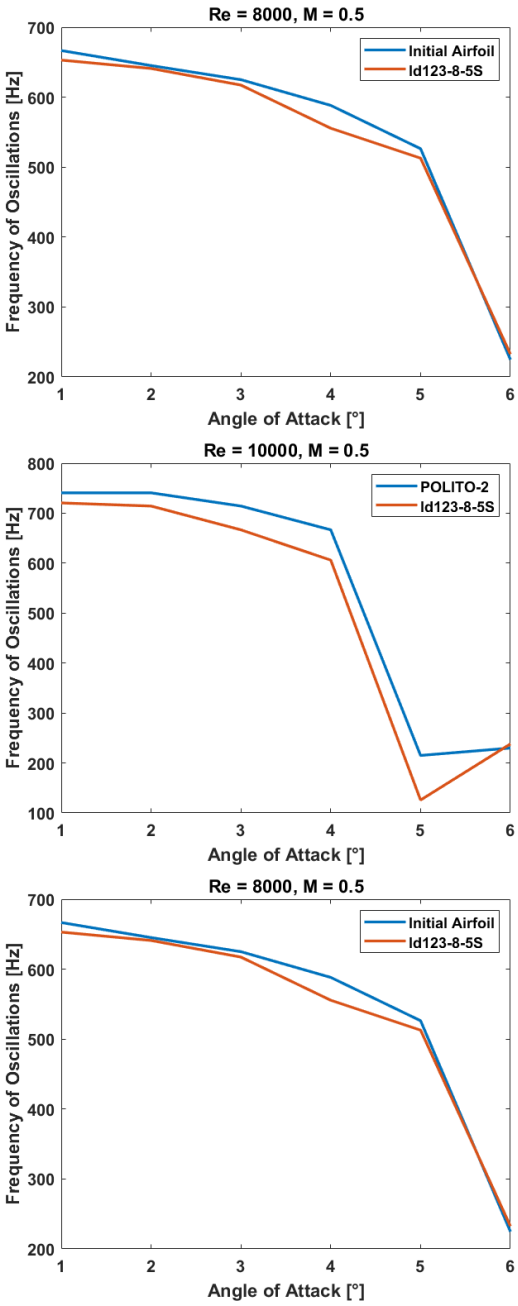

Figure 51: Frequency of oscillation at different Reynolds and Mach numbers of ld123-8-5S compared to the initial airfoil

From the $C_l - \alpha$ curve it can be seen that at Re = 10000, no laminar separation bubble is formed at 5°of angle of attack, with the slope remaining constant. This effect is due to the lower curvature of the airfoil, which produces a weaker pressure gradient, making the boundary layer less unstable and less likely to reattach. This also happens at Re = 14000.

The lift coefficient at maximum lift to drag ratio remains close to 0.8, thus, the flying conditions do not change, at equal aircraft weight, and the small increment of lift to drag ratio can be exploited.

7.2.2 Oscillations Behaviour

From the behaviour of the oscillations, it can be seen that the amplitude of the oscillations is less than that of the initial airfoil at all flow conditions. Furthermore, the lack of laminar separation bubble formation can be seen in terms of a lack of increase in the amplitude of the oscillations at 5°.

7.3 Airfoil 3

7.3.1 Averaged Performances

The third airfoil has a similar geometry to the first airfoil, with a pronounced curvature near the trailing edge. The unsteady averaged optimisation process has produced a flatter upper surface in the central part of the airfoil. For this reason, the reattachment of the separated flow to the upper surface is not possible due to the lack of pressure gradients. Therefore, the same effect occurs as in *cd234-8-5S*. Figure 63 compares the separated region on the upper surface of the initial airfoil and the two airfoils where this effect occurs. It can be seen that there is no reattachment of the separated flow, resulting in a thinner shear layer, which produces less pressure drag (verifiable in the $C_d - \alpha$ curve of the three airfoils).

In addition, due to the increased bottom loading, the lift coefficient of the maximum lift to drag ratio is shifted from 0.8 to 1, as in the first airfoil.

7.3.2 Oscillations Behaviour

The behaviour of the oscillations confirms what was said above about the laminar separation bubble. The amplitudes of the oscillations are weaker than those of the initial airfoil at high angles of attack for the second and third flow conditions, while for the first conditions the amplitudes are greater at all angles of attack, albeit by a small amount.

At Re = 10000, the drop in frequency caused by the formation of the bubble is eliminated, so that the frequency drops only when the flow separates at the leading edge at an angle of attack of 6°.

7.4 Airfoil 4

7.4.1 Averaged Performances

The not so pronounced curvature on the trailing edge with respect to the airfoil obtained in optimization 1 and 3 makes the lift coefficient of maximum lift to drag ratio of this airfoil close to that of the initial airfoil, with a slight increase.

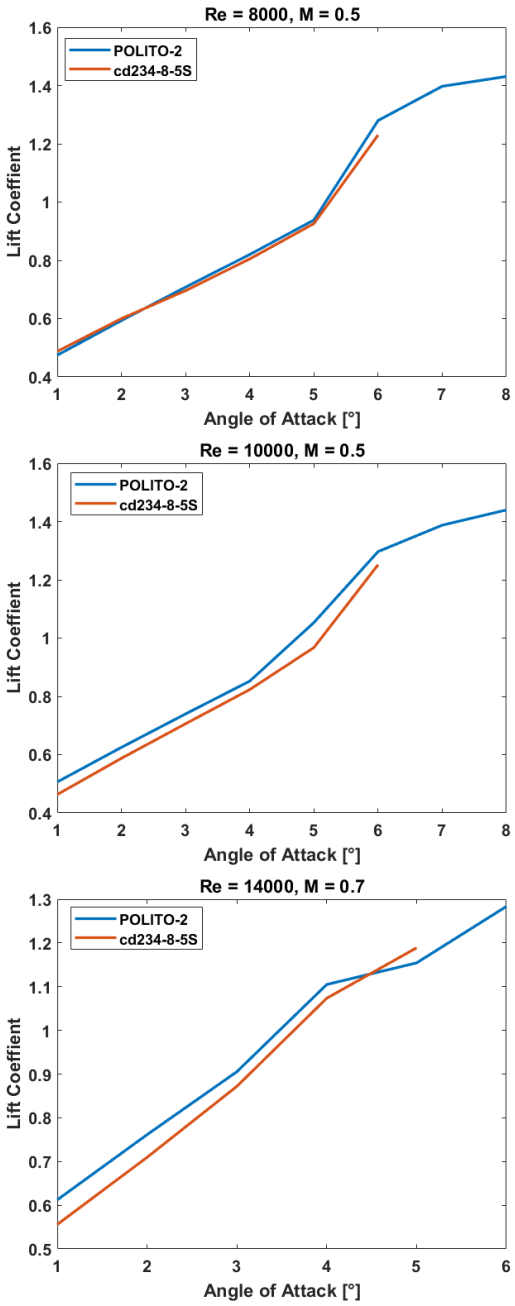

Figure 52: Averaged lift coefficient variations with angle of attack at different Reynolds and Mach numbers of cd234-8-5S compared to the initial airfoil

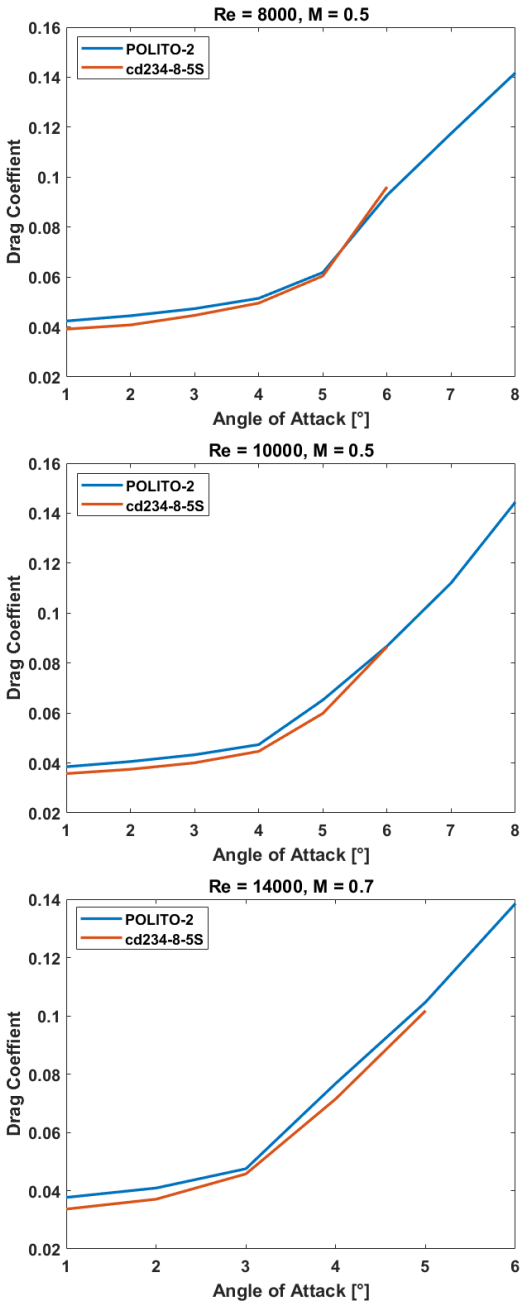

Figure 53: Averaged drag coefficient variations with angle of attack at different Reynolds and Mach numbers of cd234-8-5S compared to the initial airfoil

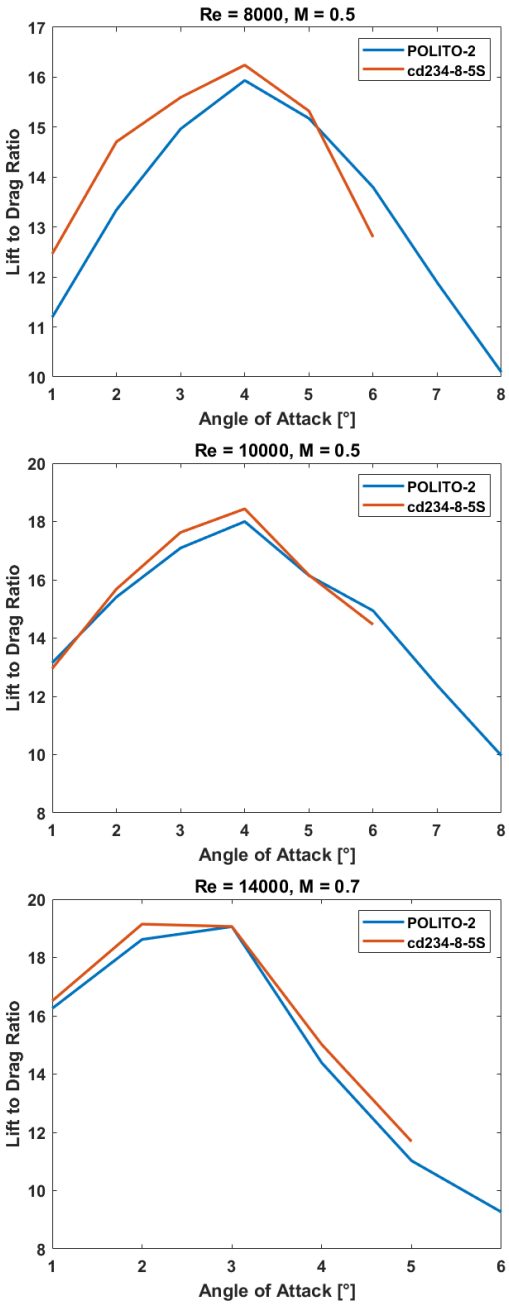

Figure 54: Averaged lift to drag ratio variations with angle of attack at different Reynolds and Mach numbers of cd234-8-5S compared to the initial airfoil

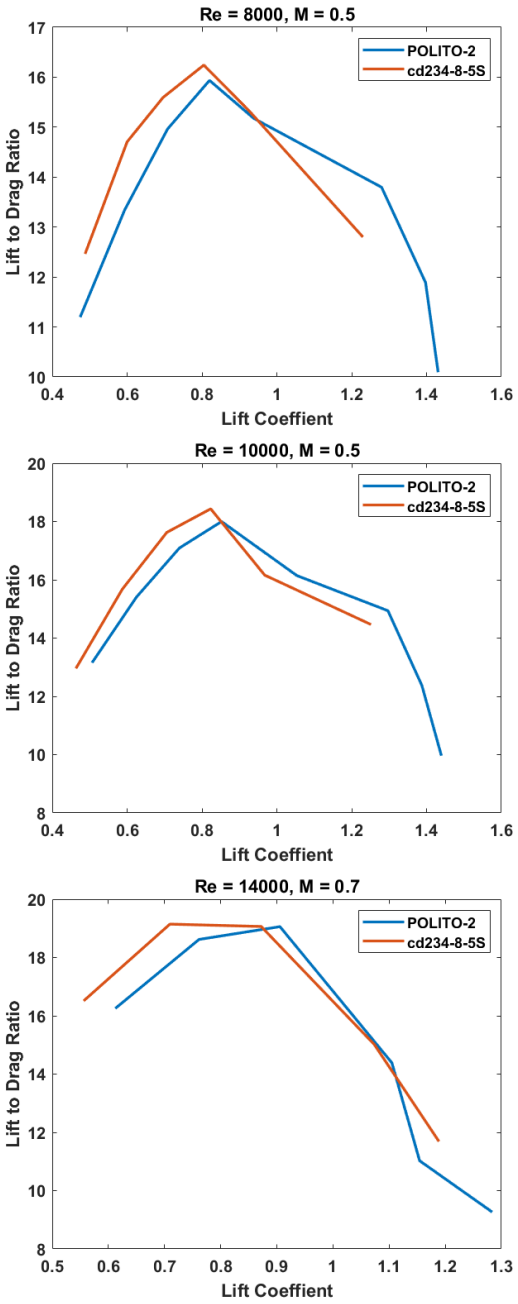

Figure 55: Averaged lift to drag ratio variations with lift coefficient at different Reynolds and Mach numbers of cd234-8-5S compared to the initial airfoil

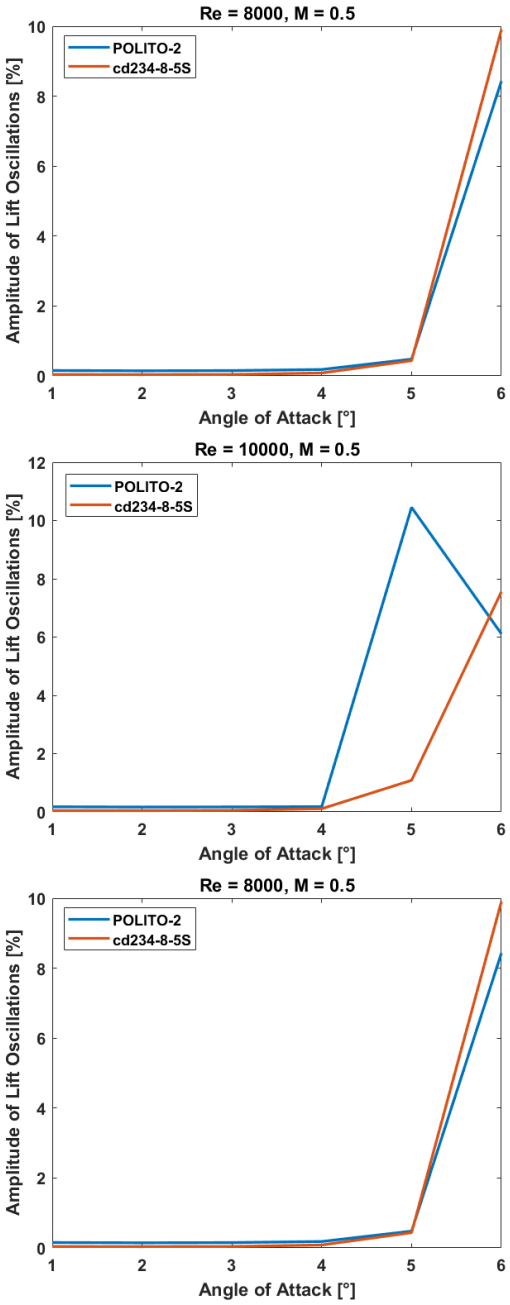

Figure 56: Lift coefficient oscillations from the mean value in percentage of the mean value at different Reynolds and Mach numbers of cd234-8-5S compared to the initial airfoil

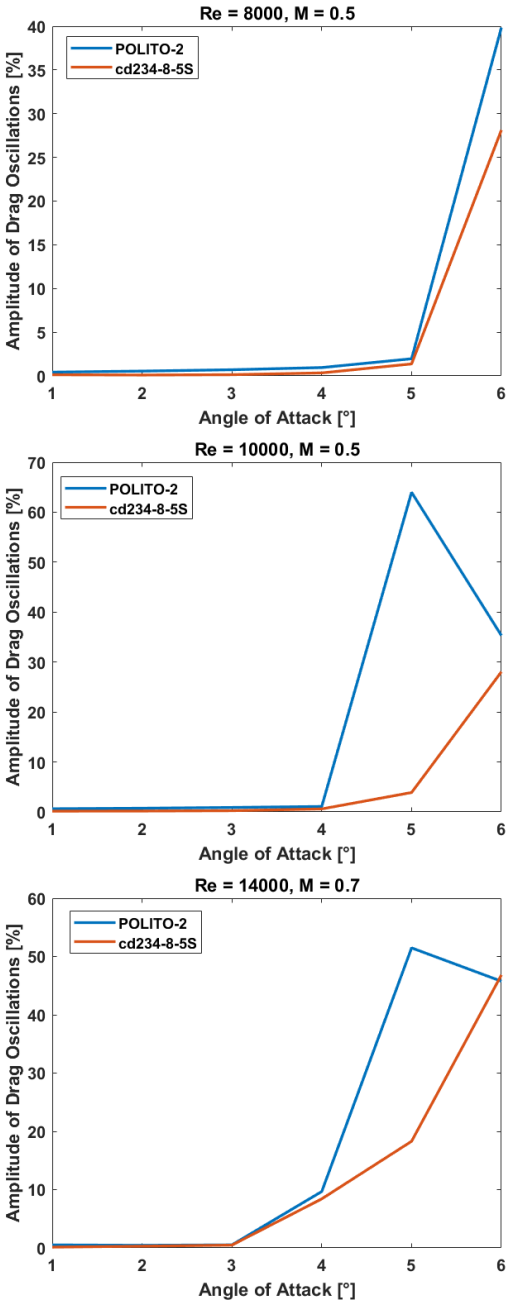

Figure 57: Drag coefficient oscillations from the mean value in percentage of the mean value at different Reynolds and Mach numbers of cd234-8-5S compared to the initial airfoil

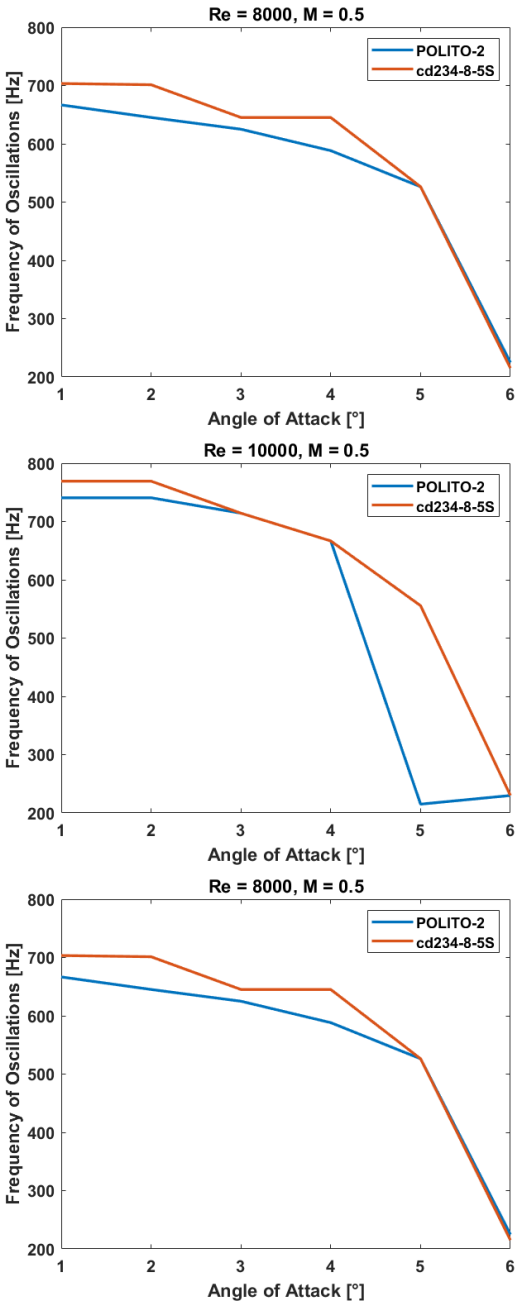

Figure 58: Frequency of oscillation at different Reynolds and Mach numbers of cd234-8-5S compared to the initial airfoil

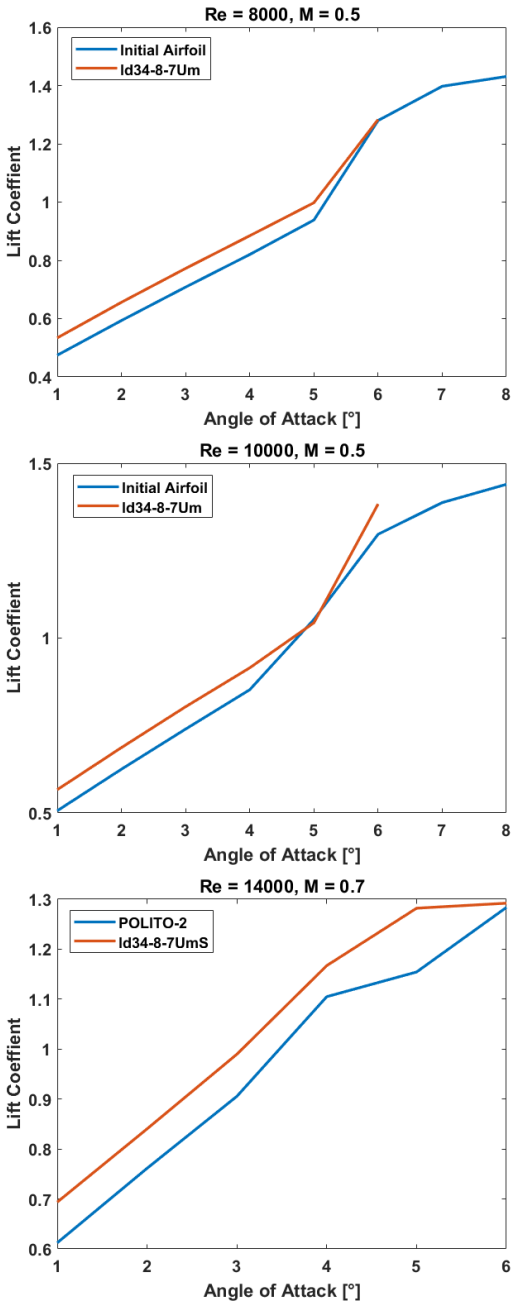

Figure 59: Averaged lift coefficient variations with angle of attack at different Reynolds and Mach numbers of ld34-8-7Um compared to the initial airfoil

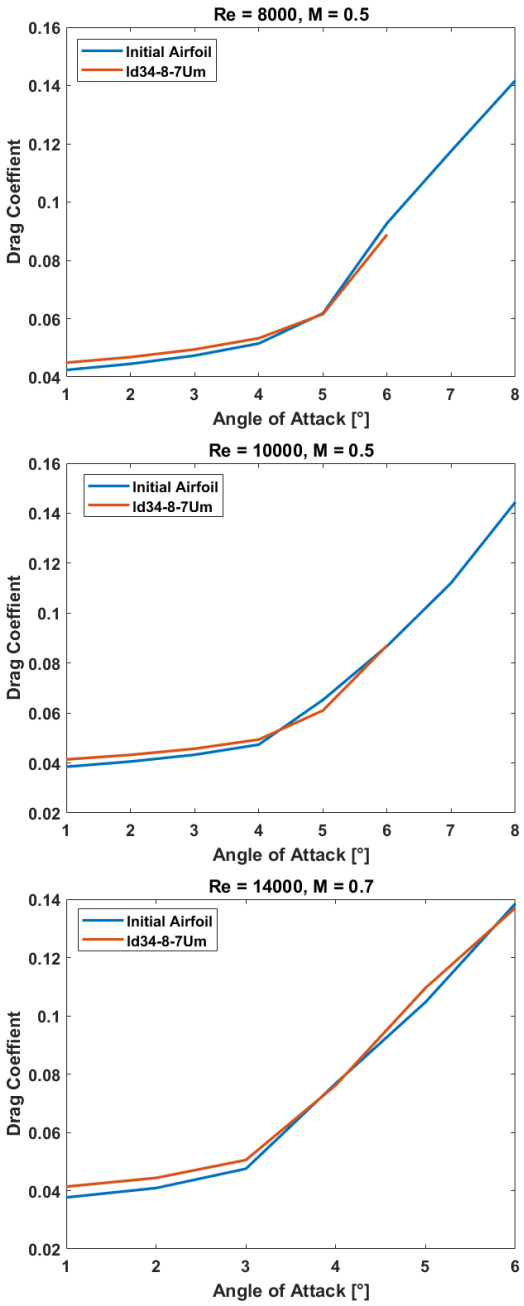

Figure 60: Averaged drag coefficient variations with angle of attack at different Reynolds and Mach numbers of ld34-8-7Um compared to the initial airfoil

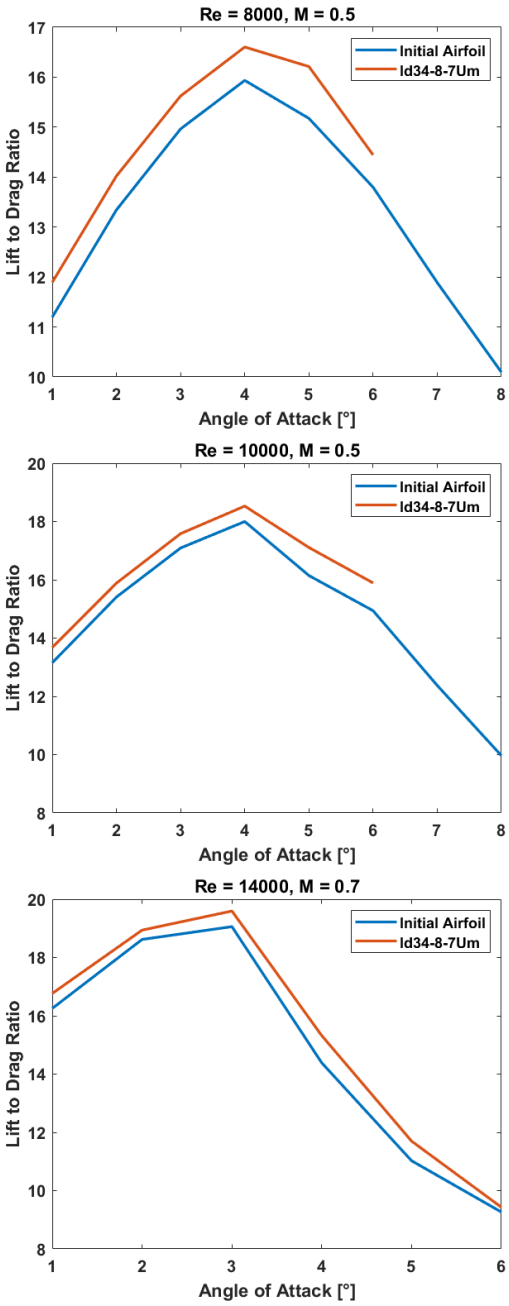

Figure 61: Averaged lift to drag ratio variations with angle of attack at different Reynolds and Mach numbers of ld34-8-7Um compared to the initial airfoil

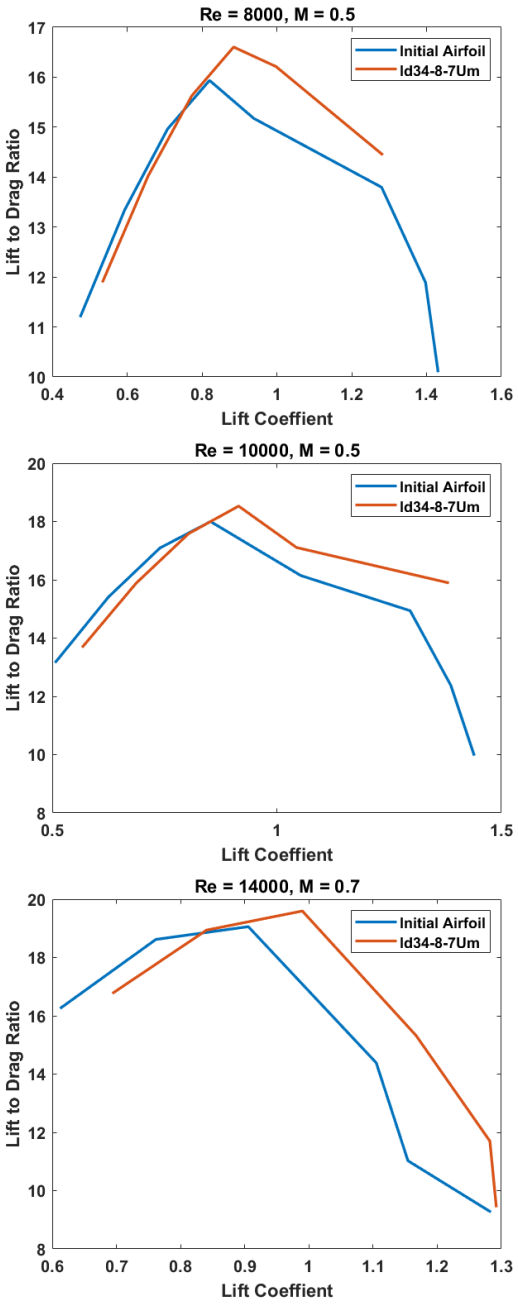

Figure 62: Averaged lift to drag ratio variations with lift coefficient at different Reynolds and Mach numbers of ld34-8-7Um compared to the initial airfoil

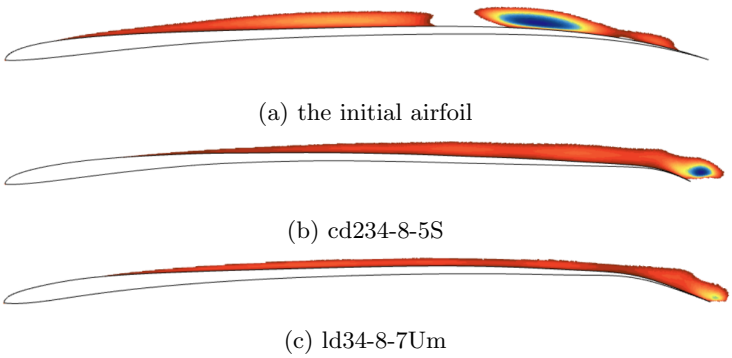

(a) the initial airfoil

(b) cd234-8-5S

(c) ld34-8-7Um

Figure 63: Comparison of the separated shear layer on the airfoil, visualised by the negative velocity field in the chord direction, on the initial airfoil, cd234-8-5S and ld34-8-7Um at Re = 10000, M = 0.5

The interesting feature is that performances are enhanced, although the flap is not so important, highlighting the benefits of the leading edge flap.

Another important aspect is the fact that at 5 degrees the airfoil, at both Re = 8000 and Re = 10000, shows drastically higher values of lift to drag ratio, with respects to the initial airfoil, obtaining a wider range of usability. This occurs because at this angle the airfoil has a smaller laminar separation bubble at Re = 10000, and is not separated yet at Re = 10000.

7.4.2 Oscillations' Behaviour

The behaviour of the oscillations highlights features already found in the other airfoils analysed, with a decreasing frequency and increasing amplitudes with angle of attack. Overall, this airfoil has smaller amplitudes of oscillations at all angles of attack and conditions.

7.5 Airfoil 5

7.5.1 Averaged Performances

This airfoil has changed in the most visible way, presenting leading and trailing edge flaps

The geometry of the leading edge is designed to form a short laminar separation bubble, which reduces the viscous drag while increasing slightly the pressure drag.

To form a short bubble, the reattachment point must be close, therefore a pressure ramp (its effects are explained in [1]) is obtained by the curvature after the leading edge. On the central part of the airfoil, when the flow is close to the optimum angle of attack, a second laminar separation bubble is formed, further reducing the viscous drag.

These effects are visible at the flow conditions where the airfoil was optimised, i.e. Re = 14000 and M = 0.7. Here the reduction in viscous drag is accompanied by a small increase in pressure drag due to the short length of the bubble.

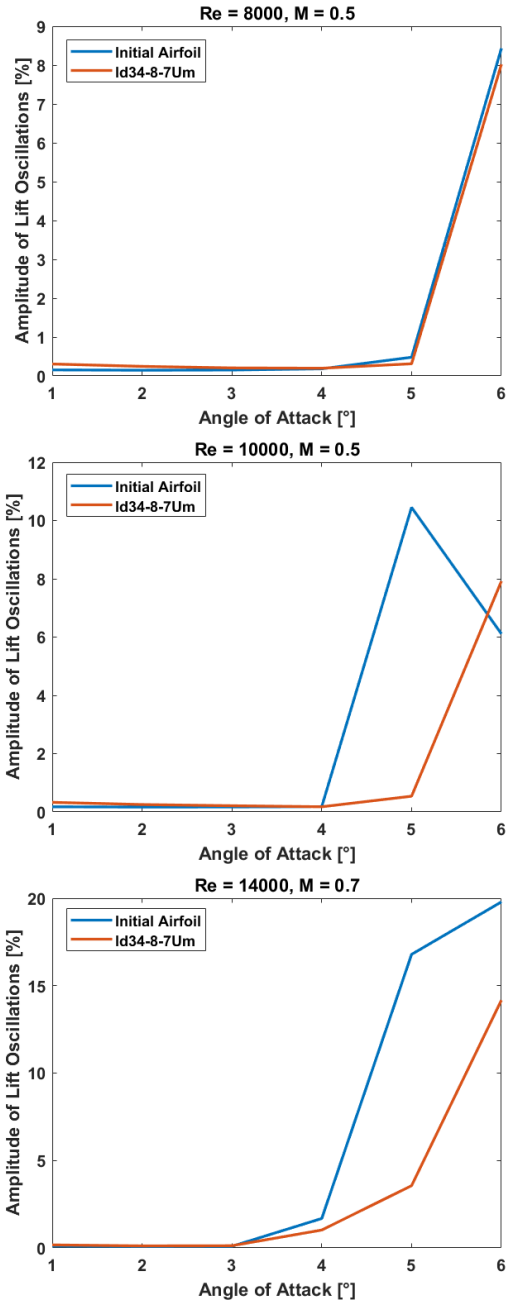

Figure 64: Lift coefficient oscillations from the mean value in percentage of the mean value at different Reynolds and Mach numbers of ld34-8-7Um compared to the initial airfoil

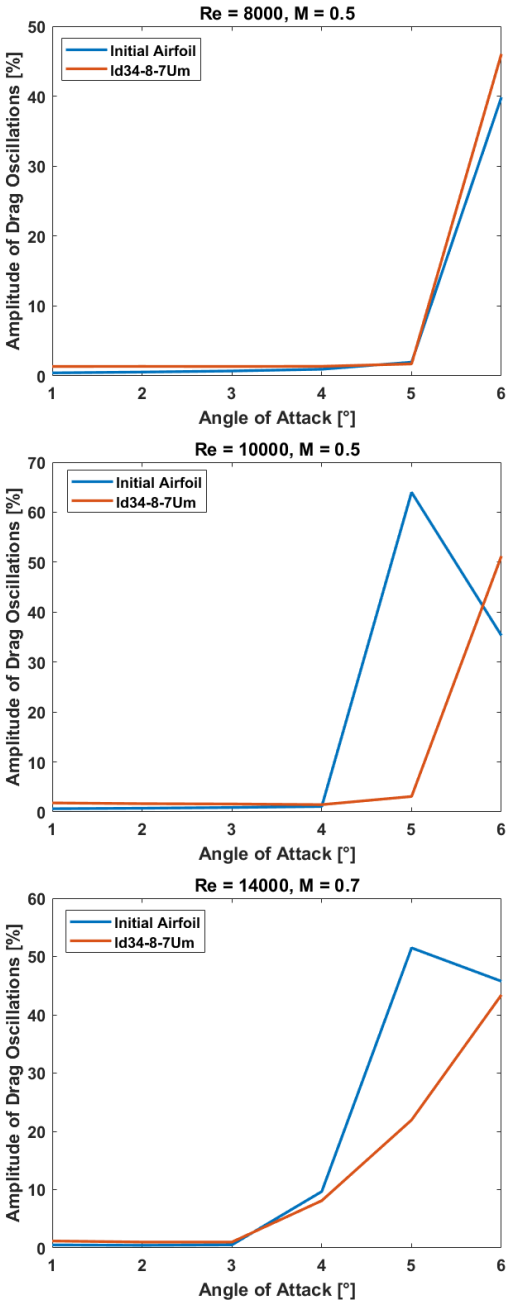

Figure 65: Drag coefficient oscillations from the mean value in percentage of the mean value at different Reynolds and Mach numbers of ld34-8-7Um compared to the initial airfoil

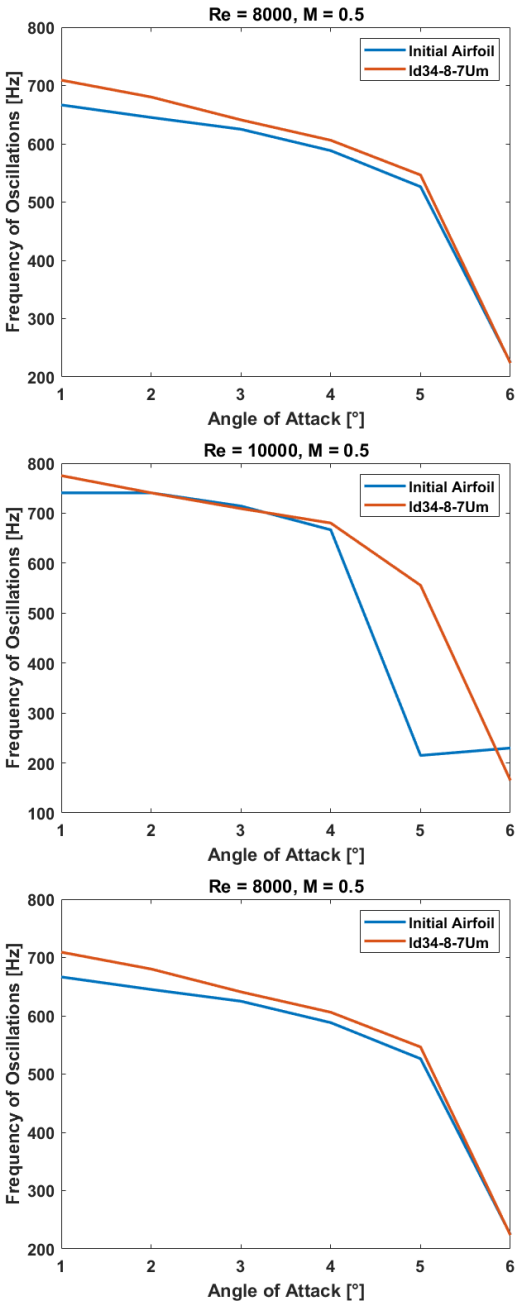

Figure 66: Frequency of oscillation at different Reynolds and Mach numbers of ld34-8-7Um compared to the initial airfoil

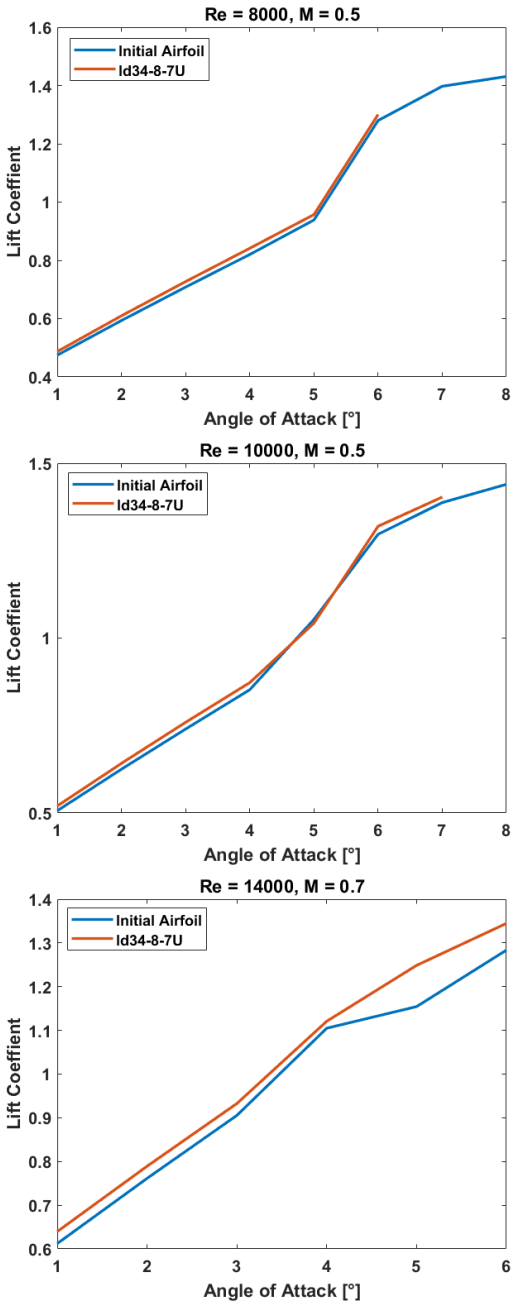

Figure 67: Averaged lift coefficient variations with angle of attack at different Reynolds and Mach numbers of ld34-8-7U compared to the initial airfoil

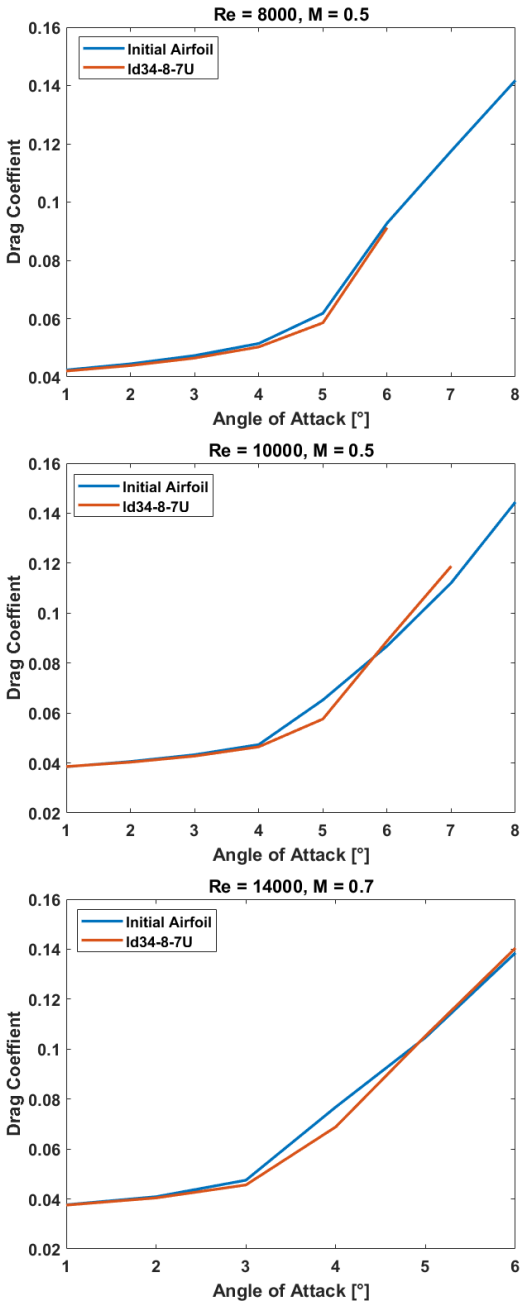

Figure 68: Averaged drag coefficient variations with angle of attack at different Reynolds and Mach numbers of ld34-8-7U compared to the initial airfoil

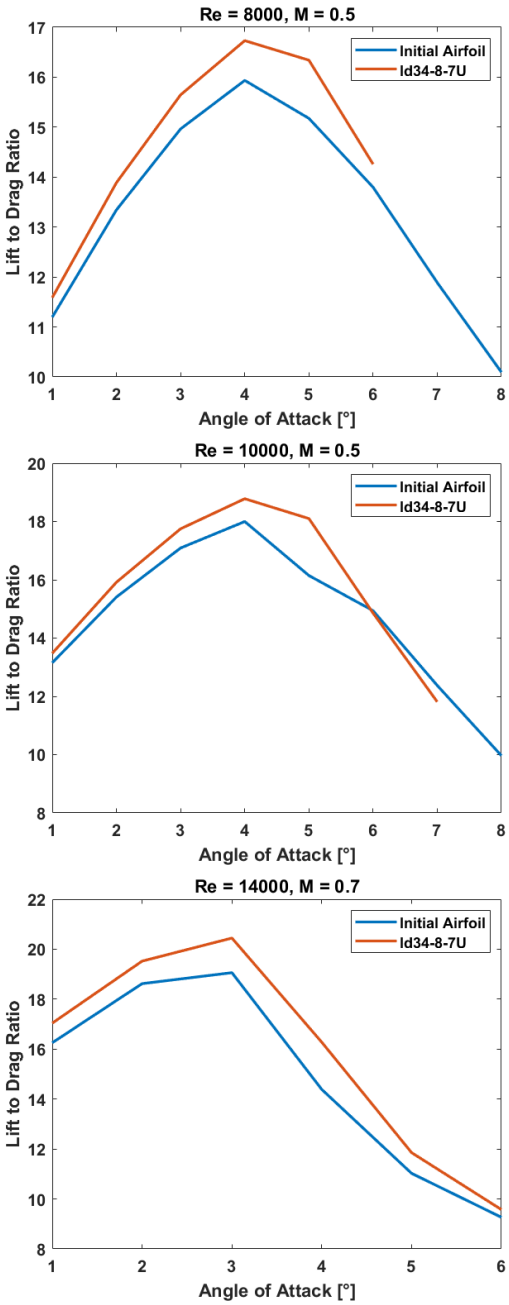

Figure 69: Averaged lift to drag ratio variations with angle of attack at different Reynolds and Mach numbers of ld34-8-7U compared to the initial airfoil

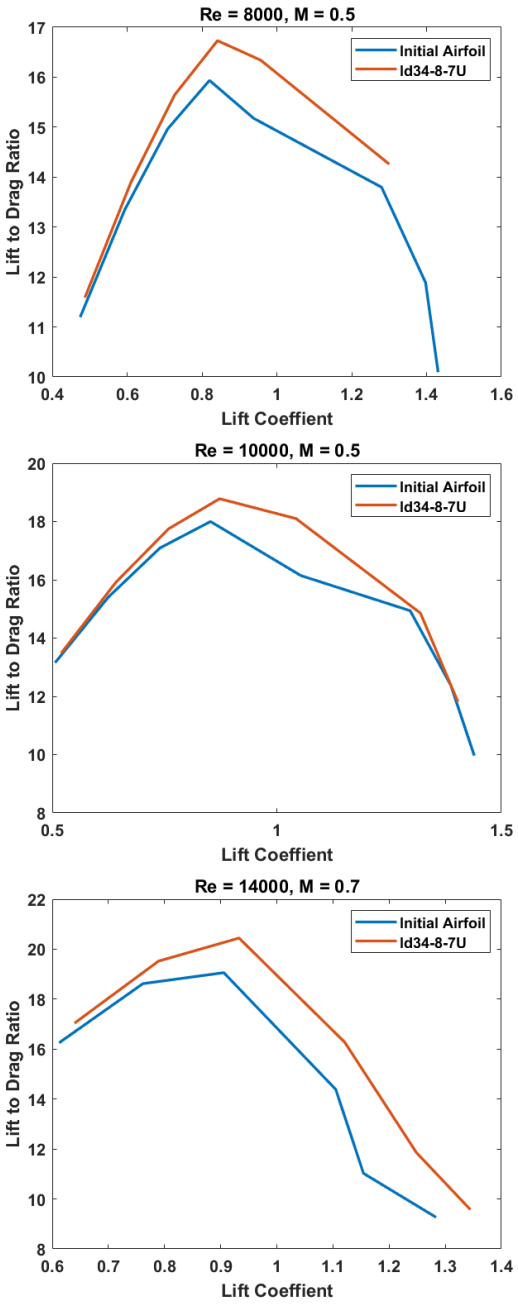

Figure 70: Averaged lift to drag ratio variations with lift coefficient at different Reynolds and Mach numbers of ld34-8-7U compared to the initial airfoil

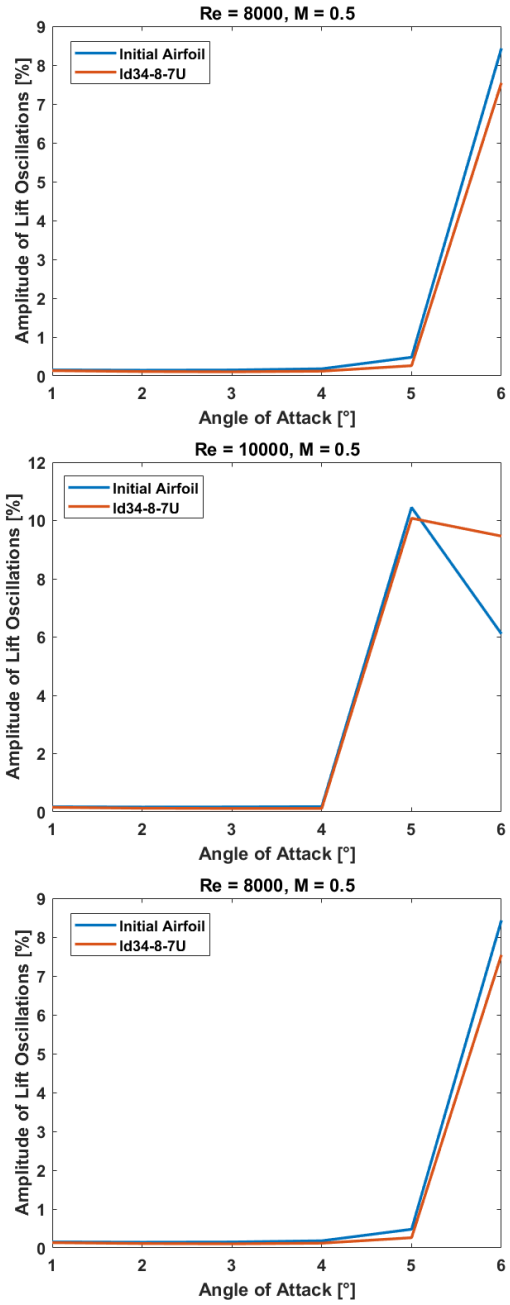

Figure 71: Lift coefficient oscillations from the mean value in percentage of the mean value at different Reynolds and Mach numbers of ld34-8-7U compared to the initial airfoil

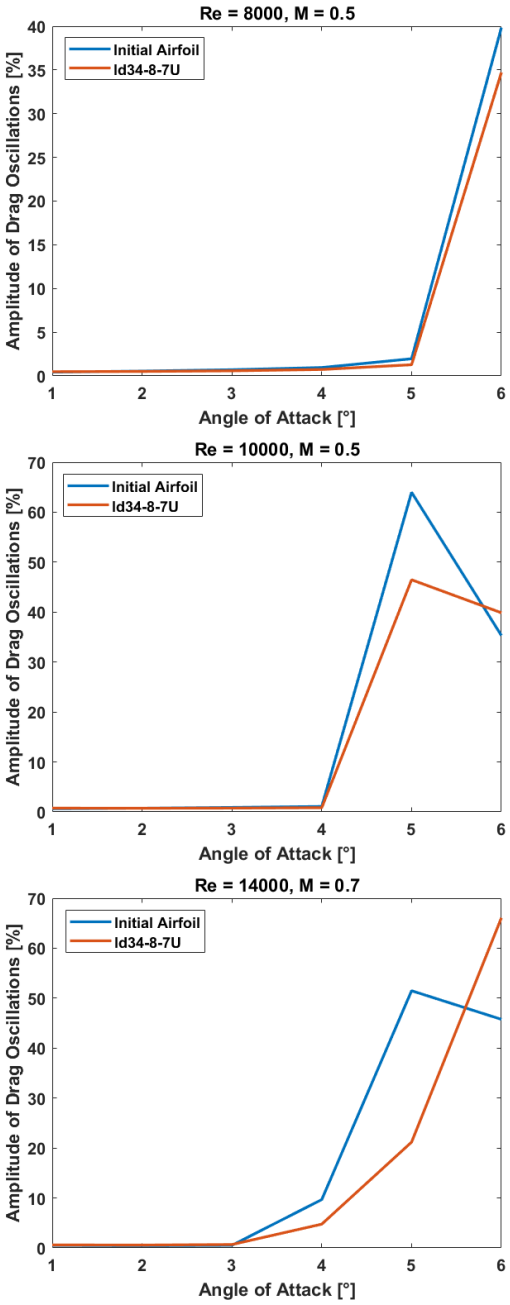

Figure 72: Drag coefficient oscillations from the mean value in percentage of the mean value at different Reynolds and Mach numbers of ld34-8-7U compared to the initial airfoil

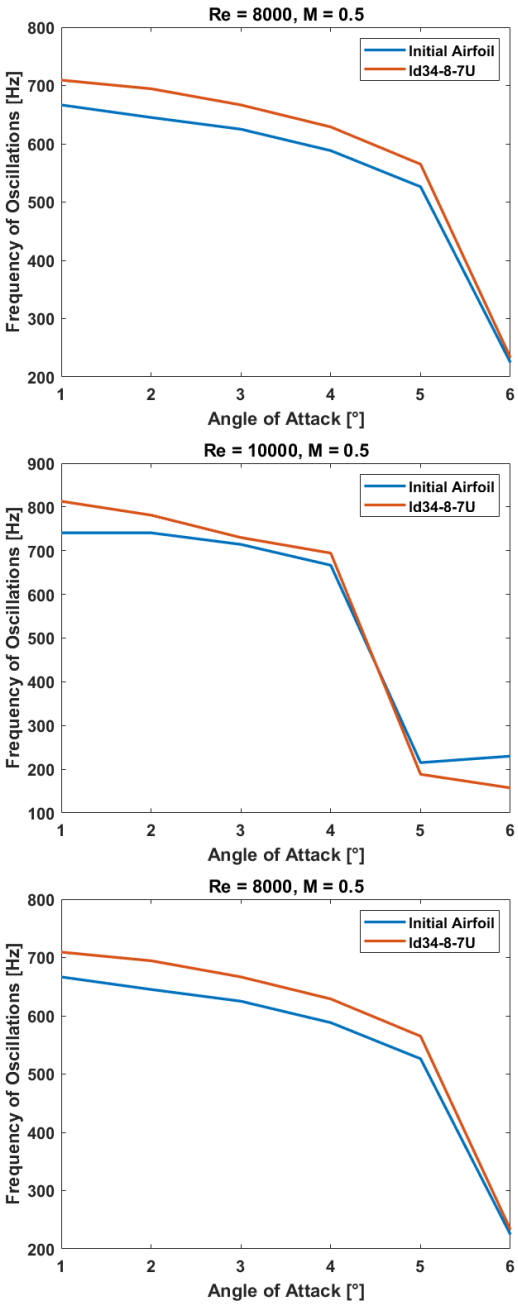

Figure 73: Frequency of oscillation at different Reynolds and Mach numbers of ld34-8-7U compared to the initial airfoil

At lower Reynolds numbers, the pressure ramp on the upper surface is not strong enough to produce a reattachment of the flow, resulting in a long bubble, that increases the pressure drag, degrading the performances.

Difference bubble over the airfoil are shown in figure 74 and 75.

Because of these effects, at Re = 14000 the airfoil has a high lift to drag ratio over a small range of angles of attack, i.e. the range where the laminar separation bubble is short.

At Re = 10000, the lift to drag ratio is maximum at 4°, but as can be seen from the oscillations plots, at this angle the flow is already separated near the leading edge, producing high amplitude oscillations.

At Re = 8000, the maximum lift to drag ratio of the airfoil is reached at an angle of attack of 4°, where a short laminar separation bubble is formed on both the leading edge flap and the central part of the airfoil.

The lift coefficient at the maximum lift to drag ratio is slightly increased compared to the original airfoil, but what makes this airfoil interesting is the fact that at Re = 14000 the lift to drag ratio is close to the maximum in a range of lift coefficients 0.2 wide, with a probable maximum above 20 at lift coefficients close to 0.85.

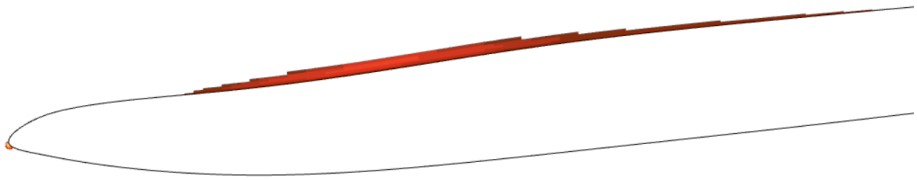

(a) Detail of the short bubble near the leading edge

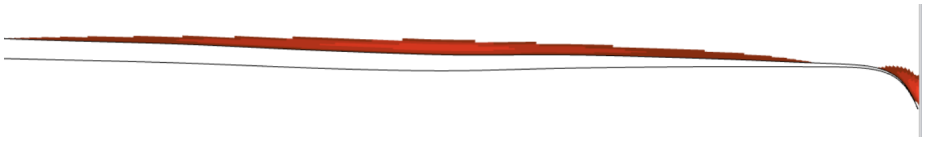

(b) Detail of the bubble on the central part of the airfoil

Figure 74: Laminar separation bubbles formed at Re = 14000 and M = 0.7 over the upper surface of ld34-14-7U

Figure 75: Laminar separation bubbles formed at Re = 10000 and M = 0.5 over the upper surface of ld34-14-7U

7.5.2 Oscillations Behaviour

The oscillations' behaviour of the airfoil highlights an important aspect of the laminar separation bubble: although a short separation bubble is present at $\alpha = 3°$at Re = 14000, oscillations amplitudes are small, while at $\alpha = 4°$at Re =

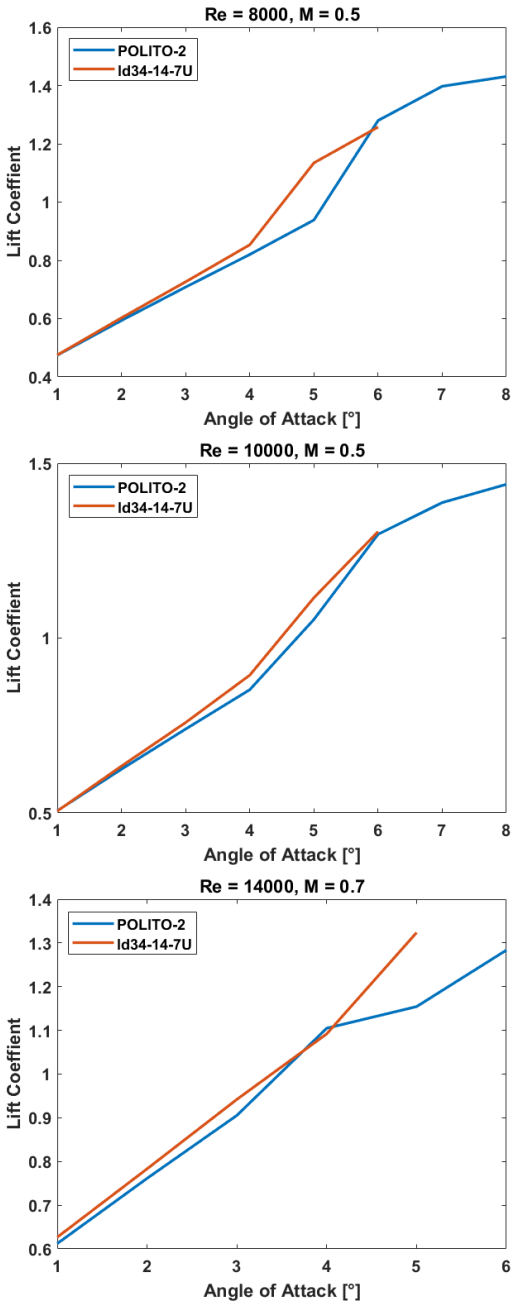

Figure 76: Averaged lift coefficient variations with angle of attack at different Reynolds and Mach numbers of ld34-14-7U compared to the initial airfoil

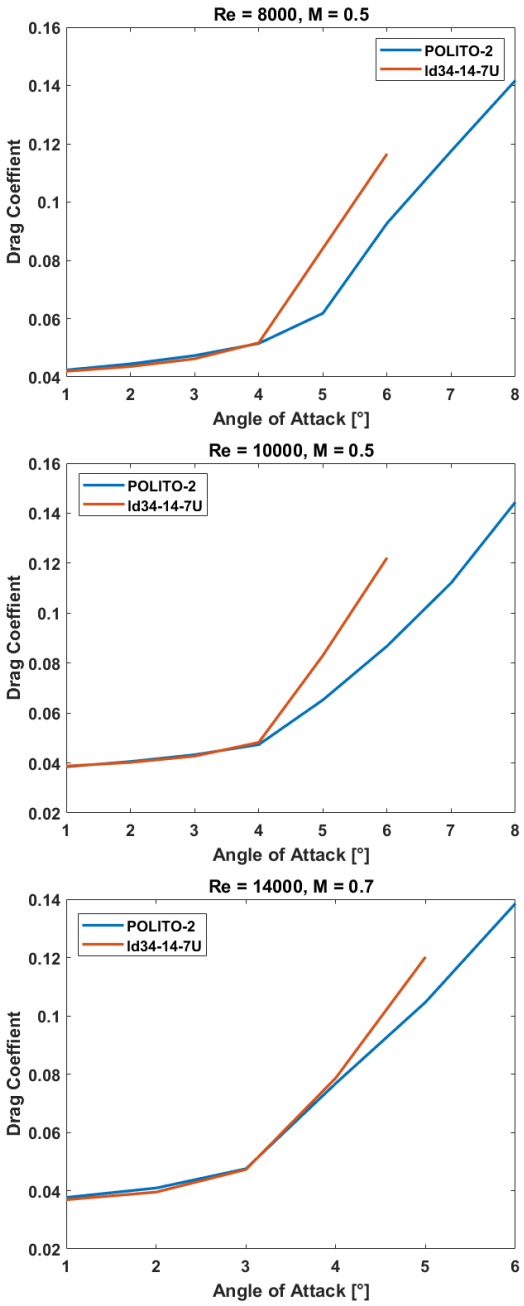

Figure 77: Averaged drag coefficient variations with angle of attack at different Reynolds and Mach numbers of ld34-14-7U compared to the initial airfoil

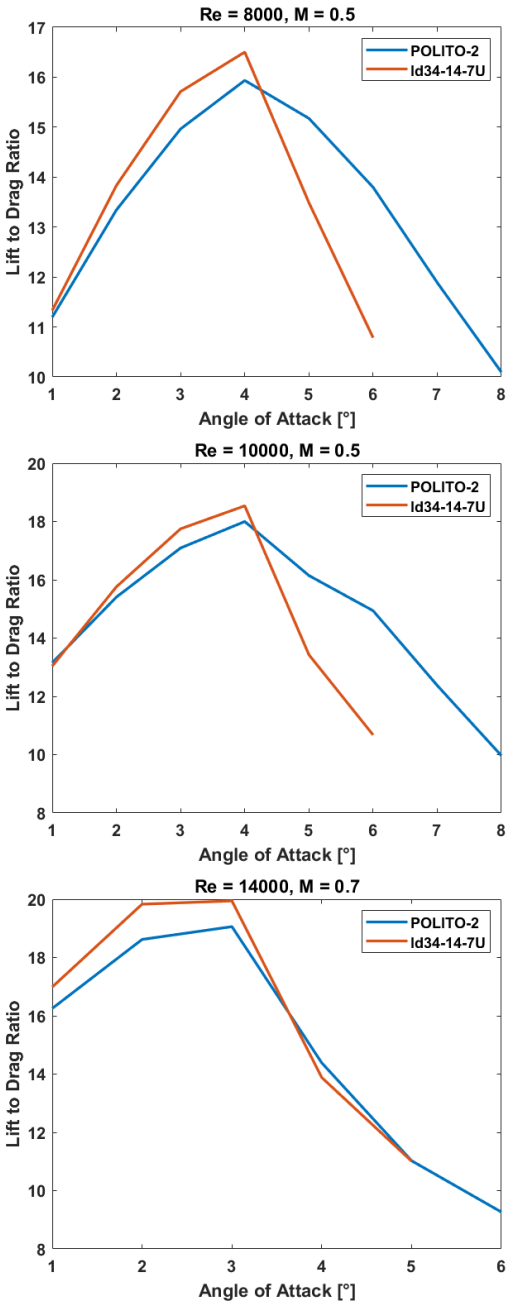

Figure 78: Averaged lift to drag ratio variations with angle of attack at different Reynolds and Mach numbers of ld34-14-7U compared to the initial airfoil

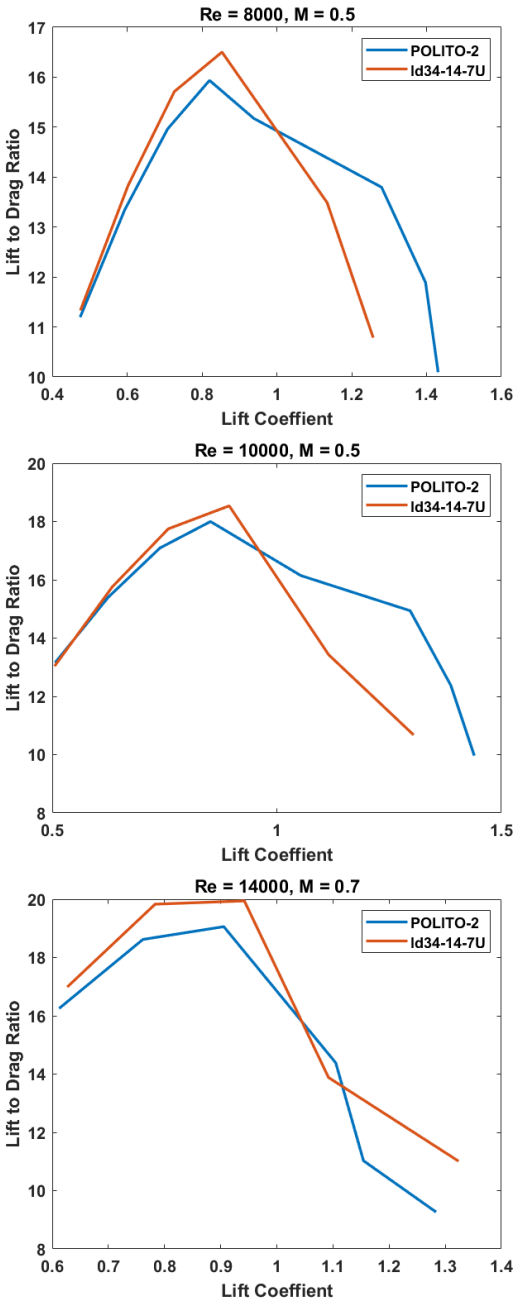

Figure 79: Averaged lift to drag ratio variations with lift coefficient at different Reynolds and Mach numbers of ld34-14-7U compared to the initial airfoil

10000, where a long laminar separation bubble is formed, oscillations amplitudes rise.

Therefore, a short laminar separation bubble is ideal for the performance of an airfoil at low Reynolds number, since:

- viscous drag drops because in a separated flow the wall shear stress is negative;
- pressure drag is only slightly increased because the height of the separation bubble is relatively small;
- oscillations amplitude are not influenced by the short laminar separation bubble, thus they remain contained

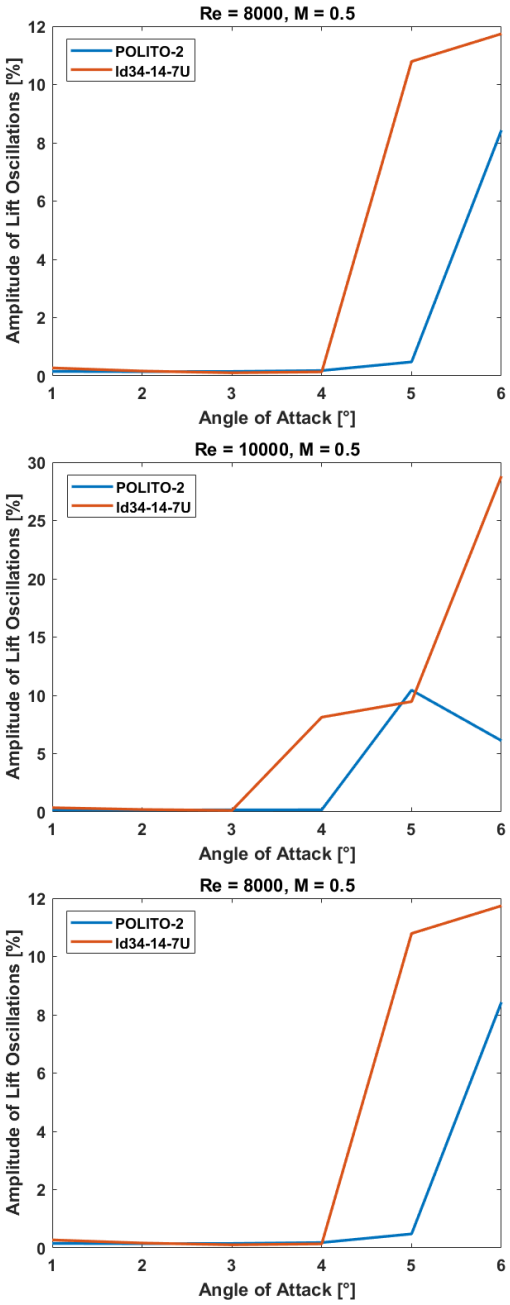

Figure 80: Lift coefficient oscillations from the mean value in percentage of the mean value at different Reynolds and Mach numbers of ld34-14-7U compared to the initial airfoil

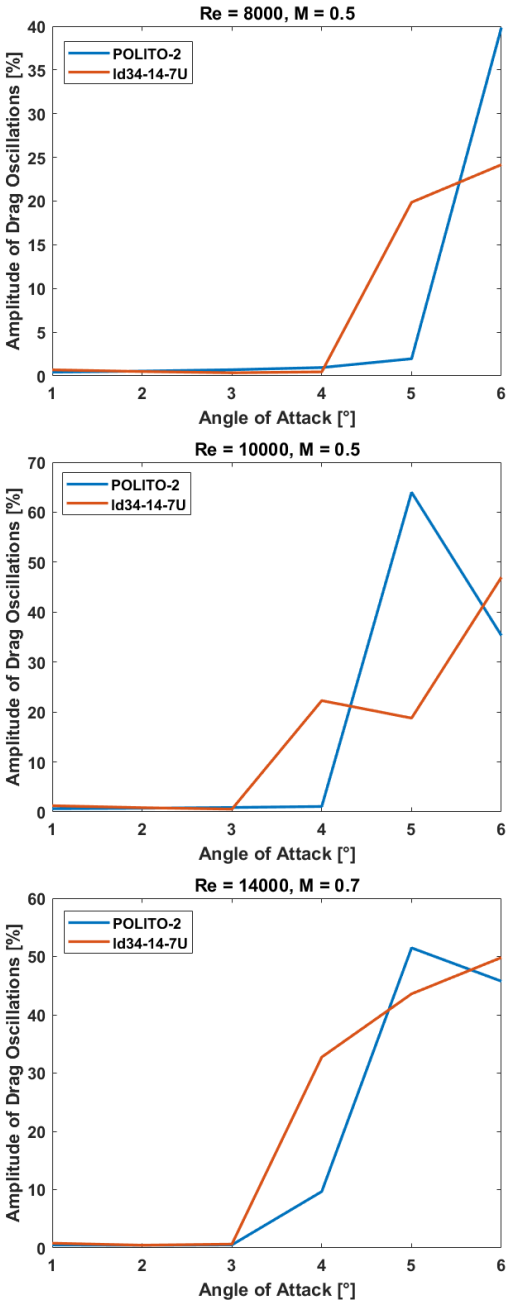

Figure 81: Drag coefficient oscillations from the mean value in percentage of the mean value at different Reynolds and Mach numbers of ld34-14-7U compared to the initial airfoil

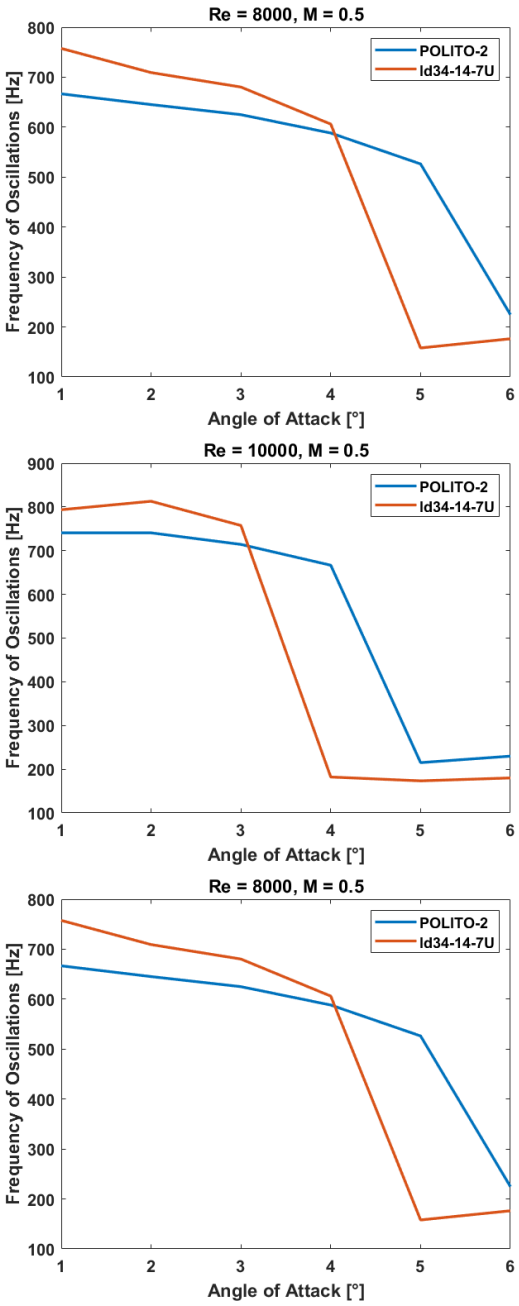

Figure 82: Frequency of oscillation at different Reynolds and Mach numbers of ld34-14-7U compared to the initial airfoil

7.6 Summary of Performance

This part summarizes performance of all the airfoil in terms of maximum lift to drag ratio, percentage of increment of lift to drag ratio from the initial airfoil, averaged lift coefficients, lift oscillations and drag oscillations at the condition of lift to drag ratio of each airfoil.

A comparison between these conditions can be made, but the fact that the CFD analysis is done at these angles of attack needs to be taken in considerations. In fact, if an airfoil has, for example, a maximum lift to drag ratio at an angle of attack of 3.5 degrees, the maximum lift to drag ratio that comes from the CFD analysis made at 3 or 4 degrees is less than the actual maximum. Thus, there are airfoils with maximum value of lift to drag ratio close to an even angle of attack and airfoil that don't. For the latter, the maximum is higher than that of the table.

In general, if the lift to drag ratio with angle of attack curve of an airfoil has a sort of plateau over two angles of attack, probably its maximum is contained between these angles. This is evident in figure 78.

Performances of the airfoils are shown in table 4, 5 and 6. The most improved airfoil for the first and second flow conditions (respectively Re = 8000, M = 0.5 and Re = 10000, M = 0.5) is the ld123-8-5S, with the ld34-8-7U that has slightly less but comparable values.

For the paper aimed condition, at Re = 14000 and M = 0.7, the most improved airfoils are the ld34-14-7U and ld34-8-7U. The former has a smaller maximum, but, as described above, the true maximum, that is probably at 2.5°, may be higher.

Airfoil	1	2	3	4	5
* Max C_l/C_d	17.416	16.242	16.604	16.732	16.503
Δ% from the initial airfoil	9.29%	1.92%	4.19%	4.99%	3.56%
C_l at *	1.0324	0.8049	0.8845	0.8414	0.8534
$C_{l_{osc}}$ at * %	0.2067%	0.0836%	0.1978%	0.1224%	0.1392%
$C_{d_{osc}}$ at * %	1.2493%	0.3436%	1.3700%	0.7366%	0.4628%

Table 4: Summary of performance of all the airfoil at their respective maximum at Re = 8000, M = 0.5

Airfoil	1	2	3	4	5
* Max C_l/C_d	19.023	18.435	18.530	18.782	18.538
Δ% from the initial airfoil	5.68%	2.42%	2.94%	4.34%	2.99%
C_l at *	1.0658	0.8233	0.8939	0.8726	0.9149
$C_{l_{osc}}$ at *%	0.1649%	0.1092%	0.1767%	0.1191%	8.1263%
$C_{d_{osc}}$ at *	1.2124%	0.6008%	1.4589%	0.8448%	22.2791%

Table 5: Summary of performance of all the airfoil at their respective maximum at Re = 10000, M = 0.5

Airfoil	1	2	3	4	5
* Max C_l/C_d	19.747	19.146	19.595	20.445	19.943
Δ% from the initial airfoil	3.60%	0.45%	2.81%	7.27%	4.63%
C_l at *	0.9943	0.7096	0.9898	0.9327	0.9421
$C_{l_{osc}}$ at *	0.0809%	0.1136%	0.1259%	0.0759%	0.1217%
$C_{d_{osc}}$ at *	0.5626%	0.3014%	1.0069%	0.6749%	0.6487%

Table 6: Summary of performance of all the airfoil at their respective maximum at Re = 14000, M = 0.7

In the end, airfoils lift to drag ratio at the three conditions are compared in figure 83, 84 and 85.

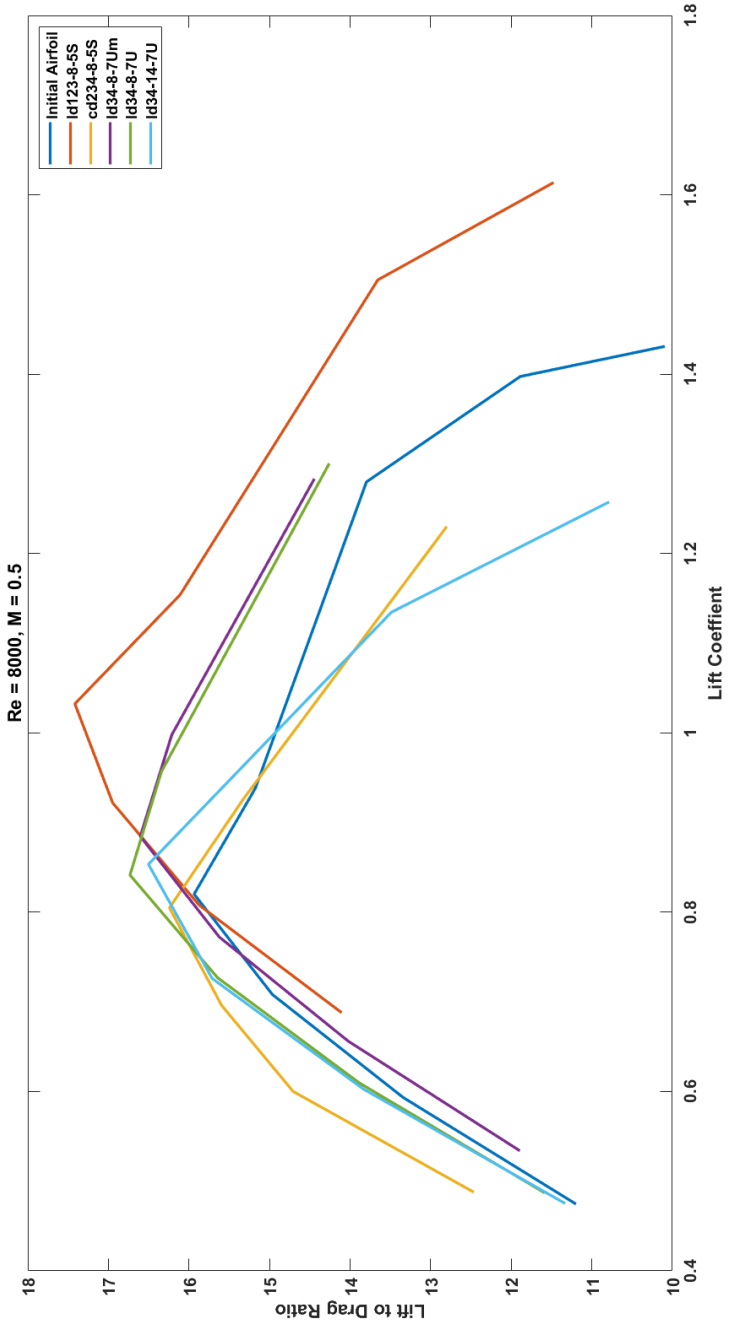

Figure 83: Comparison of lift to drag ratio variation with lift coefficients of all the airfoils present in the paper at Re = 8000 and M = 0.5

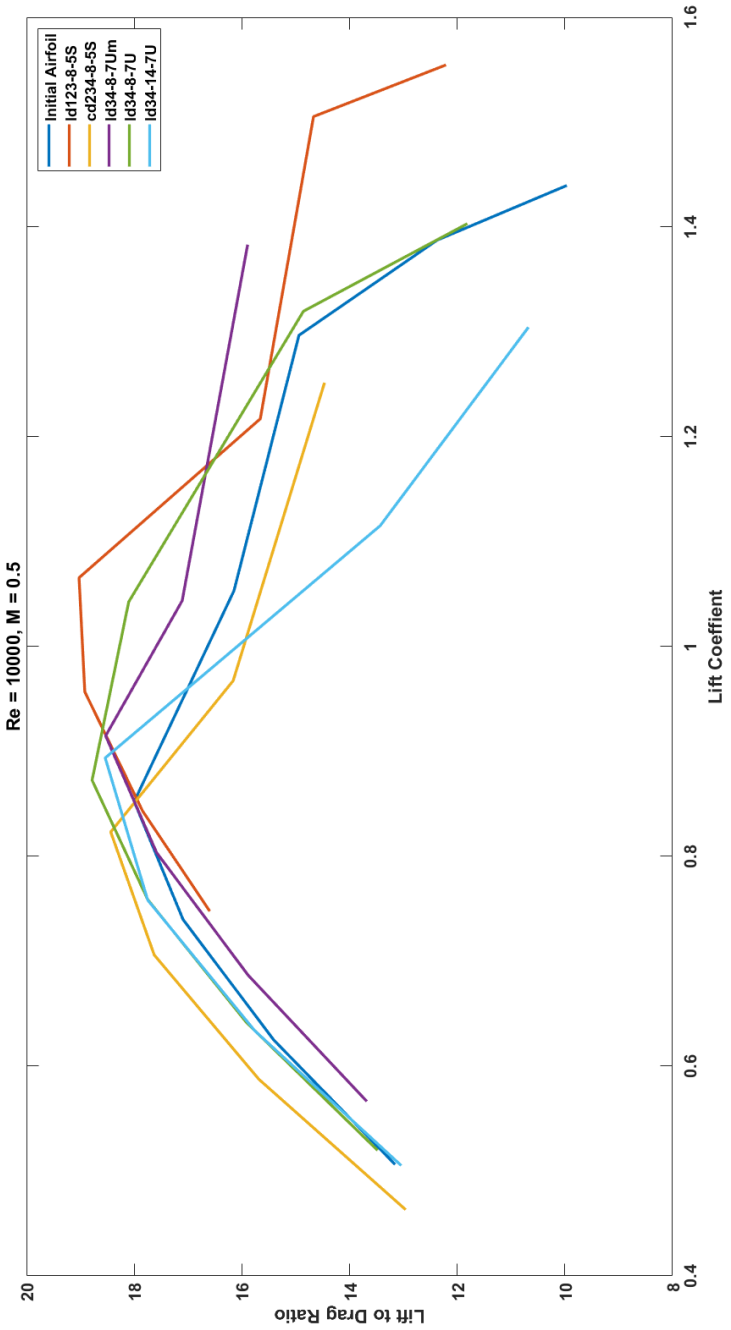

Figure 84: Comparison of lift to drag ratio variation with lift coefficients of all the airfoils present in the paper at Re = 10000 and M = 0.5

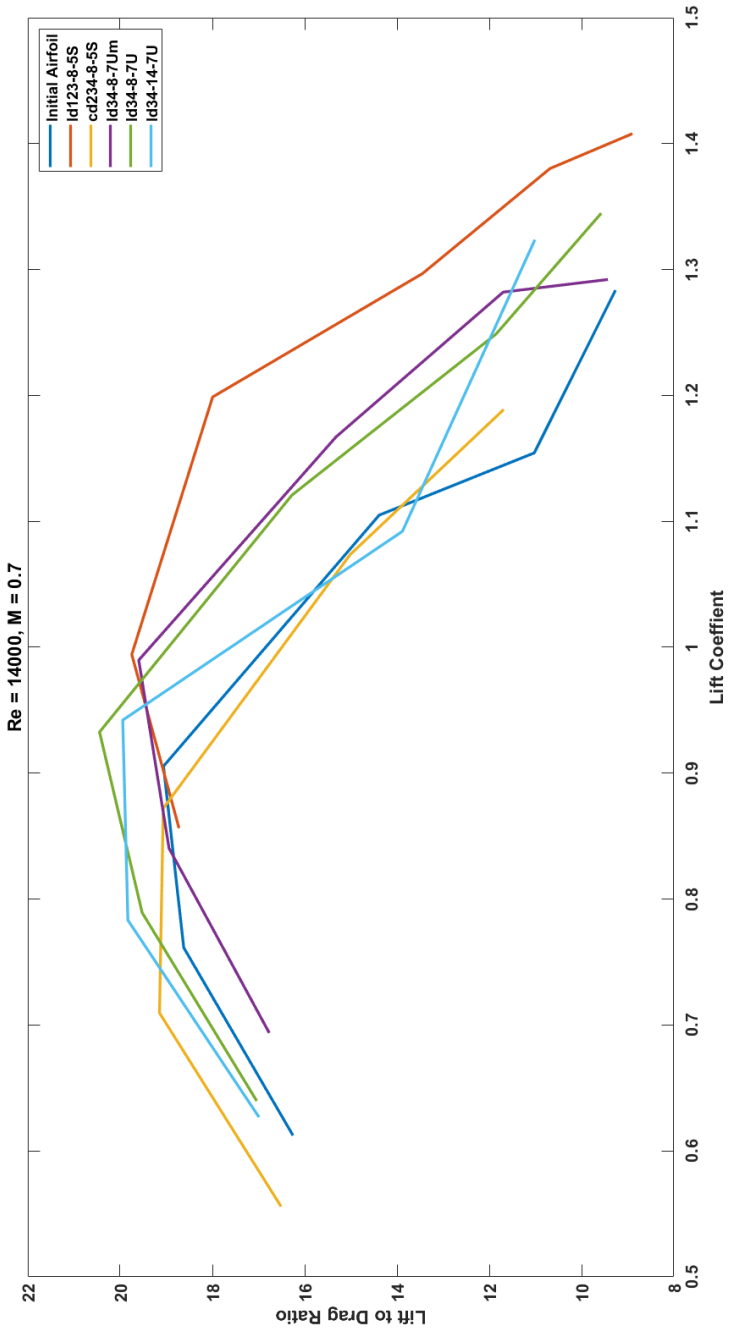

Figure 85: Comparison of lift to drag ratio variation with lift coefficients of all the airfoils present in the paper at Re = 14000 and M = 0.7

8 Conclusion

After analysing the principal phenomena developing in low Reynolds number flows over an airfoil, and describing the tools used in this paper, five optimized airfoils are obtained. These airfoils are optimized at different flow conditions and with different adjoint methods.

The performance of the initial airfoil are improved for all the airfoils.

In general, it can be stated that a shift toward the trailing edge of the maximum camber is beneficial for the performance of the airfoil at low angles of attack, where the flow is attached.

Another interesting feature of the optimization is that an optimization at low Reynolds number conditions improve the performances also at higher Reynolds number.

The one airfoil optimized at the highest Reynolds number proved to be the one with the most changes in geometry. The unsteady adjoint optimization tends to form short laminar separation bubbles on the airfoil at this Reynolds number, decreasing viscous drag while maintaining pressure drag almost constant. This feature is less effective at lower Reynolds number, where a reattachment is less probable due to the decreased instability of the boundary layer.

Although the steady adjoint procedure provided two airfoils with higher performance than the initial one, its limited range of usability represents a problem for improving airfoil in transonic flow. On the other hand, its cheap computational cost can be exploited using the procedure to adjust the parameters of the penalisation function.

Moreover, the penalisation function proved to be effective in maintaining the lift coefficient within the range requested. This function can be used in future works to improve the lift to drag ratio at different lift coefficients than that of the initial airfoil, thus obtaining different airfoil optimized for different lift conditions.

Finally, the unsteady adjoint optimization procedure described, although using an embedded steady solver, proved to be usable and extremely effective. Therefore, the unsteady residual can be used in the embedded steady adjoint solver, even in cases where oscillations are quite high. The choice of an instantaneous value for the cost function lead to better results in terms of performance and memory usage. The averaged fields, although with poorer results for the case presented, can be used for cases in which oscillations make the cost function too variable.

A Airfoil Nomenclature Used

To facilitate linking the airfoils to their respective optimization processes, the paper uses an alphanumeric nomenclature.

The name of an airfoil is divided into five fields: the first field contains two letters indicating the type of cost functions used; the second field contains a set of digits that indicates the rounded angle of attack in degrees at which the simulations of the optimization process are carried out; the third field contains a number that indicates the Reynolds number, divided by 1000, at which the simulations are done; the fourth field contains the Mach number, divided by

10, at which the simulations are done; the last field contains a set of letters indicating which optimisation process is used.

A generic airfoil name, in which X indicates a letter and N indicates a number, is:

$$XXNNN - N - NX$$

The first field uses the following initials:

- **ld** $\rightarrow$ lift to drag ratio maximization;
- **cd** $\rightarrow$ drag coefficient minimization;
- **cl** $\rightarrow$ lift coefficient maximization.

The last field uses the following initials:

- **S** $\rightarrow$ steady adjoint optimization;
- **U** $\rightarrow$ unsteady adjoint optimization with instantaneous flow fields (see section 6);
- **Um** $\rightarrow$ unsteady adjoint optimization with averaged flow fields (see section 6.

Therefore, the airfoils present in this paper are named:

- ld123-8-5S for Optimization 1;
- cd234-8-5S for Optimization 2;
- ld34-8-7Um for Optimization 3;
- ld34-8-7U for Optimization 4;
- ld34-14-7U for Optimization 5;

References

[1] Mark Drela. "Low-Reynolds-number airfoil design for the MIT Daedalus prototype-A case study". In: *Journal of Aircraft* 25.8 (1988), pp. 724–732.

[2] Mark Drela. "XFOIL: An analysis and design system for low Reynolds number airfoils". In: *Low Reynolds Number Aerodynamics: Proceedings of the Conference Notre Dame, Indiana, USA, 5–7 June 1989*. Springer. 1989, pp. 1–12.

[3] A Elsenaar and Travis W Binion. "Reynolds number effects in transonic flow". In: (1989).

[4] Donovan Selig and MS Fraser. "Airfoils at Low-Speeds". In: *A. Stokely, Virginia* (1989).

[5] Mark Drela. "Transonic low-Reynolds number airfoils". In: *Journal of Aircraft* 29.6 (1992), pp. 1106–1113.

[6] Venkat Venkatakrishnan. "On the accuracy of limiters and convergence to steady state solutions". In: *31st Aerospace Sciences Meeting*. 1993, p. 880.

[7] Peter G Baines, Sharan J Majumdar, and Humio Mitsudera. "The mechanics of the Tollmien-Schlichting wave". In: *Journal of fluid mechanics* 312 (1996), pp. 107–124.

[8] Jonathan M Weiss, Joseph P Maruszewski, and Wayne A Smith. "Implicit solution of preconditioned Navier-Stokes equations using algebraic multigrid". In: *AIAA journal* 37.1 (1999), pp. 29–36.

[9] Yousef Saad. *Iterative methods for sparse linear systems*. SIAM, 2003.

[10] Joel Brezillon and Richard Dwight. "Discrete adjoint of the Navier-Stokes equations for aerodynamic shape optimization". In: (2005).

[11] Wilna Du Toit. "Radial basis function interpolation". PhD thesis. Stellenbosch: Stellenbosch University, 2008.

[12] Juan C Meza. "Steepest descent". In: *Wiley Interdisciplinary Reviews: Computational Statistics* 2.6 (2010), pp. 719–722.

[13] Mohsen Jahanmiri. *Laminar separation bubble: its structure, dynamics and control*. Tech. rep. Chalmers University of Technology, 2011.

[14] Neil D Sandham. "Shock-wave/boundary-layer interactions". In: *NATO Research and Technology Organization (RTO)–Educational Notes Paper, RTO-EN-AVT-195* 5 (2011), pp. 1–18.

[15] Volker John. *Multigrid methods*. Tech. rep. Technical report, 2013.

[16] KL Hansen et al. "Laminar separation bubble effect on the lift curve slope of an airfoil". In: *19th Australasian Fluid Mechanics Conference*. RMIT University. 2014, pp. 8–11.

[17] Georgios Ntanakas, Marcus Meyer, and Kyriakos C Giannakoglou. "Employing the time-domain unsteady discrete adjoint method for shape optimization of three-dimensional multirow turbomachinery configurations". In: *Journal of Turbomachinery* 140.8 (2018), p. 081006.

[18] Justin Winslow et al. "Basic understanding of airfoil characteristics at low Reynolds numbers (10 4–10 5)". In: *Journal of Aircraft* 55.3 (2018), pp. 1050–1061.

[19] Thibault Désert et al. “Numerical predictions of low Reynolds number compressible aerodynamics”. In: *Aerospace Science and Technology* 92 (2019), pp. 211–223.

[20] PLM Siemens. “STAR-CCM+ User Guide Version 13.04”. In: *Siemens PLM Software Inc: Munich, Germany* (2019).

[21] Lance W Traub and Cory Coffman. “Efficient low-Reynolds-number airfoils”. In: *Journal of Aircraft* 56.5 (2019), pp. 1987–2003.

[22] Tianyu Xia et al. “Investigation on flow structure and aerodynamic characteristics over an airfoil at low Reynolds number—A review”. In: *AIP Advances* 11.5 (2021), p. 050701.

[23] M Carreño Ruiz and D D’Ambrosio. “Aerodynamic optimization and analysis of quadrotor blades operating in the Martian atmosphere”. In: *Aerospace Science and Technology* 132 (2023), p. 108047.

[24] Takuma Yamaguchi and Masayuki Anyoji. “Numerical Study on Low-Reynolds Compressible Flows around Mars Helicopter Rotor Blade Airfoil”. In: *Journal of Flow Control, Measurement & Visualization* 11.2 (2023), pp. 30–48.

Computing resources provided by hpc@polito, Academic Computing project of the Department of Automatics and Computer Science at the Polytechnic University of Turin (http://www.hpc.polito.it).